

AD-A205 075

Edward L. Ginzton Laboratory

OF THE
W.W. HANSEN LABORATORIES OF PHYSICS

STANFORD UNIVERSITY, STANFORD, CALIFORNIA 94305



SECURITY CLASSIFICATION OF THIS PAGE

AIA 205075 (2)

REPORT DOCUMENTATION PAGE

1a. REPORT SECURITY CLASSIFICATION UNCLASSIFIED		1b. RESTRICTIVE MARKINGS <i>DTIC FILE 0002</i>	
2a. SECURITY CLASSIFICATION AUTHORITY		3. DISTRIBUTION/AVAILABILITY OF REPORT Approved for public release; distribution is unlimited.	
2b. DECLASSIFICATION/DOWNGRADING SCHEDULE			
4. PERFORMING ORGANIZATION REPORT NUMBER(S)		5. MONITORING ORGANIZATION REPORT NUMBER(S) APOS R-TR- 89-0200	
6a. NAME OF PERFORMING ORGANIZATION Stanford University	6b. OFFICE SYMBOL (If applicable) AFOSR	7a. NAME OF MONITORING ORGANIZATION AFOSR/NP	
6c. ADDRESS (City, State, and ZIP Code) Jordan Quad/Birch Stanford, CA 94305-4125		7b. ADDRESS (City, State, and ZIP Code) Building 410, Bolling AFB DC 20332-6448	
8a. NAME OF FUNDING/SPONSORING ORGANIZATION AFOSR		8b. OFFICE SYMBOL (If applicable) AFOSR	
8c. ADDRESS (City, State, and ZIP Code) Building 410, Bolling AFB DC 20332-6448		8d. PROCUREMENT INSTRUMENT IDENTIFICATION NUMBER PRD020-355-A-300166	
9. TITLE (Include Security Classification) (U) PICOSECOND OPTICAL ELECTRONICS		10. SUBJECT KEY WORDS	
11. PERSONAL AUTHOR(S) Dr David M. Bloom		12. PERSONAL AUTHOR(S) Dr David M. Bloom	
13a. TYPE OF REPORT FINAL	13b. TIME COVERED FROM 1 Jul 85 TO 30 Jun 88	14. DATE OF REPORT (Year, Month, Day) August 1988	15. PAGE COUNT 114
16. SUPPLEMENTARY NOTATION			
17. COSATI CODES		18. SUBJECT TERMS (Continue on reverse if necessary and identify by block number)	
FIELD 20 06	GROUP	SUB-GROUP	
19. ABSTRACT (Continue on reverse if necessary and identify by block number) <i>Y 21/4</i> A technique permitting picosecond probing of internal nodes of GaAs integrated circuits has been developed. Bandwidths greater than 200 GHz are attained with 1.25 picosecond 1.06 micron optical pulses. The noise, bandwidth, and sensitivity have been examined in microwave probe station, oscilloscope display of time waveforms, and vector readouts for S-parameter measurements provide a simple user interface for the probe. Measurements have been made on digital circuits up to 18 GHz, microwave circuits and lines to 100 GHz, and novel structures to 3 picoseconds. An on-probe quintupler extends the range of available coplanar electrical excitation to 100 GHz.			
20. DISTRIBUTION/AVAILABILITY OF ABSTRACT <input checked="" type="checkbox"/> UNCLASSIFIED/UNLIMITED <input type="checkbox"/> SAME AS RPT. <input type="checkbox"/> DTIC USERS		21. ABSTRACT SECURITY CLASSIFICATION UNCLASSIFIED	
22a. NAME OF RESPONSIBLE INDIVIDUAL H R SCHLOSSBERG		22b. TELEPHONE (Include Area Code) (202) 767-4206	22c. OFFICE SYMBOL AFOSR/NP

DD FORM 1473, 84 MAR

83 APR edition may be used until exhausted.
All other editions are obsolete.

SECURITY CLASSIFICATION OF THIS PAGE

UNCLASSIFIED

DTIC
ELECTE

S

Final Report
to
Air Force Office of Scientific Research
on
A Program of Research
in
Picosecond Optical Electronics

K
Contract #F49620-85-0016

Principal Investigator:
David M. Bloom
Associate Professor of Electrical Engineering

August 1988

Approved for public release;
distribution unlimited.

U.S. AIR FORCE OFFICE OF SCIENTIFIC RESEARCH (AFSC)

AMERICAN AIRLINES CENTER
1100 KENNEDY AVENUE
FORT WORTH, TEXAS 76102

REF ID: A6200-12
SAC INFORMATION DIVISION

Picosecond Optical Electronics

Edward L. Ginzton Laboratory,

Stanford University

Stanford, CA 94305

(415) 723-0464



Accession For	
NTIS GRA&I	<input checked="" type="checkbox"/>
DTIC TAB	<input type="checkbox"/>
Unannounced	<input type="checkbox"/>
Justification	<input type="checkbox"/>
By _____	
Distribution/ _____	
Availability Codes	
Dist	Avail and/or Special
A-1	

Abstract

A technique permitting picosecond probing of internal nodes of GaAs integrated circuits has been developed. Bandwidths greater than 200 GHz are attained with 1.25 picosecond 1.06 micron optical pulses. The noise, bandwidth, and sensitivity have been examined in detail. The accuracy and invasiveness of the probe have also been characterized. A microwave probe station, oscilloscope display of time waveforms, and vector readouts for S-parameter measurements provide a simple user interface for the probe. Measurements have been made on digital circuits up to 18 GHz, microwave circuits and lines to 100 GHz, and novel structures to 3 picoseconds. An on-probe quintupler extends the range of available coplanar electrical excitation to 100 GHz.

TABLE OF CONTENTS

1. Introduction	1
1.1. Electrical test methods	2
1.2. Non-electrical, novel test techniques	3
2. Principles of Direct Electrooptic Sampling in GaAs IC's	11
2.1. Electrooptic voltage probing in a GaAs crystal	11
2.2. Probing geometries in GaAs IC	16
2.3. Electrooptic sampling	19
3. System Performance	23
3.1. System description	23
3.2. Bandwidth	28
3.3. Sensitivity	34
3.4. Linearity	42
3.5. Spatial resolution	42
3.6. Accuracy	45
3.7. Invasiveness	53
4. Circuit Measurements	57
4.1. Realistic circuit testing conditions	57
4.2. Digital circuit measurements	58
4.3. Microwave circuit measurements	62
4.4. Millimeter-wave circuit measurements	75
A. Active probe	75
B. Millimeter-wave potential mapping	82
C. Nonlinear network analysis	83
D. S-parameter measurements	84
5. Conclusion	101
6. Acknowledgments	102
References	103

1. Introduction

The development of advanced GaAs devices and integrated circuits has been spurred by a number of applications, including microwave and millimeter-wave radar and communication systems, fiber optic digital data transmission at gigahertz rates, high-speed data acquisition, and the constant push for faster digital logic in high-speed computers and signal processors; the IC's developed for these applications are creating new demands upon high-speed electronic instrumentation.

One demand is for increased instrument bandwidth. GaAs MESFET's have demonstrated a maximum frequency of oscillation, f_{max} , in excess of 110 GHz [1], while pseudomorphic In-GaAs/AlGaAs modulation-doped field-effect transistors [2] have shown power-gain bandwidth products which extrapolate to give $f_{max} = 200$ GHz, resonant tunnelling diodes have oscillated at 56 GHz [3], and heterojunction bipolar transistors and permeable base transistors currently under development should show similar performance. Because the maximum frequency of oscillation of these devices is often greater than the 100 GHz bandwidth of commercial millimeter-wave network analyzers, f_{max} is estimated by extrapolation from measurements at lower frequencies. Used as switching elements, propagation delays and transition times of 1-10 ps should be expected for these devices, well below the resolution of commercial sampling oscilloscopes. In either case the device bandwidth exceeds that of the measurement instrument.

A second demand is for noninvasive access to the internal signals within high-speed integrated circuits. GaAs digital integrated circuits of MSI (medium-scale integration) complexity and 1-5 GHz clock rates are now available commercially, as are GaAs monolithic microwave integrated circuits (MMIC's) of SSI (small-scale integration) complexity and 1-26 GHz bandwidths. More complex LSI (large-scale integration) digital circuits are under development, and experimental SSI digital circuits operating with 18 GHz clock rates [4] have been demonstrated. In contrast to silicon LSI integrated circuits operating at clock rates in the tens and hundreds of megahertz, the development of GaAs high-speed circuits is hampered both by poorly refined device models and by layout-dependent circuit parasitics associated with the high frequencies of operation. A test instrument providing noninvasive measurements within the integrated circuit would permit full characterization of such complex high-speed IC's.

These issues have motivated a number of researchers to investigate alternative test techniques, both to increase measurement bandwidth and to allow internal testing of IC's. This paper begins with a review of conventional test methods and instruments, summarizes several new test techniques for IC's, and then describes in detail the principles, capabilities, limitations, and IC measurement results of direct electrooptic sampling, a measurement technique that allows for internal-node voltage measurements in GaAs IC's with picosecond time resolution, corresponding to bandwidths in excess of 100 GHz.

1.1. Electrical test methods

We begin by considering the limitations of conventional test instruments. Their capabilities and characteristics are determined by two features: the IC probe that connects the test instrument to the circuit and the test instrument itself. The IC probe has its own intrinsic bandwidth that may limit the test method. In addition, the probe also determines an instrument's ability to probe *internal* to the IC due to its size (limiting its spatial resolution) and influence on circuit performance (loading of the circuit from its characteristic and parasitic impedances.) The test instrument sets the available bandwidth given perfect IC probes or packaged circuits, and defines the type of electrical test, such as measuring time or frequency response.

Connection of a test instrument to an IC begins with the external connectors, typically $50\ \Omega$ coaxial cable with a microwave connector, such as SMA and APC-3.5, standard microwave connectors, or K-connector and APC-2.4, newer connectors for 46 GHz (K) or 50 GHz (APC 2.4) operation. The IC probes are the *transitions* from the coaxial cable to some type of contact point with a size comparable to an IC bond pad. Low-frequency signals are often connected with needle probes. At frequencies greater than several hundred megahertz these probes have serious *parasitic* impedances, due to shunt capacitance from fringing fields and series inductance from the long, thin needle. The parasitic impedances and the relatively large probe size compared to IC interconnects limit their effective use to low-frequency external input or output circuit responses at the bond pads. For signals greater than several hundred megahertz, the recently developed Cascade Microtech probe [5,6] has demonstrated IC connections to millimeter-wave frequencies of 50 GHz. The probe consists of a coaxial connector with a transition to $50\ \Omega$ coplanar waveguide (CPW) transmission line that then tapers to bond pad size contacts. They offer good microwave performance, but their size limits test points to IC bond pads and their $50\ \Omega$ characteristic impedance limits their use to input or output sections of the IC.

Thus, electrical probes suffer from a measurement dilemma. Good high-frequency probes use transmission lines to control the line impedance from the coaxial transition to the IC bond pad and to reduce parasitic impedances. The low characteristic impedance of such lines (typically $50\ \Omega$) limits their use to input/output connections. High-impedance probes suitable for probing intermediate circuit nodes have significant parasitic impedances at microwave frequencies, severely perturbing the circuit operation and affecting the measurement accuracy. In both cases, the probe size is large compared to IC interconnect size, limiting their use to test points the size of bond pads.

Conventional test instruments for measuring high-speed electrical signals consist of sampling oscilloscopes, spectrum analyzers, and network analyzers. Sampling oscilloscopes measure the time response of repetitive signals with a resolution as short as 25 ps or a bandwidth of 14 GHz. Combined with transmission line probes this instrument gives either time domain reflectometry measurements or signal waveforms of an IC's external response, but has neither the time resolution required for state-of-the-art GaAs IC's nor the ability to measure the internal node response of MSI or LSI IC's. A promising note is the recent introduction of a new sampling oscilloscope based on Josephson Junction superconducting technology [7] with a time resolution of about 8 ps. As with slower

sampling oscilloscopes, however, the $50\ \Omega$ connectors limit its use to external characterization of IC's.

Spectrum and network analyzers measure the response of circuits in the frequency domain, with a range of 26.5 GHz typically and limited extension through the millimeter-wave frequencies to 300 GHz. A spectrum analyzer measures the power spectrum of a signal, while network analyzers measure the vector transfer function of a network (magnitude and phase) as a function of frequency. The small-signal, linear characteristics of microwave devices and circuits measured with a network analyzer are usually expressed in terms of the scattering parameters. These provide a measure (often extrapolated) of f_{max} , a device's maximum frequency of oscillation, and f_T , the unity current gain frequency, figures of merit of a device's operation speed. The frequency range of these instruments can be extended to millimeter-wave frequencies (300 GHz for the spectrum analyzer, 100 GHz for the network analyzer) using external source multipliers, mixers and waveguide connectors, but the frequency coverage is limited to 1.5:1 waveguide bandwidths and the waveguide connectors require a hybrid mount of the IC in a waveguide package, preventing wafer testing of the IC. Network analyzers can provide time-domain measurements of a network's small-signal step or impulse response by Fourier transforming the small-signal frequency-domain two-port device parameters. For large-signal measurements, where the network is no longer linear, the principle of superposition cannot be applied, preventing calculation of the large-signal time-domain response from measurements of frequency-domain transfer functions. For example, the network analyzer cannot measure the time waveform response of the IC's due to amplifier saturation. Although spectrum analyzers can measure the harmonic spectrum magnitude of saturated or large-signal circuit responses, the phases of the harmonics are not measured, and the large-signal time waveforms again cannot be inferred. Both instruments also rely on $50\ \Omega$ connectors and IC probes, limiting their ability to probe an IC to its external response. For network analysis, a further issue is de-embedding the device parameters from the connector and circuit fixture response, a task which grows progressively more difficult at increasing frequencies, particularly for millimeter-wave testing.

1.2. Non-Electrical, Novel test techniques

With the objective of either increased bandwidth or internal IC testing with high spatial resolution (or both) a number of new test techniques have been introduced and demonstrated. One method of measuring a voltage on IC conductors is to energy analyze secondary electron emission. To test logic level signals in VLSI silicon IC's researchers in the late 1960's developed the voltage contrast scanning electron microscope (SEM) or E-beam probing [8,9]. This technique uses an electron beam from an SEM to stimulate secondary electron emission from surface metallization. For a metal conductor at ground or negative potential, the electrons have sufficient energy to be collected by a detector shielded by an energy analyzer grid. Metal lines at a positive potential retard the emitted electrons, lowering their energy and reducing the number of electrons detected. The detected signal is small for IC voltage levels; to improve time resolution the signal is sampled with electron beam pulses and averaged to improve signal-to-noise ratio.

Commercial SEM's have sensitivities of 1-10 mV, bandwidths up to 2 GHz or time resolutions of ≈ 1 ns, and a spatial resolution as small as 20 nm. Compared to typical operating speeds of com-

mmercial silicon VLSI (clock rates of 10 to 100 MHz) this technique has good time resolution, acceptable sensitivity, and excellent spatial resolution. The system's time resolution is set by gating the E-beam from the thermionic cathodes of standard SEM's. For decreasing electron beam duration required for increased time resolution, the average beam current decreases, degrading measurement sensitivity and limiting practical systems to a time resolution of several hundred picoseconds. To overcome this limitation, a technique which implements a photocathode triggered by an intense picosecond optical pulse to generate short, high-current electron pulses [10] has been demonstrated. This approach shows promise for achieving time resolution approaching 10 ps with the SEM probe. The major drawbacks of SEM testing are its complexity and its relatively high cost.

Photoemissive sampling, based on analyzing secondary electron emission from IC conductors similar to E-beam testing, uses intense, energetic light from a pulsed laser focused on an IC conductor to generate photoelectrons. An extraction/retarding grid combination placed in close proximity to the conductor energy analyzes the electrons, with a resulting secondary electron emission varying with the conductor potential. The feasibility of this new approach is made possible by picosecond pulselwidth, high peak power lasers, and offers a potential improvement in time resolution and sensitivity over the SEM probe. The technique is not available commercially, but a number of researchers have demonstrated systems with time resolution as short as 7 ps with good spatial resolution and millivolt sensitivity [11,12,13]. With both electron-beam and photoemissive sampling, electron beams and electron extraction fields can produce charge concentrations within the semiconductor substrate through charging of deep levels, or at its surface, through field-induced surface inversion.

A technique which optically senses free-carrier charge density was recently developed for measurements within silicon IC devices [14,15]. Because of its centrosymmetric crystal structure, silicon exhibits no bulk second-order optical nonlinearities, such as the electrooptic effect, to use as a basis for an optical measurement system. Third-order effects, such as voltage-dependent second-harmonic generation or the optical Kerr effect, are in general very weak and result in impractical systems in terms of measurement sensitivity and implementation. Most semiconductor devices function by modulating charge density within a control region, which contributes to material index of refraction as described by the plasma-optical relation

$$n = n_0 \left(1 - \frac{\omega_p^2}{\omega^2} \right)^{\frac{1}{2}} \quad (1)$$

$$\omega_p^2 = \frac{q^2 N}{\epsilon_s m_e^*} + \frac{q^2 P}{\epsilon_s m_h^*} \quad (2)$$

where n_0 is the bulk index of refraction, ω is the optical probe frequency, ω_p is the plasma resonance frequency, N is the electron concentration in the conduction band, P is the hole concentration in the valence band, ϵ_s is the permittivity of the substrate material, and m_e^* and m_h^* are the electron/hole conductivity effective masses. The change in charge density is detected with a compact optical interferometer using a 1.3 μm wavelength (the absorption minimum in silicon) semiconductor laser as the

probe, shown schematically in Figure 1. In contrast to electrooptic techniques, where typical probe beam intensity modulation is on the order of 0.1%, for the charge density typical of integrated silicon bipolar transistors the probe beam modulation in the charge-sensing system is on the order of 1%. This sensitivity has allowed the demonstration of single-shot (i.e. no repetitive sampling) detection of a silicon bipolar junction transistor's switching signal in a 200 MHz bandwidth (Figure 2). Since the plasma-optical effect occurs in all semiconductor materials, this technique is applicable to GaAs IC's and shows promise for studying device characteristics and charge dynamics.

Another optical probe scheme is electrooptic sampling, which uses an electrooptic light modulator to intensity modulate a probe beam in proportion to a circuit voltage. The technique was initially developed to measure the response of photoconductors and photodetectors faster than the time resolution of sampling oscilloscopes [16,17,18,19] and used an external electrooptic modulator (typically lithium tantalate, LiTaO_3) connected to the device under test. A polarized optical probe beam passes through an electrooptic crystal, whose index of refraction changes due to the presence of an electrical signal (Figure 3.) The polarization of the light after passing through the electrooptic crystal depends on the signal driving the modulator, and passing the probe beam through a polarizer results in a signal-dependent intensity modulation. The approach exhibits excellent time resolution (<0.5 ps) due to the advanced level of ultrashort pulse generation with the colliding-pulse mode-locked (CPM) laser and the very high intrinsic speed of the electrooptic effect. Combined with a cryogenic system, optical measurements of electrical signals have been made at liquid helium temperatures[20]. However, the hybrid lithium tantalate electrooptic modulator requires connecting the test point on the IC to the transmission line of the modulator, restricting its use to external test points. Unless carefully designed, the system's time resolution is degraded by the hybrid connection between the modulator and the device under test, due to the loading of the test point from the relatively low characteristic impedance of the transmission line, and due to the parasitic impedances of bond wires.

Using an electrooptic needle probe (Figures 4&5) [21], the technique has been extended to internal node probing of IC's. The needle, a fused silica rod with a 40×40 micron tip of LiTaO_3 coated for high reflection of the probe beam, is brought close to a conductor, introducing fields within the probe tip. As with the hybrid electrooptic scheme, the electric fields change the polarization of the probing beam, and the reflected beam is analyzed by a polarizer. The LiTaO_3 electrooptic material, transparent to visible wavelength light, allows the use of ultrashort sampling pulses from a CPM laser; a step response risetime of less than 300 fs has been demonstrated[22,23]. Because the probe relies on no optical or electrical properties of the circuit under test, circuits of any substrate material can be tested without sample preparation. The probe exhibits some small circuit invasiveness through capacitive loading on the order of 10 femtofarads due to the proximity of the LiTaO_3 probe tip of dielectric constant $\epsilon_r = 40$. The polarization shift in lithium tantalate, proportional to the lateral electric field, may make the probe sensitive to signals from nearby conductors in addition to the potential of the probed conductor.

The external electrooptic sampling techniques described above can provide signal measurements with subpicosecond time resolution (equivalent to bandwidths of approaching 1 THz.) Direct electrooptic sampling, a related technique where the substrate of the GaAs circuit under test serves as the electrooptic modulator, eliminates the electrical parasitics associated with external electrooptic elements and provides voltage measurements of points internal to the IC with picosecond time resolution and

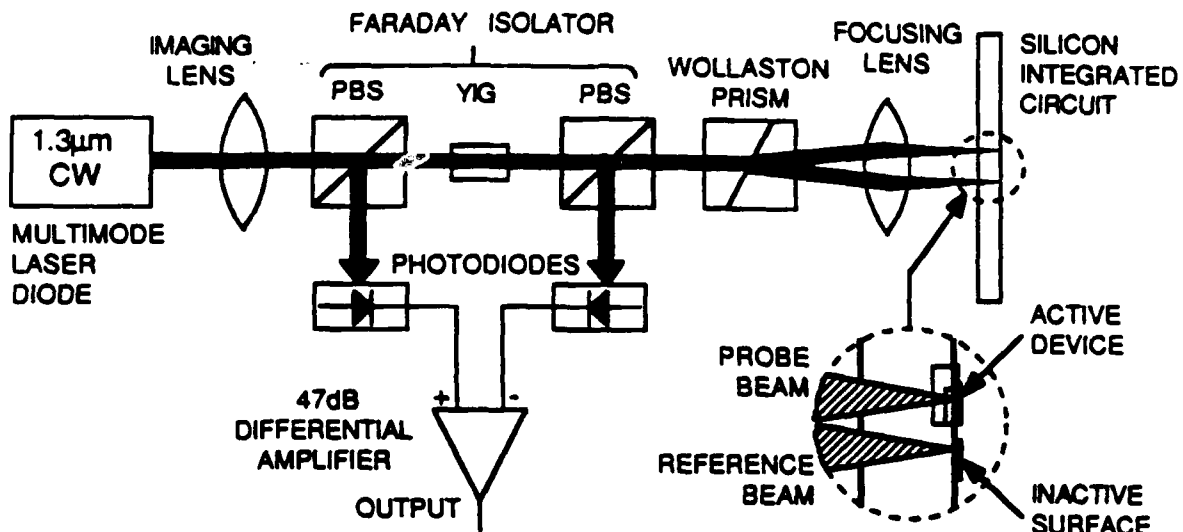


Figure 1: Charge-sensing system schematic [14,15]. The Wollaston prism separates the input beam into a probe beam and a reference beam. The presence of charge in the probe beam path results in a change in output intensity at the photodiodes proportional to the charge concentration, as described in the text. PBS denotes a polarizing beamsplitter cube.

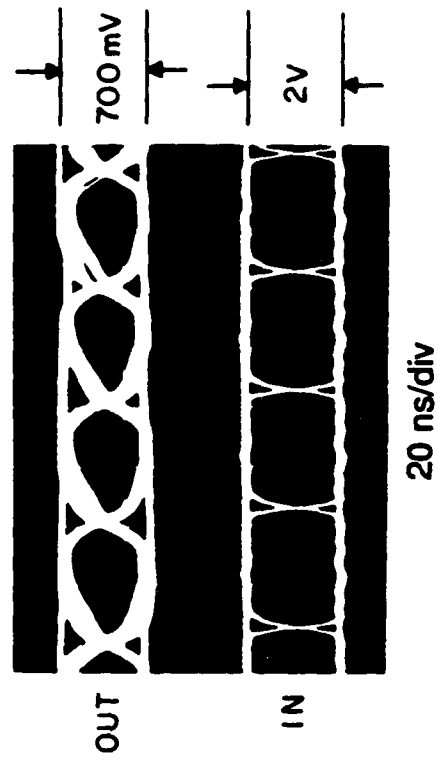


Figure 2: Eye diagram of the stored base charge in a silicon bipolar-junction transistor, as monitored by the optical charge-sensing system, upper trace. The corresponding base voltage is shown in the lower trace. The input signal is 25 Megabaud pseudo-random Manchester-coded data. Time scale is 20 ns per division.

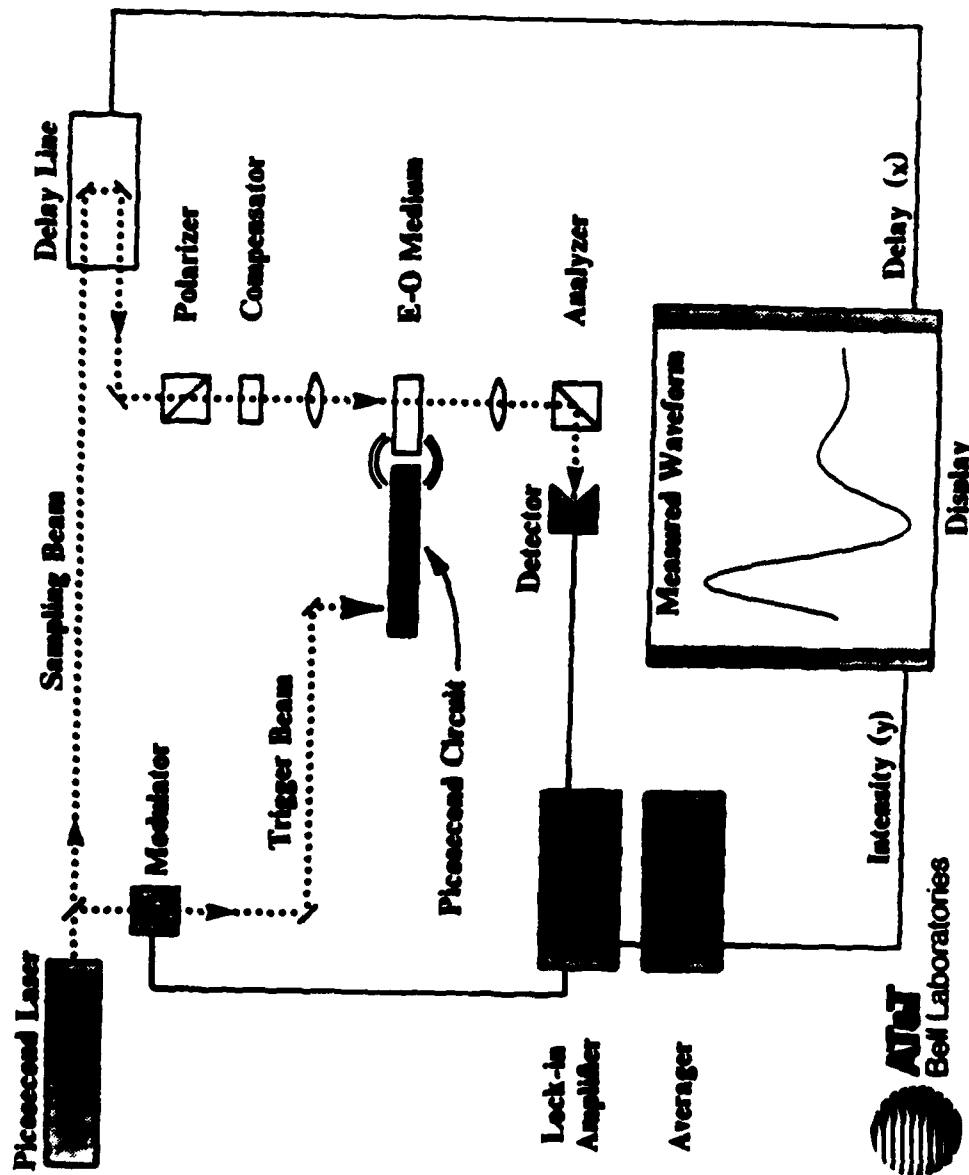


Figure 3: Electrooptic sampling system [18]. Courtesy of J.A. Valdmanis, AT&T Bell Laboratories.

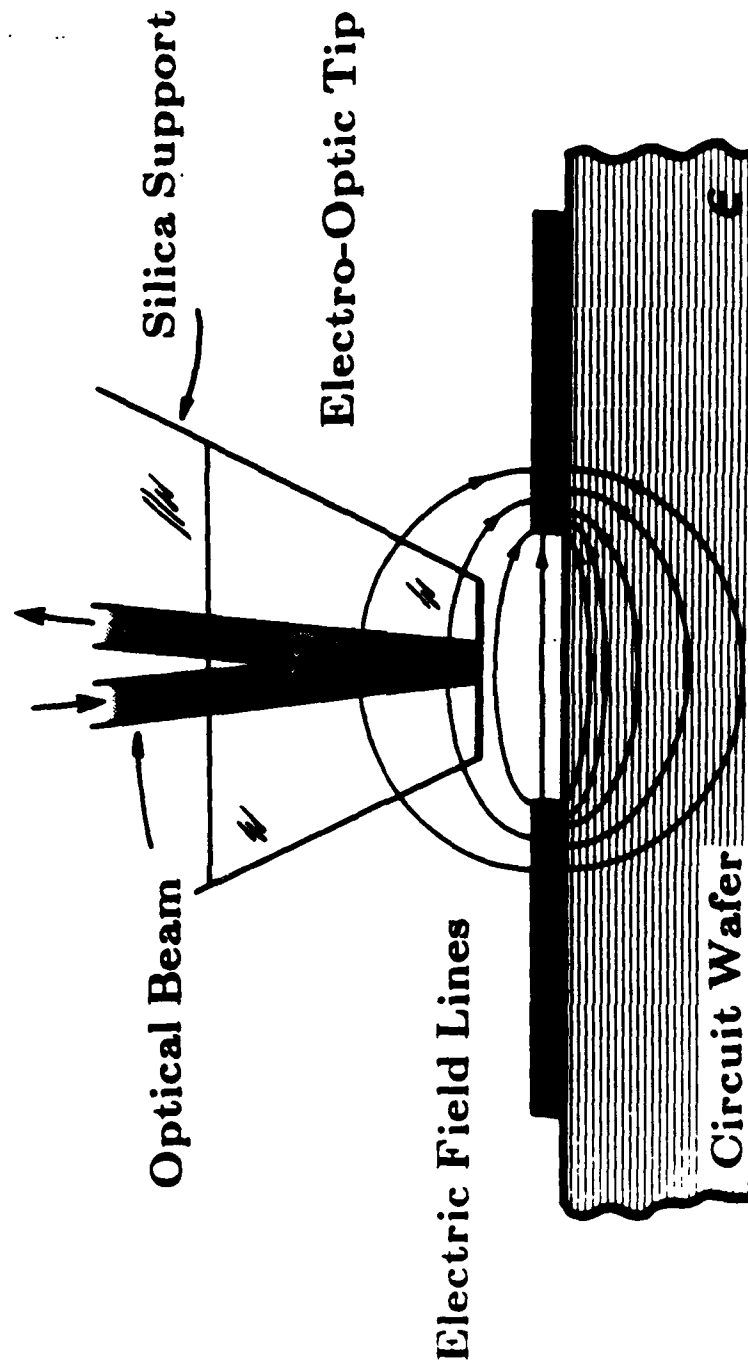


Figure 4: Electro-optic needle probe for on-wafer measurements [21,22]. Courtesy of J.A. Valdmanis, AT&T Bell Laboratories.

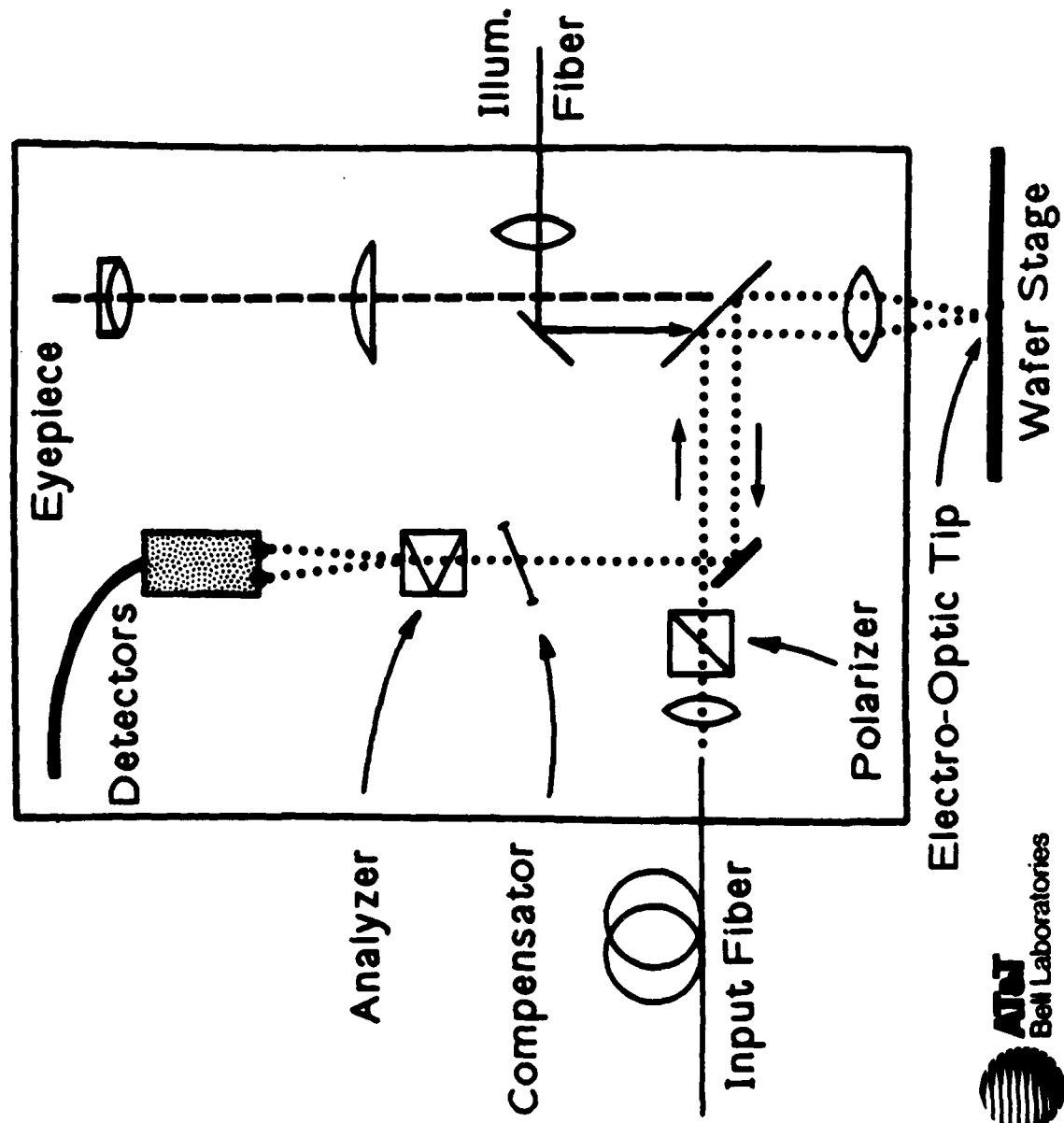


Figure 5: Sampling system for on-wafer measurements with the electrooptic needle probe. Courtesy of J.A. Valdmanis, AT&T Bell Laboratories.



micron spatial resolution. This method's principles, capabilities, and circuit measurement results are described in the following sections.

2. Principles of Direct Electrooptic Sampling in GaAs IC's

The electrooptic effect, an anisotropic variation in a material's dielectric constant due to an applied electric field, is present in a variety of non-centrosymmetric crystals. Among these are GaAs, InP and AlAs, used for high-speed semiconductor devices, and lithium niobate (LiNbO_3), lithium tantalate (LiTaO_3) and potassium dihydrogen phosphate (KH_2PO_4), used for nonlinear optical devices. Centrosymmetric crystals do not exhibit the electrooptic effect; notable among these materials are silicon and germanium. The change in refractive index of electrooptic materials with electric field can be used for optical phase-modulation, and, from this, polarization-modulation or intensity-modulation [24,25]. Direct electrooptic sampling uses the electrooptic effect in GaAs to obtain voltage-dependent intensity modulation of a probe beam [26,27]. As with other experimental probing methods, a pulsed optical probe beam permits a potential time resolution on the order of one picosecond or instrument bandwidths greater than 100 GHz.

Without external electrooptic elements, the invasive properties of those elements are eliminated, permitting probing with no electrical contact, no loading of the test point with low-impedance transmission lines, and no parasitic probe impedance. Because the probing beam can be focused to a spot of diameter of several microns, the probe's spatial resolution allows access to finely-spaced conductors in LSI GaAs circuits. Direct electrooptic sampling thus provides the bandwidth, the spatial resolution, and the internal-node access necessary for characterization of high-speed GaAs integrated circuits.

2.1. Electrooptic Voltage Probing in a GaAs Crystal

GaAs is one of simplest electrooptic crystals, a zincblende with crystal symmetry $\bar{4}3m$. Its cubic structure results in no natural (field-free) birefringence and a symmetric electrooptic tensor with equal-valued elements. The electrooptic tensor in GaAs is [28]

$$r_{jk} = \begin{pmatrix} 0 & 0 & 0 \\ 0 & 0 & 0 \\ 0 & 0 & 0 \\ r_{41} & 0 & 0 \\ 0 & r_{41} & 0 \\ 0 & 0 & r_{41} \end{pmatrix} \quad (3)$$

An applied electric field induces a birefringence described by the index ellipsoid

$$\frac{x^2}{n_0^2} + \frac{y^2}{n_0^2} + \frac{z^2}{n_0^2} + 2r_{41}yzE_x + 2r_{41}xzE_y + 2r_{41}xyE_z = 1 \quad (4)$$

where n_0 is the zero-field refractive index, r_{41} is the electro-optic coefficient for GaAs, and E is the applied electric field in the direction indicated by its subscript. The intersection of the index ellipsoid and a plane normal to the optical propagation direction defines an ellipse whose major and minor axes give the allowed (eigenvector) polarization directions and their refractive indices.

To relate this to an IC substrate, Figure 6 shows the principal crystal axes of a GaAs IC fabricated on standard (100)-cut material. The X, Y, and Z axes are aligned with the <100> directions of the GaAs cubic Bravais lattice, while the Y' and Z' axes are aligned with the [011] and [011] directions parallel to the cleave planes of the a GaAs wafer (along which individual IC's are scribed) and 45° to the [010] and [001] directions. For an optical plane wave traveling in the X direction, the intersection of the index ellipsoid and the $x=0$ plane normal to its direction of propagation defines an ellipse in the (Y', Z') plane

$$y'^2 \left(\frac{1}{n_0^2} - r_{41}E_x \right) + z'^2 \left(\frac{1}{n_0^2} + r_{41}E_x \right) = 1 \quad (5)$$

The Y' and Z' axes are the eigenvectors of the electrooptic effect and form the natural coordinate system for describing electrooptic sampling in GaAs IC's. The refractive indices $n_{y'}$ and $n_{z'}$ in the Y' and Z' directions are

$$n_{y'} = n_0 + \frac{n_0^3 r_{41} E_x}{2} \quad (6a)$$

$$n_{z'} = n_0 - \frac{n_0^3 r_{41} E_x}{2} \quad (6b)$$

and these field-dependent refractive indices result in differential phase shift for beam polarizations in the Y' and Z' directions.

Consider the transmission electrooptic amplitude modulator shown in Figure 7. A circularly-polarized plane wave propagating through the substrate receives a change in phase between the Y' and Z' polarizations due to the electrooptic effect in proportion to the electric field given by

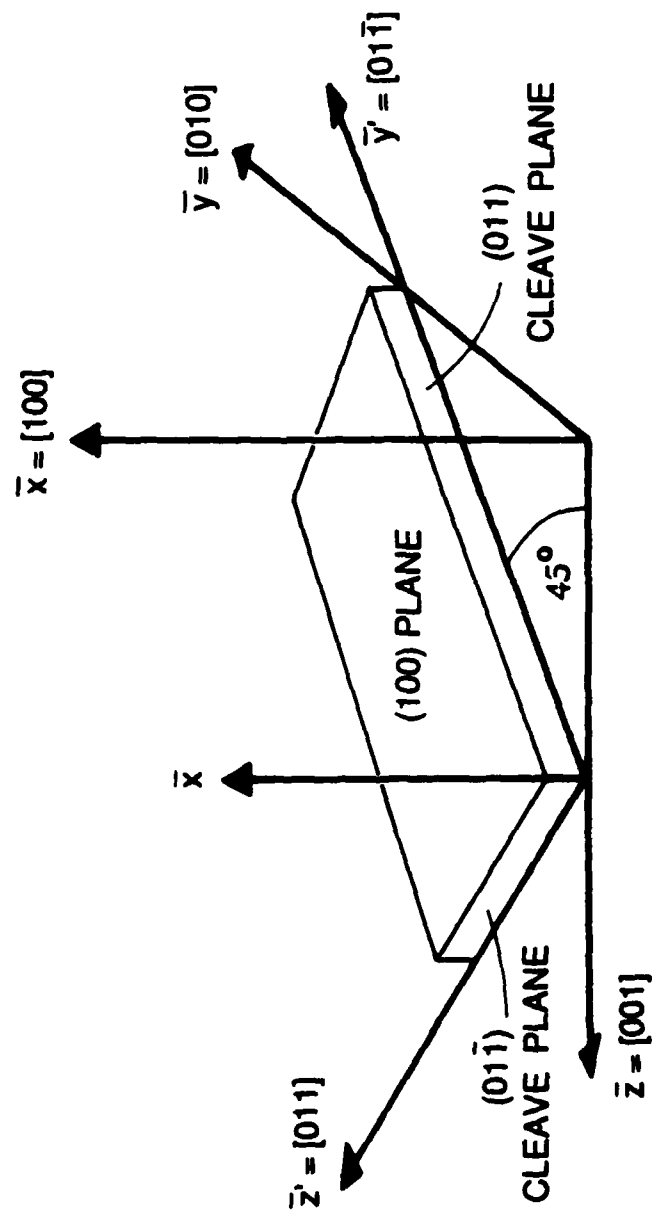


Figure 6: Principal axes and cleave planes in (100)-cut Gallium Arsenide.

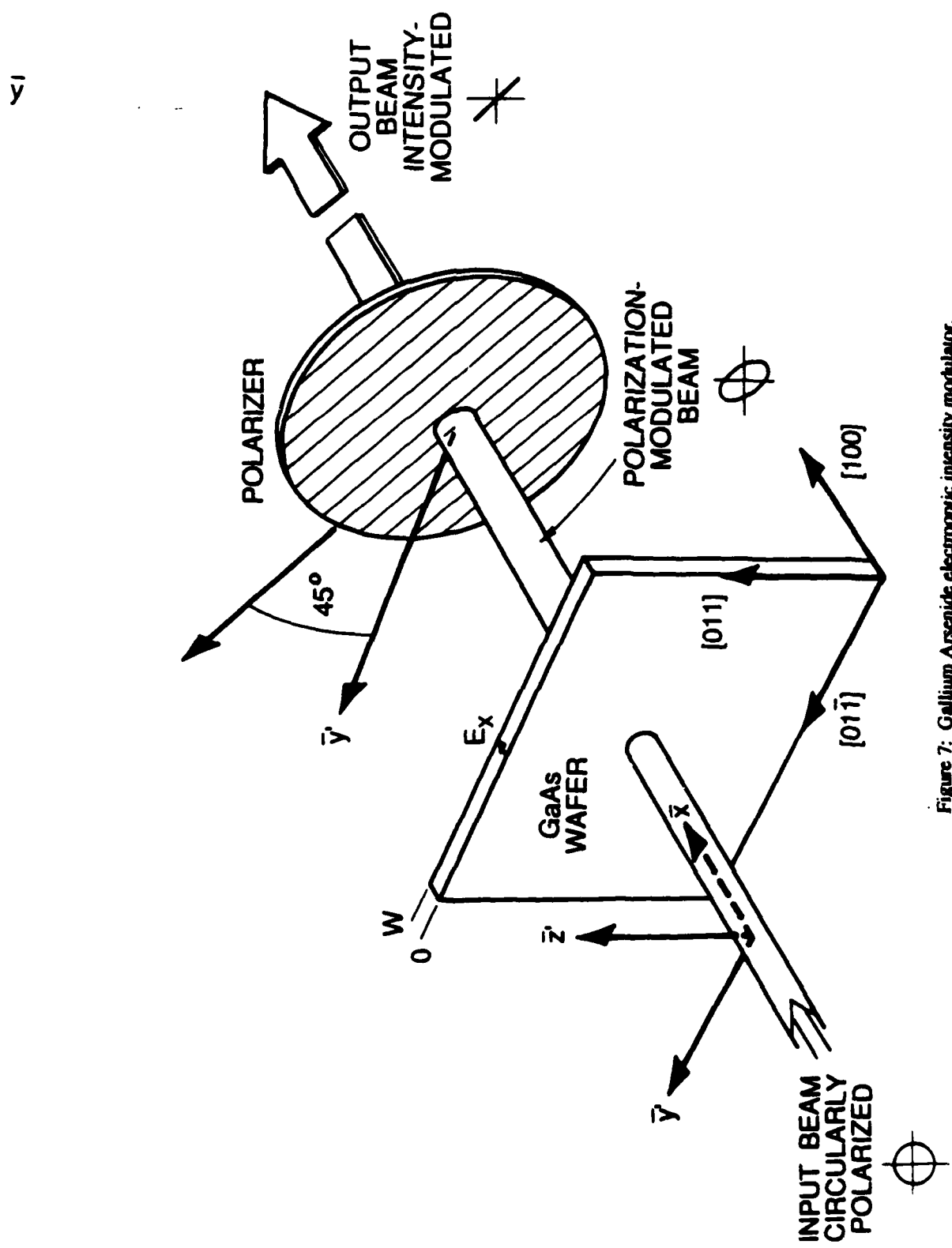


Figure 7: Gallium Arsenide electrooptic intensity modulator.

$$\Delta\phi = \frac{2\pi n_0^3 r_{41}}{\lambda_0} E_x W = \frac{2\pi n_0^3 r_{41}}{\lambda_0} V \quad (7)$$

such that the beam emerging from the substrate has changed from circular to slightly elliptical polarization. Note that the product $E_x W$ of the substrate thickness and the x-component of the electric field is the potential difference V between the front and back surfaces of the GaAs wafer where the probing beam traverses the wafer. This result holds for a general field distribution; a plane-wave optical beam propagating along a $<100>$ direction experiences a change in phase shift proportional to product of the longitudinal electric field and the substrate thickness, i.e. it is *only* affected by the potential difference V across the wafer at the probe point.

To measure this voltage-induced polarization change, the beam emerging from the GaAs is passed through a polarizer oriented at 45° to the Y' and Z' axes. The intensity of the output beam is then

$$P_{out}(V) = P_0 \left[1 + \sin \left(\frac{2\pi}{\lambda_0} n_0^3 r_{41} V \right) \right] \\ = P_0 \left[1 + \sin \left(\frac{\pi V}{V_\pi} \right) \right] \quad (8)$$

where P_0 is the output intensity with zero field in the substrate. V_π , called the half-wave-voltage, and given by

$$V_\pi = \frac{\lambda_0}{2 n_0^3 r_{41}} \quad (9)$$

is the voltage required for 180° phase shift between the Y' and Z' polarizations. For GaAs, $V_\pi \approx 10$ kV at a wavelength of $1.064 \mu\text{m}$ for $n_0 = 3.6$, and $r_{41} \approx 1.4 * 10^{-12} \text{ m/V}$ [29]; the argument of the sine expression is thus small for typical voltages V on integrated circuits, and Eqn. 8 can be approximated by

$$P_{out} \approx P_0 \left[1 + \frac{\pi V}{V_\pi} \right] \quad (10)$$

Thus for substrate voltages to several hundred volts, the output beam intensity is nearly linear and in direct proportion to the voltage across the substrate. The intensity of the output beam, detected by a photodiode, is thus a measure of the voltage across the substrate of the IC.

2.2. Probing geometries in GaAs IC's

The transmission modulator of Figure 7 requires separate lenses for focusing and collecting the probe beam, precisely aligned on opposite sides of the wafer for IC measurements. Also, high-density interconnections on the circuit side of digital IC's and backside metallization on many microwave IC's would obstruct the beam passage through the wafer. Reflection-type probing geometries as shown in Figure 8 provide better access to IC's, using a single lens for focusing and using the IC metallization for reflection. The frontside geometry is suitable for probing microstrip transmission lines of MMIC's. The backside geometry permits very tight focusing of the probing beam to a diameter limited by the numerical aperture of the focusing lens, and provides a probe beam modulation sensitive to the probed conductor's voltage but independent of nearby signal conductors for typical IC layout[30], a necessity for testing high-density IC's.

For microstrip transmission lines typically used in MMIC's, the fields extend laterally from the conductor roughly a distance equal the substrate thickness; the probe beam is focused from the top of the substrate through the fringing fields of the conductor to a beam spot size diameter approximately one-tenth of the substrate thickness so that it overlaps well with the fringing fields. Other MMIC's use planar transmission lines such as coplanar waveguide (CPW) for microwave interconnects. MSI/LSI circuits typically use thin metal lines (3 to 10 μm); the electric field distribution around the conductors is a strong function of their layout. For these types of interconnects and for planar transmission lines, the extent of the fields into the substrate is on the order of the distance between signal conductors and grounds. Typical IC substrate thickness (400 to 500 μm) is much greater than conductor spacings; the electric fields lie near the substrate surface, and the back of the substrate is nearly at an equipotential with respect to individual conductors on the IC surface. The optical probe, focused through the back of the substrate to a spot diameter less than or equal to the conductor width, is modulated by the voltage on the conductor nearly independent of signals from nearby conductors (see Section 4.2 on digital circuits and Figs. 28 & 29 for examples of probing closely spaced IC conductors.)

In both cases the optical probe is reflected from metallization on the IC. The signal is proportional to the amount of light reflected, and if the reflectivity of the metallization varies, the signal strength also varies. The signal can be normalized to the amount of reflected light, but metallization such as ohmic contacts, which may be very rough, will cause poor signal sensitivity if a large fraction of the probe beam is scattered. Because integrated circuits are patterned by optical lithography, the wafer top surface has good optical quality. For backside probing the back of the wafer must be polished to allow passage of the probe beam with negligible scattering. For frontside probing the ground plane should be sufficiently reflective to provide a good return beam - most MMIC's we have encountered have shown adequate ground-plane reflectivity.

In reflection-mode probing, the incident and reflected beams, centered on the microscope lens for optimum focusing, can be separated by manipulation of their polarizations (Figure 9.) The advantages of this arrangement for IC probing are ease-of-alignment, on-axis focusing for diffraction-limited spot size, and efficient use of the optical signal (in contrast to using a beamsplitter to separate the incident and return beams, which attenuates half the optical power on each pass.) The polarization states of this arrangement may be analyzed by Jones calculus, and are qualitatively described as

Frontside Probing

Backside Probing

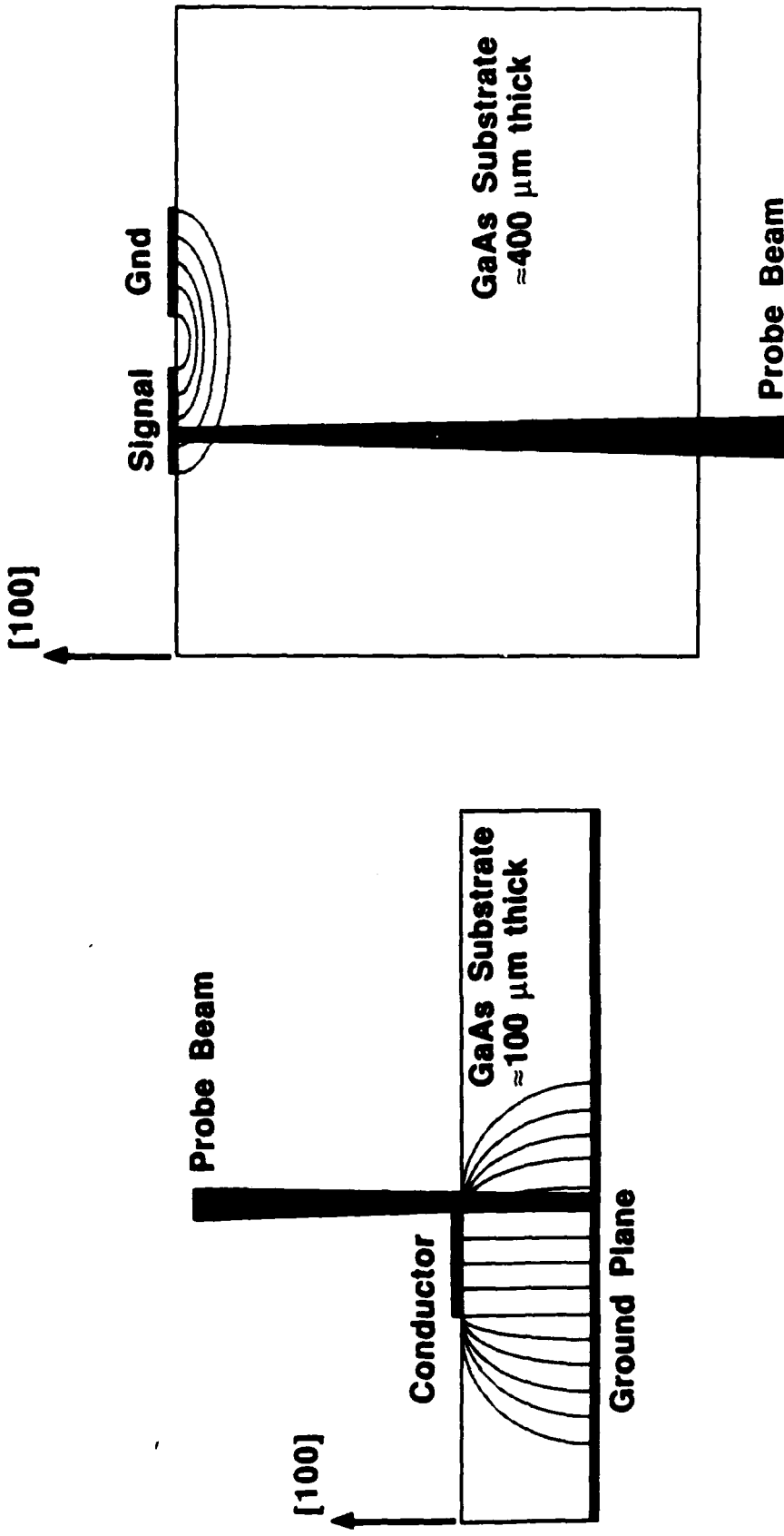


Figure 8: Reflection-mode probing geometries for electrooptic sampling of GaAs integrated circuits. The frontside geometry is used for probing microstrip transmission lines on MMIC's, while the backside geometry is used for probing planar transmission lines on MMIC's and interconnects lines on digital IC's.

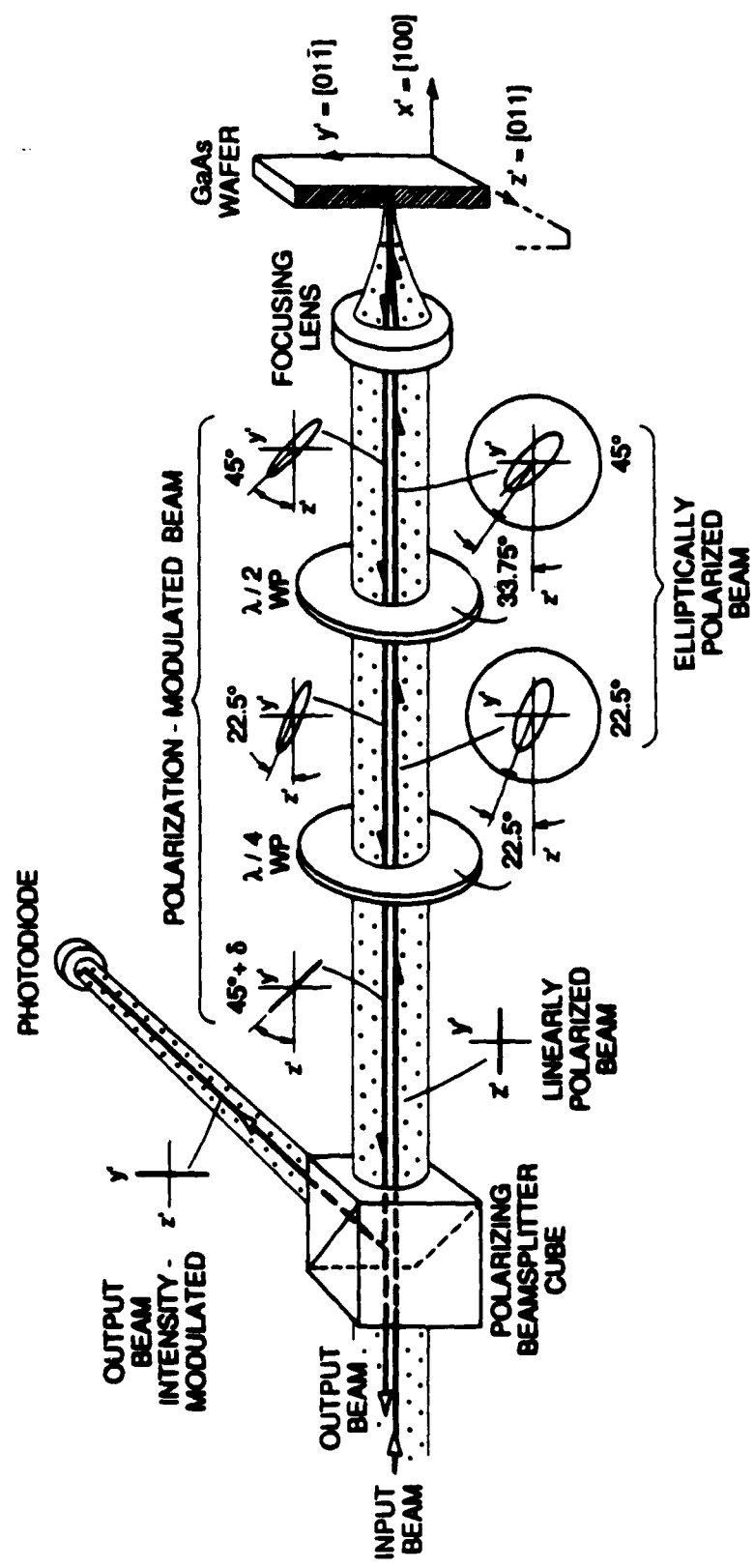


Figure 9: Coaxial arrangement for separation of incident and reflected beams in reflection-mode probing.

follows. A linearly polarized probe beam from the polarizing beamsplitter passes through a quarter-waveplate, oriented at 22.5° to the axis of the beamsplitter, producing an elliptical polarization. A half-waveplate oriented at 33.75° then rotates the elliptical polarization an additional 22.5° to align its major axis at 45° to the [011] direction of the GaAs substrate (i.e. oriented at 45° to the substrate cleave planes.) The on-axis probe beam is focused by a microscope objective next to a conductor (frontside probing) or on the conductor (backside probing.) The reflected beam passes back through the lens and the waveplates, producing a linear polarization at 45° to the axes of the polarizing beam-splitter, and the polarization component at 90° orientation is directed by the beamsplitter onto a photodiode. The probed conductor voltage changes the polarization of the return beam through the electrooptic effect by changing the *angle* of the linearly polarized light prior to the polarizer, and thus the intensity incident upon the photodiode. The resulting intensity varies as in Eqn. 10 where V_π is now

$$V_\pi = \frac{\lambda_0}{4n_0^3 r_{41}} \approx 5 \text{ kV} \quad (11)$$

giving twice the sensitivity for the reflection-mode cases. The on-axis return beam may be separated from the incident beam with a Faraday isolator. The signal from this beam is out-of-phase with the first beam allowing for differential detection to further improve signal sensitivity.

2.3. Electrooptic Sampling

The longitudinal reflection-mode geometries provide intensity modulation proportional to voltage for IC probing. With a continuous optical probe beam, the output intensity incident upon the photodiode will be a large steady-state intensity P_0 plus a small intensity change following the voltage of the probed conductor; microwave-frequency or picosecond-risetime signals on the probed conductor will result in microwave-frequency or picosecond-risetime modulation of the probe beam. Detection of this modulation would require a photodiode/receiver system with bandwidth comparable to that of the detected signal. With commercial sampling oscilloscopes limited to ~14 GHz and infrared photodiodes limited to ~20 GHz, the probing system's bandwidth would be insufficient for many high-speed and microwave GaAs circuits. In addition, the small modulation provided by the electrooptic effect would result in extremely poor signal-to-noise ratio using direct detection at microwave bandwidths, and thus very poor instrument sensitivity.

Mode-locked laser systems in conjunction with optical pulse compressors can generate extremely short optical pulses. At visible wavelengths, pulses as short as 6 fs [31,32] have been generated, while at the infrared wavelengths where GaAs is transparent, pulses as short as 33 fs have been generated [33,34]. Sampling techniques using a pulsed optical probe can achieve a time resolution set by the optical pulse duration and the circuit-probe interaction time, permitting instrument bandwidths exceeding 100 GHz. We describe repetitive sampling in the time domain as *synchronous sampling*, where equivalent-time measurements of the voltage waveforms are made in a manner similar to the operation of a sampling oscilloscope, and in the frequency domain as *harmonic mixing*, where the electrooptic sampler measures the amplitude and phase of sinusoidal voltages on probed conductors, similar to a microwave network analyzer.

In synchronous or equivalent-time sampling, an optical probe pulse with a repetition rate f_0 (set by the laser) samples a repetitive voltage waveform. If the waveform repeats at exactly $N \cdot f_0$, an integer multiple of the probe repetition rate, an optical pulse interacts with the waveform every N^{th} period at a fixed point within its cycle. Over many repetitions, the pulses sample the voltage waveform at the *same* time within the cycle, undergoing an equal modulation of each pulse's intensity. The resulting change in the average intensity of the probe beam, proportional to the signal, is detected by a photodiode receiver whose bandwidth is much less than the optical pulse repetition frequency. To detect the entire time waveform, the waveform frequency is increased by a small amount Δf (Figure 10.) The probe pulses are then slowly delayed with respect to the waveform, sampling successively delayed points, so that the average intensity at the photodiode changes in proportion to the waveform, but *repeating* at a rate Δf . The receiver then averages (low-pass filters) the photocurrent over a period much longer than $1/f_0$, eliminating the individual pulses. The averaged photocurrent i_{out} is then continuous and varies with $V(t)$, but at the slow repetition rate Δf

$$i_{\text{out}}(t) = I_0 \left[1 + \frac{\pi}{V_\pi} V \left(\frac{t \Delta f}{Nf_0 + \Delta f} \right) \right] \quad (12)$$

where I_0 is the average photodiode current. Typically f_0 is ~ 82 MHz, N varies from 1 to 500 for circuit drive frequencies to 40 GHz, and Δf is 10 to 100 Hertz. In contrast to pump/probe sampling, which has one probe pulse for every pump signal, the signal repeats N times between probe pulses in equivalent-time sampling. Because the pulse repetition rate is harmonically related to the signal repetition rate, Nyquist's sampling theorem (which states maximum recoverable signal bandwidth is half the sampling rate) does not apply in terms of setting the bandwidth of this measurement. Instead, the bandwidth is determined by the sampling pulselwidth, the relative jitter between sampling pulses, and the interaction time between the pulse and the signal. These factors are discussed in detail in Section 3.2.

The frequency domain description of equivalent-time sampling is known as *harmonic mixing*. The time domain signal detected by the photodiode receiver, proportional to the product of the laser signal and the measured signal in the time domain, has a frequency spectrum determined by the spectrum of the laser convolved with the spectrum of the measured signal [35]. In the frequency domain

$$\mathcal{F}\{P_{\text{out}}(t)\} = \mathcal{F}\{P(t)\} * \left[\delta(f) + \frac{\pi \mathcal{F}\{V(t)\}}{V_\pi} \right] \quad (13)$$

where \mathcal{F} is the Fourier transform operator, $P_{\text{out}}(t)$ is the intensity out of the polarizer, $P(t)$ is the laser intensity, $\delta(f)$ is the delta function, and $*$ represents the convolution operation. Figure 11 shows a schematic representation of this convolution for a mode-locked laser spectrum and a single microwave frequency signal. Scaled replicas of the signal appear in the laser intensity spectrum as amplitude-modulation sidebands around each laser harmonic. The magnitude and phase of the signal is recovered from the baseband harmonic with a low-frequency photodiode and a synchronous detector.

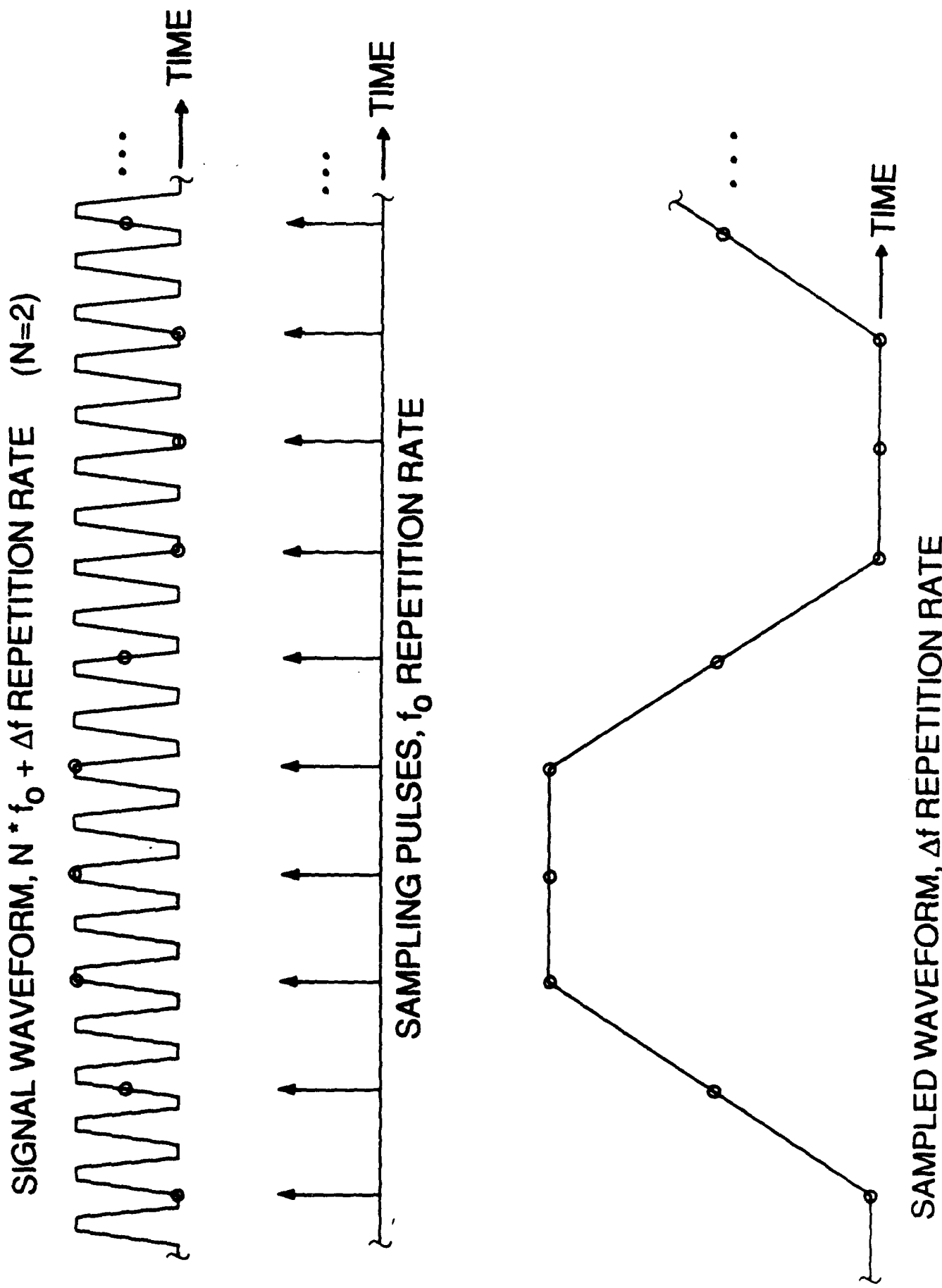


Figure 10: Equivalent-time sampling. Typically, $f_0 = 82$ MHz, $0 \leq N < 500$, and $\Delta f = 10$ Hz

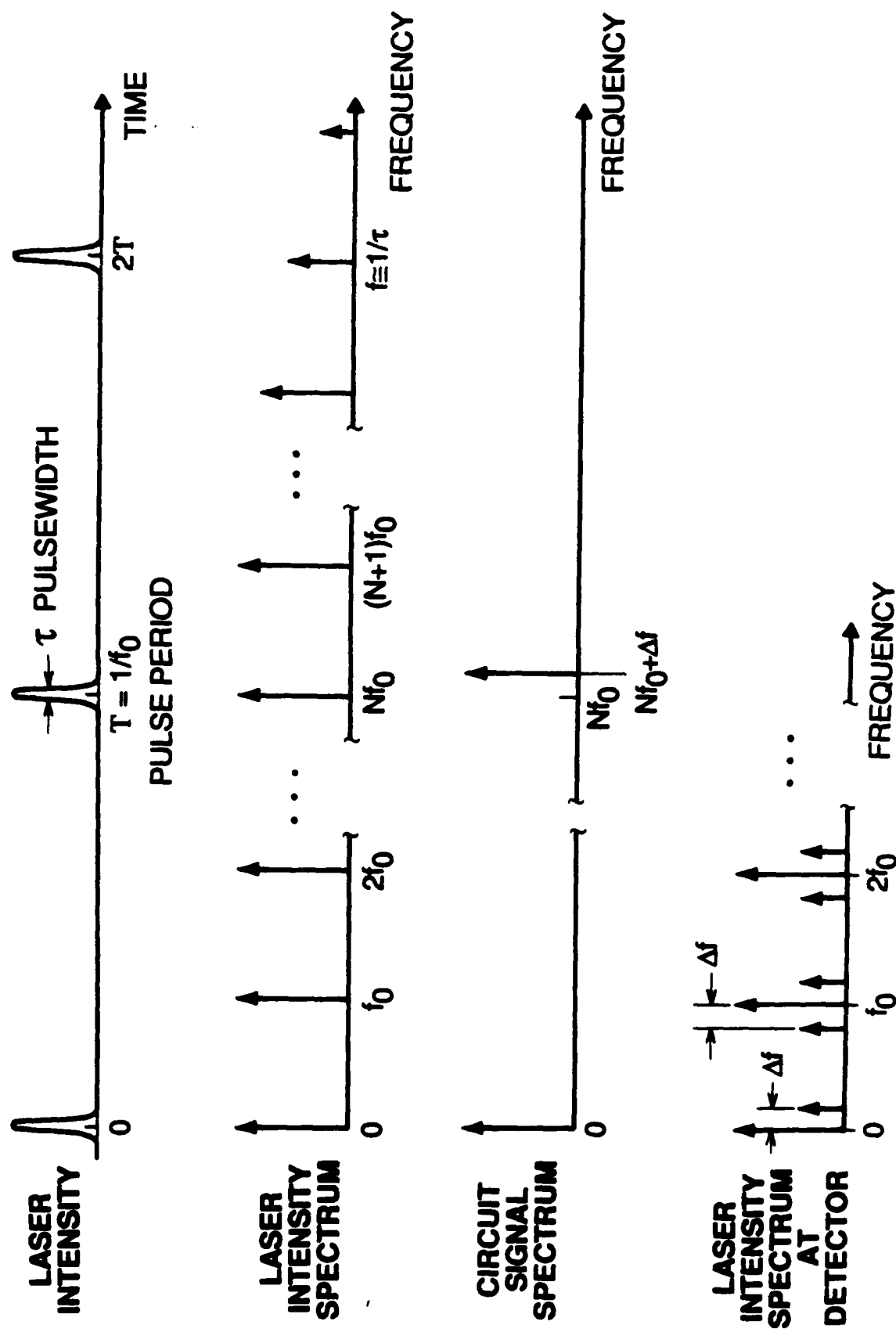


Figure 11: Electrooptic harmonic mixing.

3. System performance

3.1. System description

The sampling system, shown schematically in Figure 12, can be grouped into three sections; the laser system for optical pulse generation, the microwave instrumentation for driving the IC under test, and the receiver system for signal processing and data acquisition. The laser system consists of a mode-locked Nd:YAG laser, a fiber-grating pulse compressor, and a timing stabilizer feedback system. The Nd:YAG laser produces $1.06 \mu\text{m}$, 90 ps pulses at an 82 MHz rate with free-running pulse-to-pulse timing fluctuations of 4 ps rms, reduced to less than 300 fs rms by a phase-lock-loop feedback system [36,37] which synchronizes and stabilizes the laser pulse timing with respect to the microwave synthesizer. The fiber-grating pulse compressor shortens the pulses to 1.5 ps FWHM (full width at half maximum) [38,39,40]. The beam passes through a polarizing beamsplitter and two waveplates to adjust its polarization, then is focused through the IC substrate with a microscope objective to a $3 \mu\text{m}$ spot on the probed conductor (backside probing) or a $10 \mu\text{m}$ spot on the ground plane beneath and adjacent to the probed conductor (frontside probing.) The reflected light is analyzed by the polarizing beamsplitter and detected by a photodiode connected to a vector receiver.

To drive the IC, a microwave synthesizer generates either sinusoidal excitation for microwave circuits, or the clock/data signals for digital circuits. For wafer-level testing of IC's the drive signal is delivered with a microwave probe station (Cascade Microtech Model 42, Figs. 13&14) modified to allow for backside electrooptic probing. The transmission line probes used with this test station allow for launching a signal on the IC with repeatable, low reflection connections in a 50Ω environment to 40 GHz.

Signal processing is critical to achieve accurate, shot-noise limited measurements. Harmonic mixing is used for vector voltage measurements. The synthesizer is set to an exact multiple of the laser repetition rate plus a 1-10 MHz frequency offset, and the receiver is configured as a synchronous detector (i.e. an RF lock-in amplifier) to measure the magnitude and phase of the received signal at the frequency offset. Equivalent-time sampling is used to view time waveforms. The synthesizer is set to an exact multiple of the laser repetition rate (82 MHz), plus a small frequency offset Δf (1-100 Hz.) Pulse modulation, phase modulation, or fast offset/averaging signal processing as described in Section 3.3 is required to suppress laser intensity noise. The resulting signal varies at the slow offset rate Δf in proportion to the detected signal.

Direct electrooptic sampling has also been demonstrated using a mode-locked or gain-switched In-GaAsP injection laser to generate sampling pulses of 10-20 ps pulselength [41,42]. This system uses two synthesizers, referenced to a master clock, to drive the laser and to supply a signal to the IC. The longer pulselengths of the injection laser decrease the system's potential time resolution compared to the 1.5 ps pulselengths generated using the Nd:YAG/pulse compressor, but the injection laser pulses have sub-picosecond timing jitter and the laser is a very compact and stable optical source with a continuously tunable pulse repetition rate. This system has also been used to measure electrical signals in InP (indium phosphide) IC's [43].

Electrooptic Sampling System

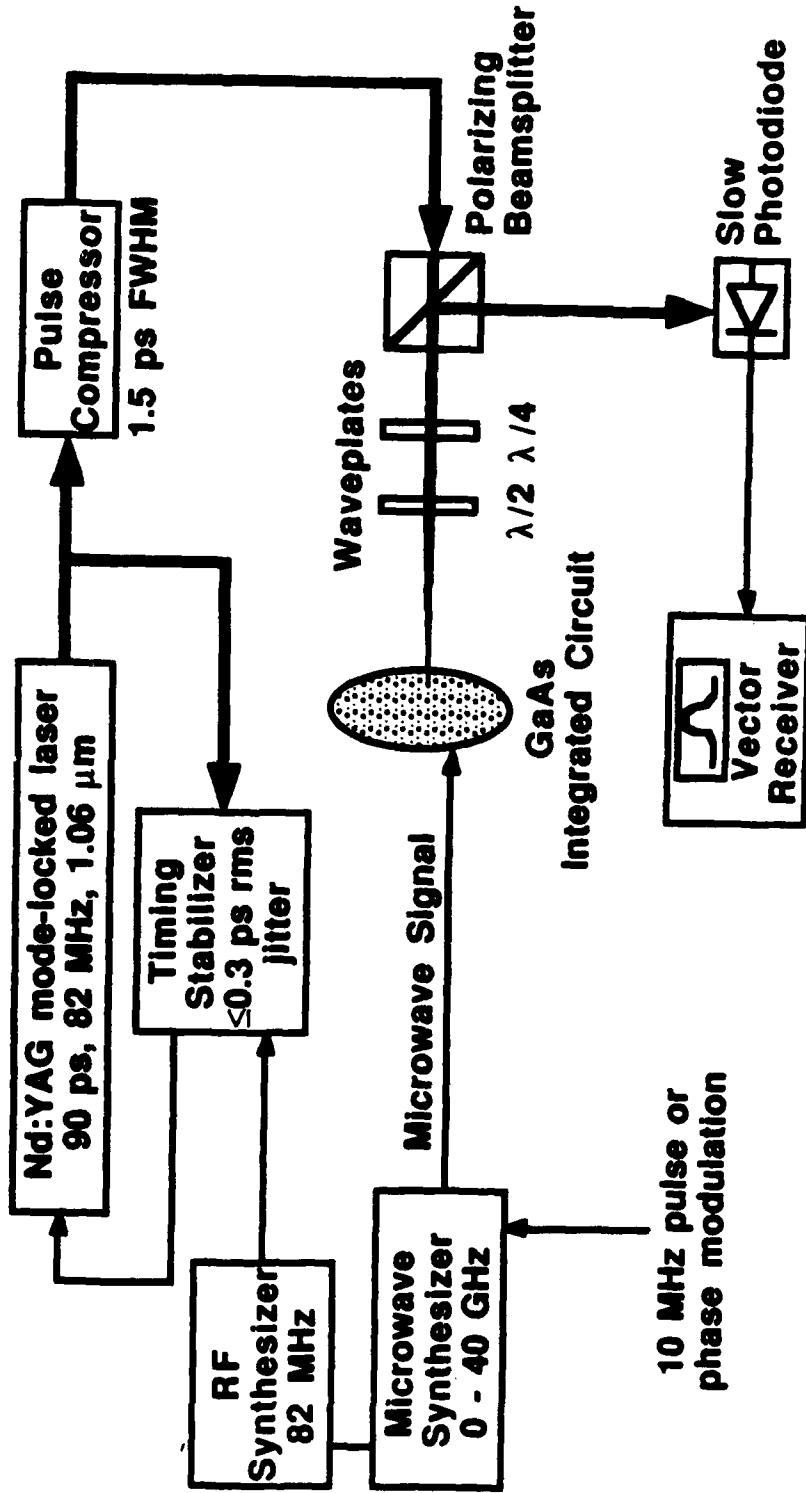


Figure 12: System for direct electrooptic sampling.

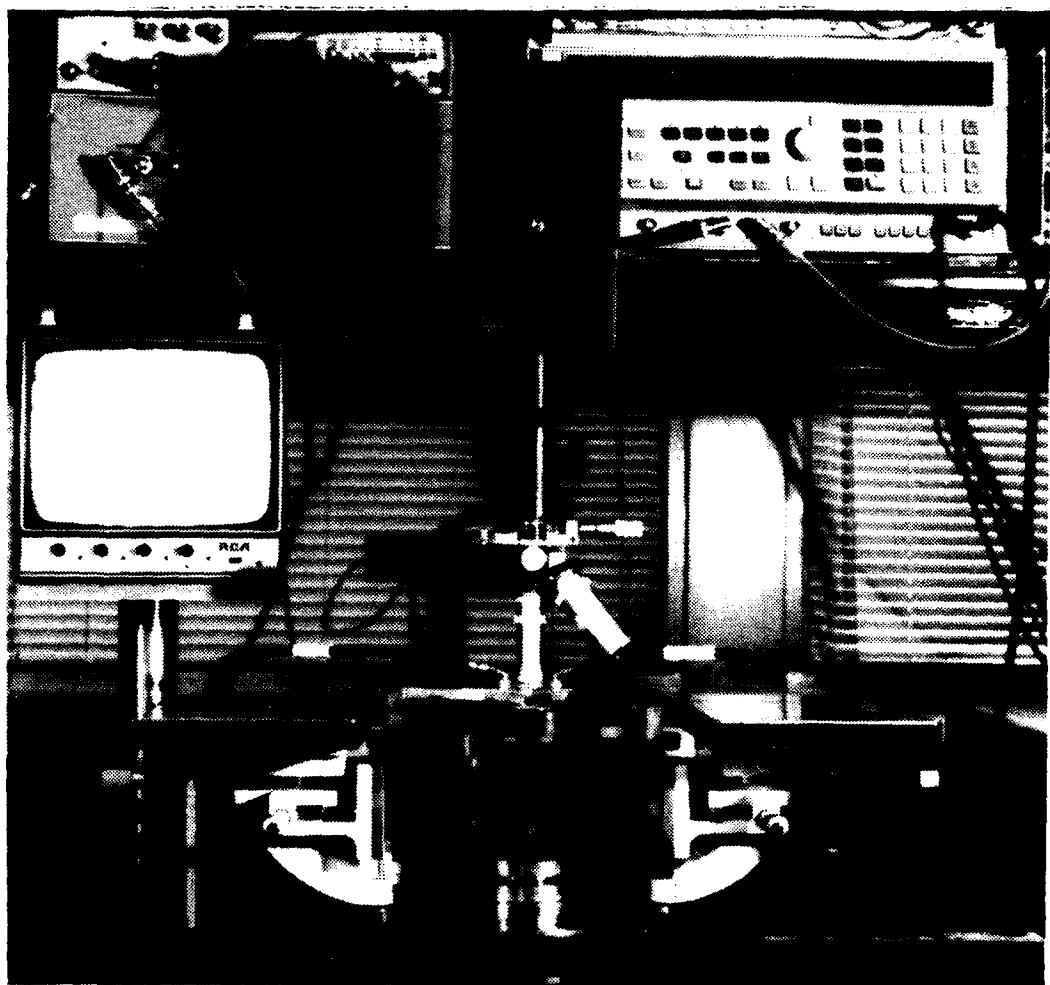


Figure 13: Overall view of Cascade microwave probe station modified for electrooptic sampling [6]

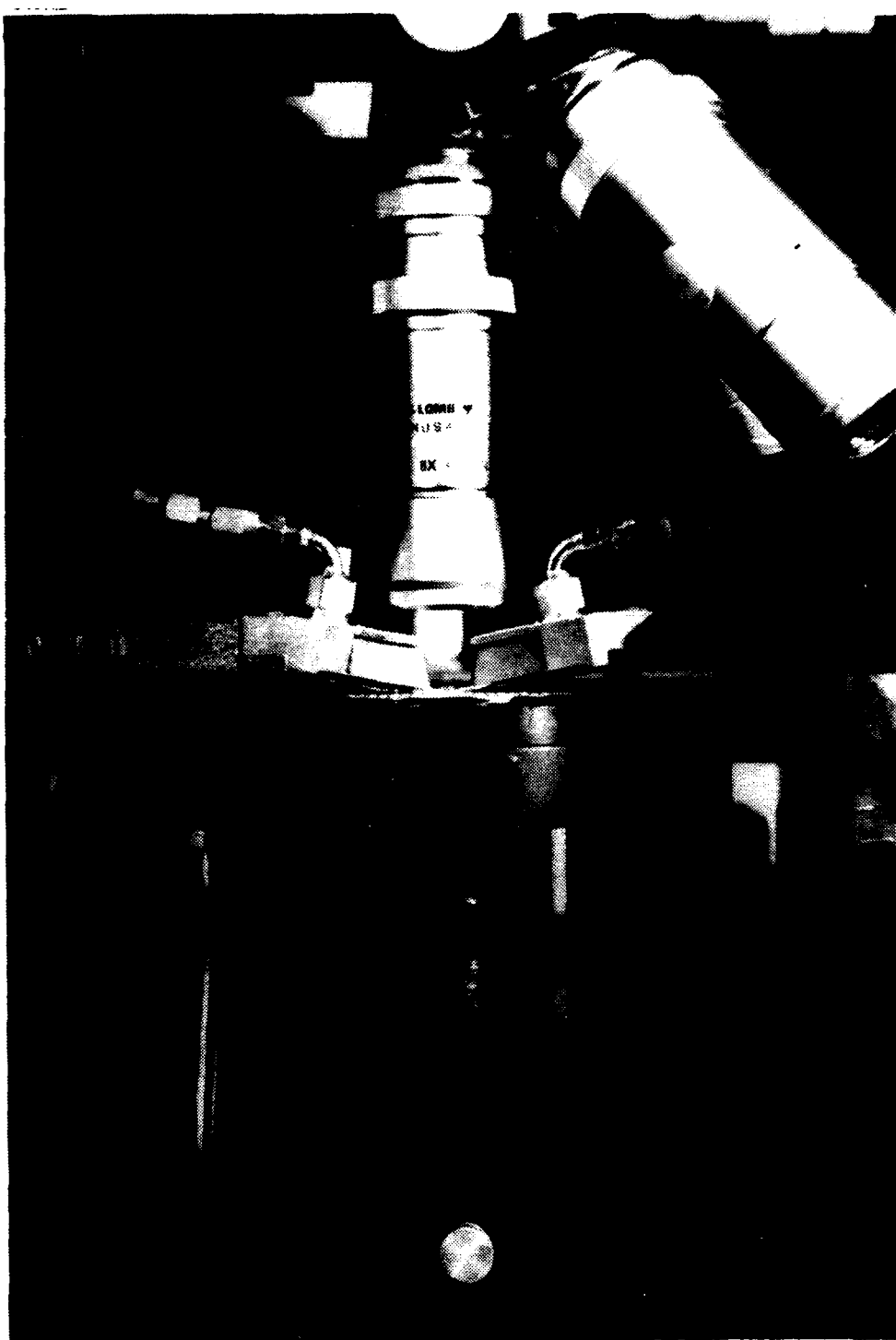


Figure 13: Cascade [6] microwave wafer probe station modified for electrooptic sampling.
b) View showing probe beam focusing objective below the wafer stage. The probe beam is focused on the IC through a hole or a sapphire window in the wafer stage.

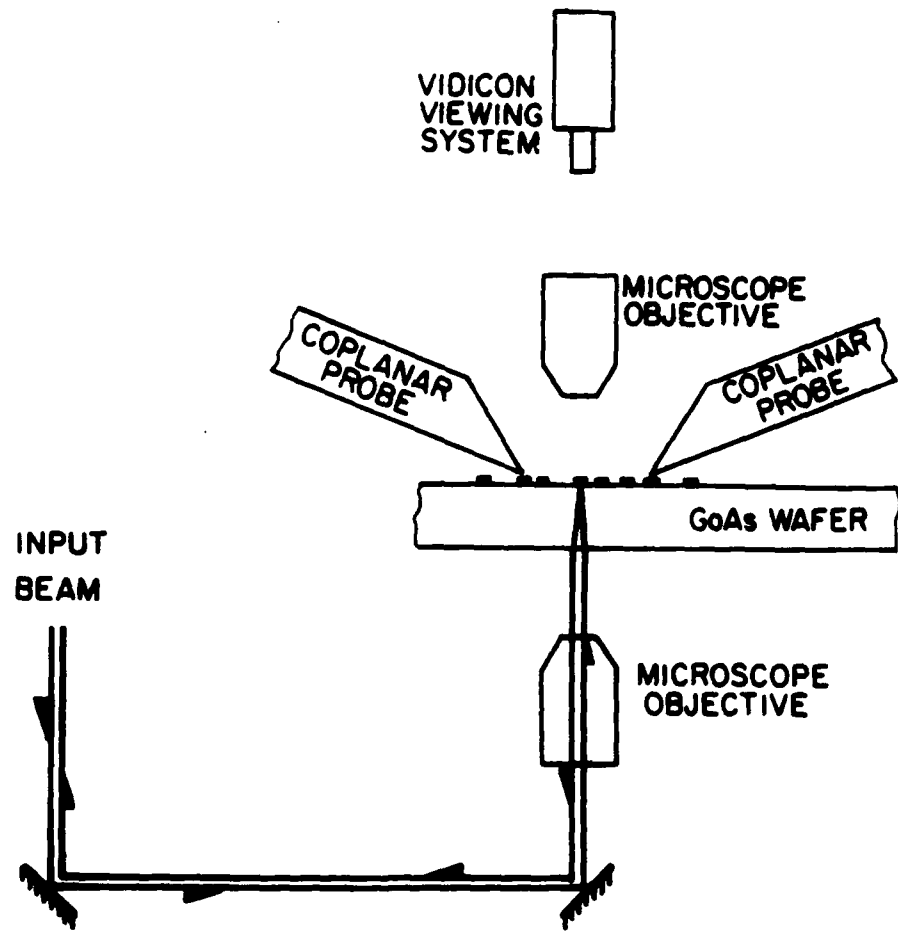


Figure 14: Schematic diagram of the beam path through the Cascade probe station.

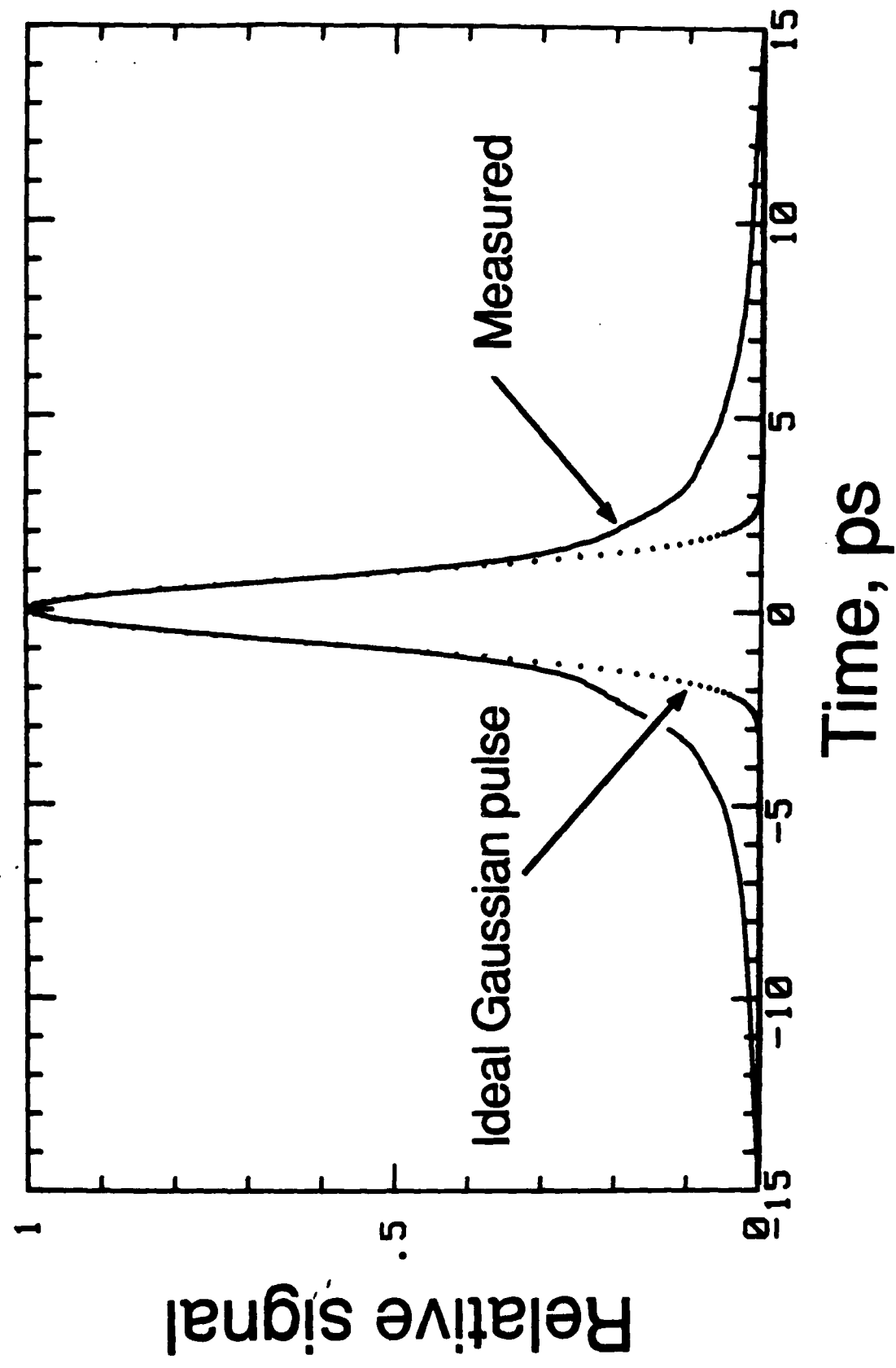


Figure 15: Autocorrelation of the 1.4 ps FWHM compressed pulse (solid line) and the autocorrelation of an ideal Gaussian pulse (dashed line.)

3.2. Bandwidth

The system's bandwidth or time resolution is determined by the optical pulsedwidth, the pulse-to-pulse timing jitter of the laser with respect to the microwave synthesizer driving the circuit, the interaction time of the probe pulse and the electrical signal, and the effective receiver response time. We assume Gaussian distributions for each term for simplicity. The overall time resolution is the root-mean-square sum of these values

$$\sigma_{\text{total}} = \sqrt{\sigma_{\text{PW}}^2 + \sigma_j^2 + \sigma_{\text{IT}}^2 + \sigma_{\text{REC}}^2} \quad (14)$$

where σ_{PW} is the rms optical pulsedwidth, σ_j is the rms pulse-to-pulse timing jitter, σ_{IT} is the rms interaction time of the pulse through substrate, and σ_{REC}^2 is the effective receiver impulse response time.

The relation between the time resolution and the frequency bandwidth for the optical pulse is given by

$$\sigma_{\text{FWHM}} = \frac{0.312}{f_{3\text{dB}}} \quad (15)$$

where for a Gaussian pulseshape $\sigma_{\text{FWHM}} = 2.35 * \sigma_{\text{rms}}$ is the full width at half-maximum (optical pulsedwidth is typically measured in terms of its FWHM, not its rms value), and $f_{3\text{dB}}$ is the half power frequency. This time-bandwidth product is reduced by a factor of $1/\sqrt{2}$ from the time-bandwidth product of 0.441 due to the square-law photodiode detector, i.e. the optical intensity of the pulse is converted to a voltage in the receiver with a resulting power spectrum related to the square of this voltage.

The 90 ps pulsedwidth from the Nd:YAG laser results in a bandwidth of 3.5 GHz, clearly not suitable for high bandwidth circuit measurements. To reduce the pulsedwidth, a fiber-grating pulse compressor is used [38,39,40]. This system, based on the Kerr effect or self-phase modulation in a single-mode optical fiber, generates a frequency chirp on the laser pulse as it propagates through the fiber. The light emerging from the fiber is red-shifted on its leading edge and blue-shifted on its trailing edge with the frequency varying across the pulse duration in proportion to the derivative of the intensity envelope. For a Gaussian intensity pulseshape (characteristic of some mode-locked lasers) the frequency chirp is nearly linear over the center of the pulse. These new frequency components are recombined into a compressed pulse by passing the light through a grating pair, where the time-of-flight delay is linearly proportional to the light's wavelength, thus acting as a dispersive delay line where the red-shifted leading frequency components are delayed with respect to the blue-shifted trailing frequencies. The wavelength-dependent delay is adjusted by the separation of the gratings to match the frequency chirp of the light, producing a compressed pulse.

A number of effects limit the amount of pulse compression available with this technique; stimulated Raman scattering limits the maximum optical power focused into the fiber core, and deviation from a linear frequency chirp on the pulse due to non-ideal input pulseshapes can generate long pedestals on an otherwise short compressed pulse. Using a fiber length of 1 km in the pulse compressor, the group velocity dispersion enhances the region of linear frequency chirp [39], and the pulses from the mode-locked Nd:YAG laser are routinely compressed to 1.5 ps, a factor of 60:1. Using two-stage optical compression, pulses as short as 200 fs at 1.06 μ m have been generated [34].

The compressed pulsedwidth, as measured with an optical autocorrelator, deviates from the autocorrelation of an ideal Gaussian pulseshape as evidenced by slight "wings" or pedestals on the pulse due to the non-ideal frequency chirp of input pulse (Figure 15). The group velocity dispersion of the relatively long 1 km fiber reduces the pulse pedestals compared to shorter fiber lengths [39]. A Gaussian pulse of 1.4 ps FWHM duration has spectral content extending past 200 GHz, while the spectral content of the compressed pulse deviates from an ideal Gaussian pulse, where the power spectral density is determined by numerically Fourier transforming the autocorrelation (Figure 16) [35]. The wings on the compressed pulse may be further reduced by "spectral windowing" [44] to remove part of the nonlinear frequency chirp or polarization discrimination of the compressed pulse [45].

Timing jitter influences both bandwidth and sensitivity; the impulse response of the sampling system is the convolution of the optical pulseshape with the probability distribution of its arrival time (neglecting optical transit time), while those Fourier components of the jitter lying within the detection bandwidth of the receiver introduce noise proportional to the time derivative of the measured waveform (Section 3.3). Stabilization of the laser timing is thus imperative for low-noise measurements of microwave or picosecond signals. The timing fluctuations of the laser are suppressed by phase-locking the laser to a high-stability reference oscillator [36,37]. Figure 17 shows the block diagram of the feedback system. A photodiode monitors the 82 MHz laser pulse train, and the phase of its fundamental component is compared with that of the reference oscillator, generating a phase error signal. The 41 MHz signal required for driving the laser's acousto-optic (A-O) cell is generated by frequency division from the 82 MHz standard; its timing (phase) is adjusted with a voltage-controlled phase-shifter controlled by the amplified and frequency-compensated phase error signal. Given an error-free phase detector, the laser timing fluctuations are suppressed in proportion to the loop gain of the feedback system. Figure 18 shows the measured phase noise of one harmonic of the laser with an HP 8662 low-phase noise synthesizer as the reference for the feedback system. From this measurement the time jitter is calculated (see Section 3.3, Equation 26) to be less than 300 fs rms.

The interaction time of the optical pulse and electrical signal in the GaAs substrate comes from several factors; the response time of the electrooptic effect, the electrical transit time, and the optical transit time. The electrooptic effect in GaAs arises primarily from its electronic polarizability and is intrinsically very fast (see Auston, this issue), with a response time on the order of 10 femtoseconds. The electrical transit time is the propagation time of the electrical signal as it traverses the spatial extent of the probe beam. For typical IC values this time is on the order of 60 fs [27]. The optical transit time is the propagation time of the optical pulse as it traverses the electric fields within the GaAs substrate. For frontside probing of microstrip lines, where the field is uniform though the

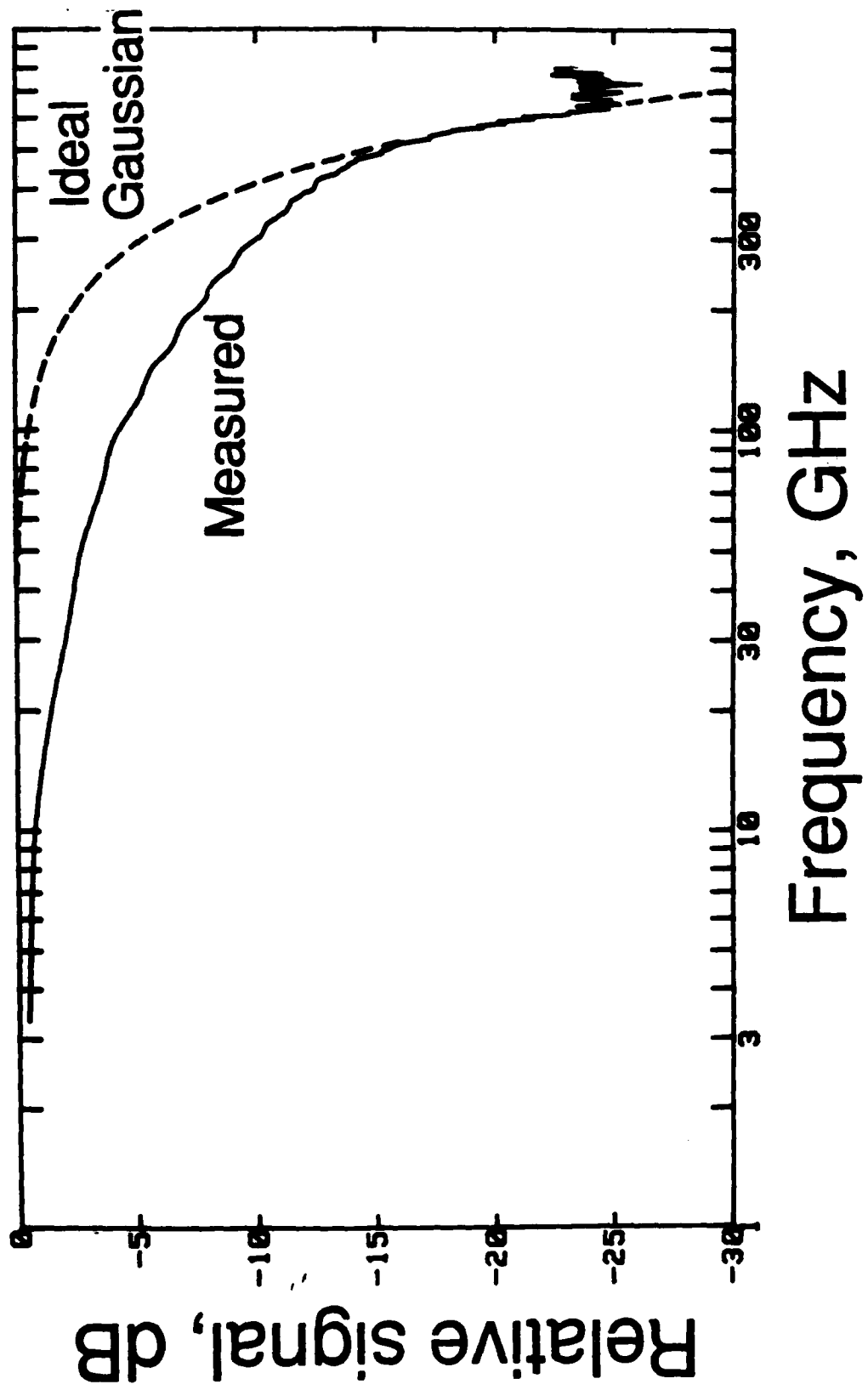


Figure 16. Power spectral density of the compressed pulse (solid line) and an Gaussian pulse (dashed line). The power spectral density is the Fourier transform of the autocorrelation.

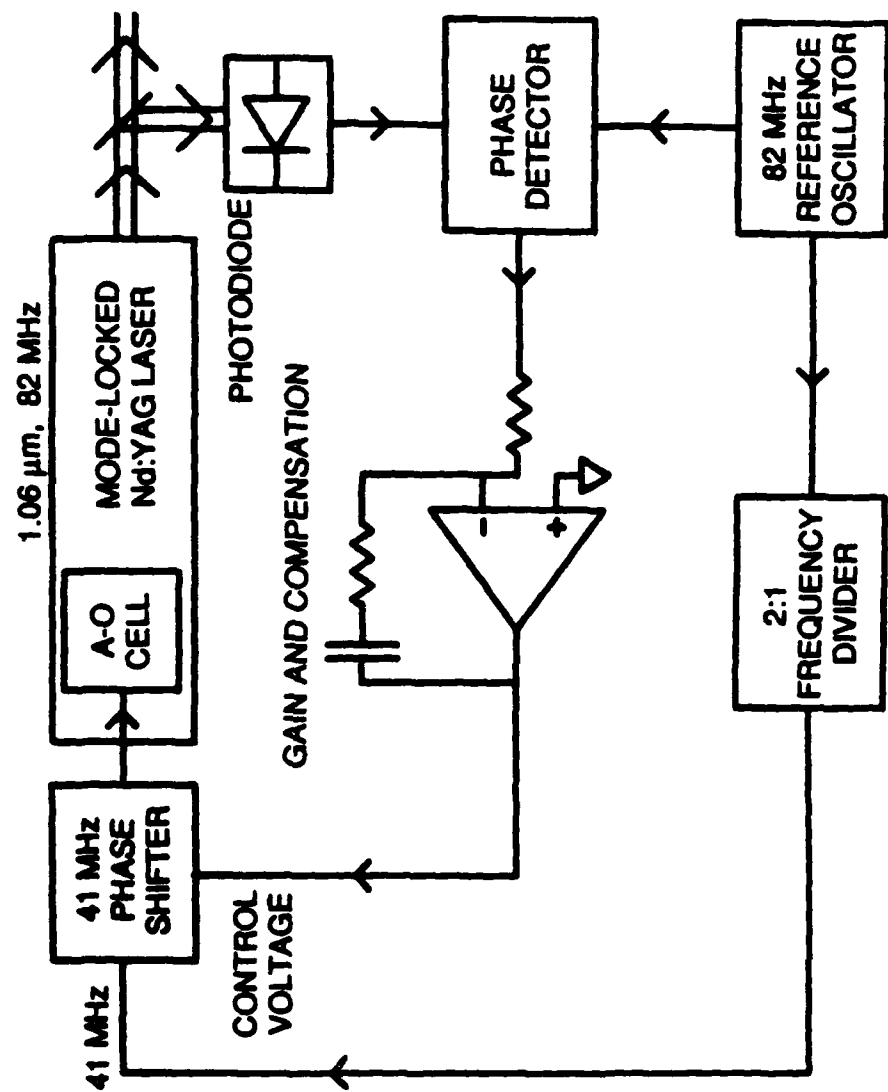


Figure 17: Block diagram of the phase-lock-loop timing stabilizer feedback system.

Center 1.64 GHz 1 kHz/div Resolution 100 Hz

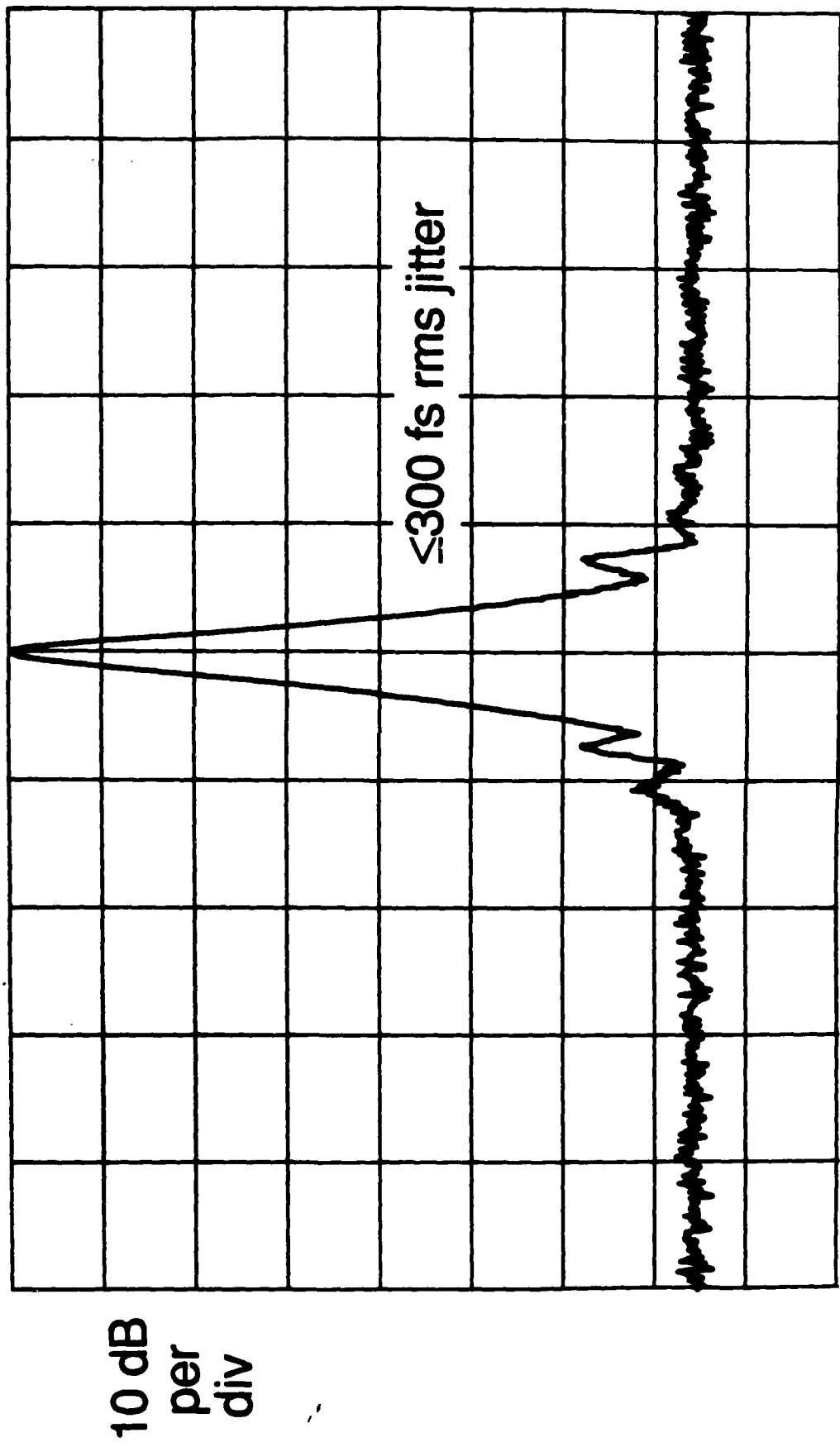


Figure 18: Laser phase noise at the 20th harmonic of the pulse repetition rate, measured with a photodiode and a spectrum analyzer. The noise floor of this measurement is instrumentation limited, giving an upper limit for timing jitter of 300 fs rms.

Low-frequency Laser Intensity Noise Spectrum

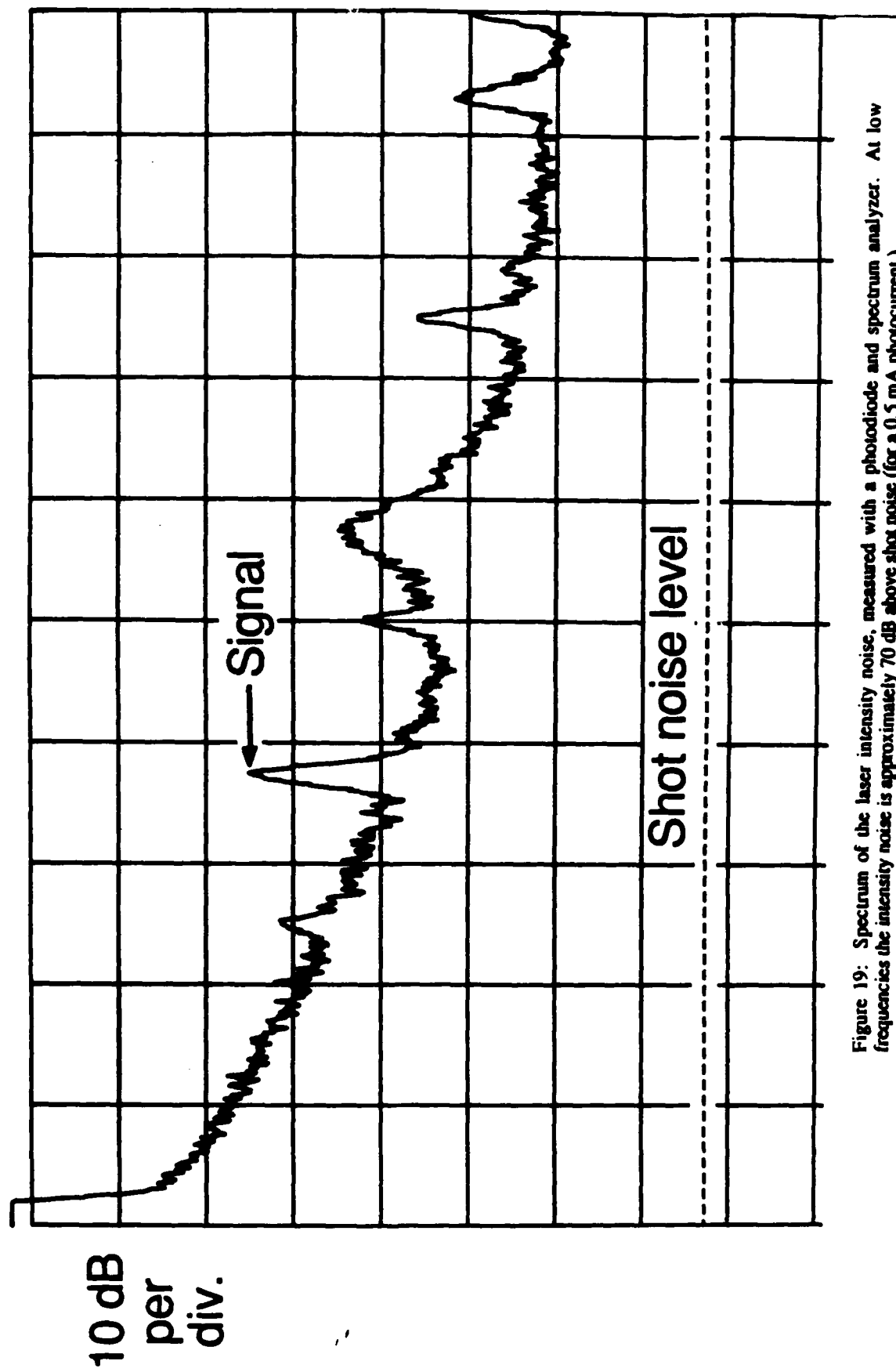


Figure 19: Spectrum of the laser intensity noise, measured with a photodiode and spectrum analyzer. At low frequencies the intensity noise is approximately 70 dB above shot noise (for a 0.5 mA photocurrent.)

substrate, the optical transit time is proportional to the substrate thickness. For backside probing of coplanar transmission lines or planar interconnections, the electric field is not uniform in the substrate and the characteristic depth of the electric fields is on the order of the conductor spacing; in this case the optical transit time is not a function of substrate thickness, but is proportional to the conductor spacing. Because the optical and microwave dielectric constants in GaAs are nearly equal, microwave transmission lines have a cutoff frequency for higher-order modes roughly equal the inverse of the optical transit time. Well-designed microwave circuits operate at frequencies well below the multimode cutoff frequency. Only when measuring interconnects near or above the cutoff frequency (where dispersive characteristics are of interest) must the optical transit time be considered. For example, the optical transit time for a 125 μm thick substrate, typical of MMIC's operating at frequencies below 40 GHz, is 3 ps, corresponding to a 3 dB response rolloff of >100 GHz.

The effective receiver impulse risetime arises from the constraint put on the receiver bandwidth by the required system sensitivity. We assume for analysis the receiver has a Gaussian impulse response

$$h(t) = \frac{1}{\sqrt{2\pi}\sigma_t} \exp\left(\frac{-t^2}{2\sigma_t^2}\right) \quad (16)$$

where σ_t is the rms duration. Then, the receiver frequency response

$$H(f) = \exp\left(\frac{-f^2}{2B_{\text{acq}}^2}\right) \quad (17)$$

has an rms signal acquisition bandwidth $B_{\text{acq}} = 1/2\pi\sigma_t$. Because the sampled signal at frequency Nf_0 is translated to a lower frequency Δf at the receiver (Eqn. 12), the effective receiver impulse response for synchronous sampling is

$$\sigma_{\text{REC}} = \frac{\Delta f}{Nf_0} \sigma_t = \frac{\Delta f}{Nf_0 2\pi B_{\text{acq}}} \quad (18)$$

Given a required time resolution σ_{total} from the electrooptic sampling system, the data acquisition rate of the sampler is then limited. For a fixed time resolution, larger receiver bandwidths B_{acq} (or shorter receiver time constants) permit faster waveform acquisition rates, but degrade the measurement sensitivity.

3.3. Sensitivity

If the measurement bandwidth provided by the electrooptic sampler is to be useful, the instrument must also provide sufficient sensitivity to observe signal voltages typical of high-speed GaAs circuits. As in any system, sensitivity is determined by the signal to noise ratio; the instrument's sensi-

tivity, or minimum detectable voltage, is the probed voltage which results in a measured signal equal to the measurement system's noise signal. Most noise sources have power spectral densities which are independent of frequency ("white" noise), resulting in a noise voltage proportional to the square root of the signal acquisition bandwidth B_{acq} and a minimum detectable voltage expressed in units of volts per root Hertz ($\text{V}/\sqrt{\text{Hz}}$.) Smaller minimum detectable voltages permit more rapid measurement acquisition for fixed measurement accuracy. With appropriate system design and signal processing, the various sources of noise in the electrooptic sampler can be reduced or eliminated, permitting low-noise voltage measurements with fast data acquisition.

The fundamental limiting noise source in electrooptic sampling is the shot noise of the probe beam (observed as shot noise of the photodiode quiescent current.) The signal generated by the photodiode (dropping the constant term I_0) from Eqn. 12 is

$$i_{\text{out}}(t) = \frac{I_0\pi}{V_\pi} \sqrt{\left(\frac{t \Delta f}{Nf_0 + \Delta f}\right)} + i_{\text{SN}} \quad (20)$$

The shot noise, i_{SN} , associated with the DC component of the photodiode current has a variance given by

$$\overline{i_{\text{SN}}^2} = 2qI_0B_{\text{eq}} \quad (21)$$

where q is the electron charge, the horizontal bar denotes the statistical expectation, and

$$B_{\text{eq}} = \sqrt{\pi/2} B_{\text{acq}} \quad (22)$$

is the receiver's equivalent noise bandwidth. Setting the signal current $I_0\pi V_{\text{min}}/V_\pi$ equal to the shot noise current, and normalizing to $B_{\text{eq}} = 1 \text{ Hz}$ acquisition bandwidth, the minimum detectable voltage is

$$V_{\text{min}} = \frac{V_\pi}{\pi} \sqrt{\frac{2q}{I_0}} \quad \frac{\text{Volts}}{\sqrt{\text{Hz}}} \quad (23)$$

For the reflection-mode probing geometries, $V_\pi \approx 5 \text{ kV}$, while the average photocurrent I_0 is typically 1 mA. Then, the minimum detectable voltage is

$$V_{\text{min}} = 30 \text{ } \mu\text{V}/\sqrt{\text{Hz}} \quad (24)$$

Typically, $V_{\text{min}} \approx 70 \text{ } \mu\text{V}/\sqrt{\text{Hz}}$ is observed experimentally (at 1 mA average photocurrent) due to ≈ 10 dB of residual noise from the system (dominated by excess amplitude noise from the pulse compressor); this sensitivity is sufficient to acquire measurements at scan rates of 10-100 Hz with a noise floor of a few millivolts. The actual measurement system has a number of additional noise sources to contend with to achieve $70 \text{ } \mu\text{V}/\sqrt{\text{Hz}}$ sensitivity. These include timing jitter of the laser (phase

noise), intensity noise of the probe beam from low frequency laser fluctuations and from the pulse compressor, and receiver noise.

Low-frequency fluctuations in the mode-locked laser introduce noise into the received photocurrent. Fluctuations in the mode-locked Nd:YAG laser include variations in both pulse intensity and pulse timing. The laser produces a train of pulses approximated by

$$P(t) = \frac{P_0}{f_0} [1 + N(t)] \sum_{m=-\infty}^{+\infty} \delta[t - m/f_0 - J(t)] \quad (25)$$

where $N(t)$ is the normalized pulse intensity fluctuation and $J(t)$ is the pulse timing fluctuation. The laser intensity then has a power spectral density $S_p(f)$ approximated to second order in $mf_0\sigma_J$ by

$$S_p(f) = P_0^2 \sum_{m=-\infty}^{+\infty} \{ [1 - (2\pi mf_0\sigma_J)^2] \delta(f - mf_0) + [1 - (2\pi mf_0\sigma_J)^2] S_N(f - mf_0) + (2\pi mf_0)^2 S_J(f - mf_0) \} \quad (26)$$

where $S_N(f)$ is the power spectral density of $N(t)$ and $S_J(f)$ is the power spectral density of $J(t)$. The spectrum of the laser intensity is a series of discrete spectral lines at multiples of f_0 , plus spectra resulting from the timing and amplitude fluctuations, referred to as amplitude-noise sidebands [$S_N(f - mf_0)$] and phase-noise sidebands [$(2\pi mf_0)^2 S_J(f - mf_0)$]. By monitoring the laser intensity with a spectrum analyzer and measuring the relative powers of the laser harmonic and its noise sidebands as a function of the order of the harmonic, the spectral densities of $N(t)$ and $J(t)$ are measured.

With these amplitude and timing fluctuations, the received photocurrent $i_{out}(t)$ is

$$i_{out}(t) \approx I_0 + \frac{I_0 \pi}{V_\pi} V \left(\frac{t \Delta f}{Nf_0 + \Delta f} \right) + i_{laser,0} + i_{laser,1} + i_{phase} \quad (27)$$

where

$$i_{laser,0} = I_0 N(t) \quad (28)$$

is the zero-order (background) received noise current due to laser intensity fluctuations,

$$i_{laser,1} = N(t) \frac{I_0 \pi}{V_\pi} V \left(\frac{t \Delta f}{Nf_0 + \Delta f} \right) \quad (29)$$

is a received noise current arising from the product of the laser intensity fluctuations and the signal voltage, and

$$i_{\text{phase}} = \frac{I_0 \pi}{V \pi} J(t) V' \left(\frac{t \Delta f}{Nf_0 + \Delta f} \right) \quad (30)$$

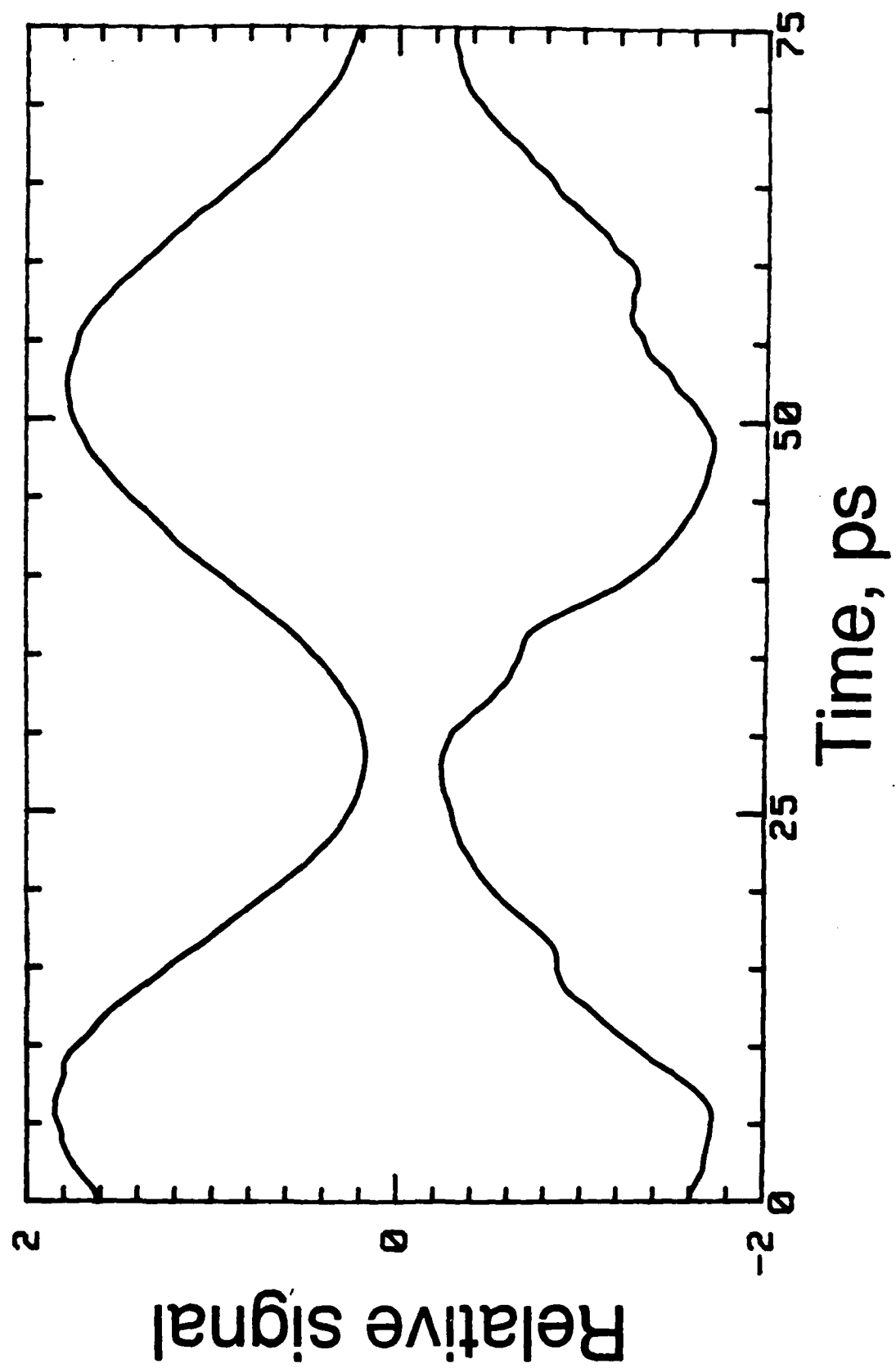
is the noise arising from the laser timing fluctuations, where $V'(t)$ is the time derivative of $V(t)$. We have assumed that $\Delta f \ll Nf_0$, and have omitted terms in $N(t)J(t)$, as these are negligible.

The spectral density $S_N(f)$ of the laser intensity noise $N(t)$ is shown in Figure 19. At frequencies below ~ 1 kHz, the laser intensity noise is approximately 70 dB greater than the shot noise of a 0.5 mA receiver photocurrent. At higher frequencies the noise power decreases, reaching an asymptote 5-15 dB above the shot noise level at frequencies greater than ~ 100 kHz. The excess noise at frequencies above 100 kHz arises from Raman scattering and polarization noise in the optical pulse compressor. If the sampled signal were detected at a low frequency, the zero-order laser intensity noise $i_{\text{laser},0}$ would contribute a 10³:1 degradation to the minimum detectable voltage. To suppress the zero-order laser intensity noise, the excitation to the circuit under test is modified so that the received photocurrent $i_{\text{out}}(t)$ has a spectral component, with amplitude proportional to the probed voltage, at a frequency above the 100 kHz 1/f noise corner frequency. One method is pulse modulation (chopping) of the drive signal. The received photocurrent then has a spectral component at the chopping rate whose amplitude varies in proportion to the sampled point on the signal waveform. The chopping frequency is set from 1-10 MHz, well above the 1/f noise corner frequency, to achieve near-shot-noise limited detection.

Driving digital IC's requires modification of the pulse modulation scheme, since most digital circuits require continuous drive signals for their clocks. One alternative is phase modulation of the drive signal, corresponding to controlled jitter in time, at the chopping frequency. The received photocurrent then has a component at the chopping frequency whose amplitude is proportional to the time derivative of the sampled signal, and is recovered by integration [46]. The drawbacks to this technique are circuit sensitivity to clock jitter (usually negligible) and a reduction in the signal-to-noise ratio (due to the differentiation) by a factor of the square root of the acquisition bandwidth. A second signal recovery scheme, termed fast offset and averaging, relies on increasing the frequency offset Δf to a rate above the low-frequency laser noise, 100 to 200 kHz. The signal is recovered by high-pass filtering to remove the low-frequency laser noise, then by signal averaging at the offset rate Δf . If the received signal is averaged at the scan rate, the sensitivity using fast averaging is the same as for simple synchronous sampling with the same measurement acquisition time. Commercial digitizing oscilloscopes have limited averaging rates; at scan rates of 100-200 kHz, most instruments can average a maximum of only 100-200 scans per second, corresponding to a signal-to-noise reduction of 30 dB from averaging at the fast scan rate. Even so, we have demonstrated the feasibility of this technique using a commercial digitizing oscilloscope, and the signal-to-noise reduction, compensated for by increased measurement acquisition time, is justified for testing IC's that are sensitive to signal chopping.

The two remaining noise terms arising from laser low-frequency fluctuations, $i_{\text{laser},1}$ and i_{phase} , are not suppressed by signal chopping or signal phase modulation. Because these noise terms arise from the products $N(t)V(\alpha t)$ and $J(t)V'(\alpha t)$, their power spectra are proportional to the convolutions $S_N(f)*S_V(f/\alpha)$ and $S_J(f)*f^2 S_V(f/\alpha)$, respectively, where $S_V(f)$ is the power spectrum of $V(t)$.

Figure 20: 20 GHz sampled signal with (upper trace) and without (lower trace) timing stabilizer.



Pulse-modulation or phase-modulation of $V(t)$ at a frequency f_{mod} results in a received photocurrent having spectral components at f_{mod} arising from both $V(t)$ and from the multiplicative laser amplitude noise $i_{\text{laser},1}$ and the received phase noise i_{phase} . Instead, these noise terms must be suppressed by laser stabilization. The laser timing stabilizer reduces $S_J(f)$ by 20-25 dB at frequencies lying within typical receiver bandwidths B_{rec} of 10 Hz-1 kHz. Figure 20 shows the resulting suppression of received phase noise on a 20 GHz sampled signal. The multiplicative amplitude noise $i_{\text{laser},1}$ can be suppressed by feedback stabilization of the laser intensity [47]. As the multiplicative amplitude noise scales with the signal voltage $V(t)$, without laser amplitude stabilization it is a significant source of measurement error in the electrooptic sampling system for signal voltages larger than ≈ 1 V.

Additional noise arises from the receiver, which has an equivalent input noise current

$$\overline{i_{\text{receiver}}^2} = \frac{4kTB_{\text{eq}}}{R_L} + \overline{i_{\text{amp}}^2} + \frac{1}{R_L^2} \overline{v_{\text{amp}}^2} \quad (31)$$

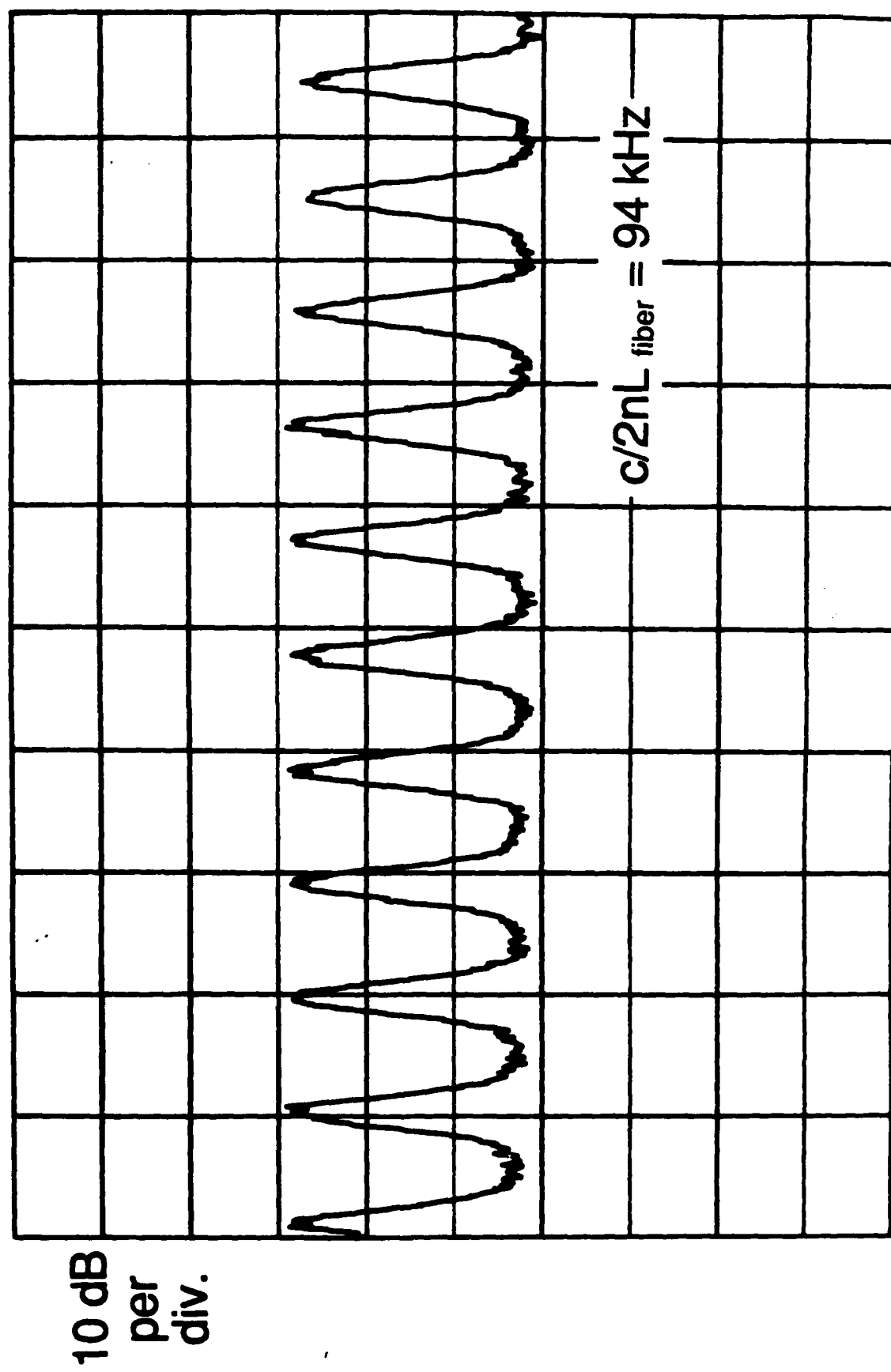
where k is Boltzmann's constant, T is the absolute temperature, and R_L is the photodiode load resistor. The first term is the Johnson or thermal noise of the load resistor, and $\overline{i_{\text{amp}}^2}$ and $\overline{v_{\text{amp}}^2}$ are the equivalent input noise current and equivalent input noise voltage of the amplifier following the photodiode. Receiver noise is reduced to a level below the shot noise limit by appropriate receiver design; R_L is made large in comparison with $2kT/qI_0$ so that Johnson noise is well below shot noise and the photodiode amplifier is selected for low input noise.

The pulse compressor introduces excess amplitude noise due to stimulated Raman scattering (SRS) and temperature-induced polarization drift in the non-polarization-preserving fiber [48]. We observe the broadband background amplitude noise increase dramatically (20-40 dB) above the shot noise limit as the input power to the fiber approaches the Raman threshold. A periodic structure to the noise spectrum (Figure 21) corresponds to the free spectral range of the 1 km fiber. We attribute this effect to a parasitic synchronously pumped fiber-Raman laser formed by the 4% Fresnel reflection at each fiber end facet and the high gain of the 1.06 μm pumped SRS [49,50]. Self-phase modulation (SPM) occurs over the entire length of the fiber while the interaction length for SRS is set by the dispersion-induced walkoff between the input and Stokes-shifted wavelengths, approximately 60 meters. This dispersion also causes the 1.06 μm pump and the 1.12 μm Raman pulse to separate by 1.8 ns over the length of the 1 km fiber. If the weakly reflected Raman pulse is synchronized to within 1.8 ns of a pump pulse it is further amplified after its first round trip through the fiber. With this condition the Raman threshold with the 1 km fiber is 400 mW average power from the fiber output. Trimming the fiber length a few inches defeats this synchronism and increases the Raman threshold to 700 mW. We routinely obtain 60X compression ratios at power levels (350 mW average power from the fiber output) well below the Raman threshold.

In addition to SRS the fiber generates broadband polarization noise, possibly arising from guided acoustic wave Brillouin scattering [51] or intensity-induced polarization fluctuations [45]. The polarization noise is converted to amplitude noise after passing through the grating pair in the compressor. Adjusting the polarization from the fiber to maximize transmission through the grating path

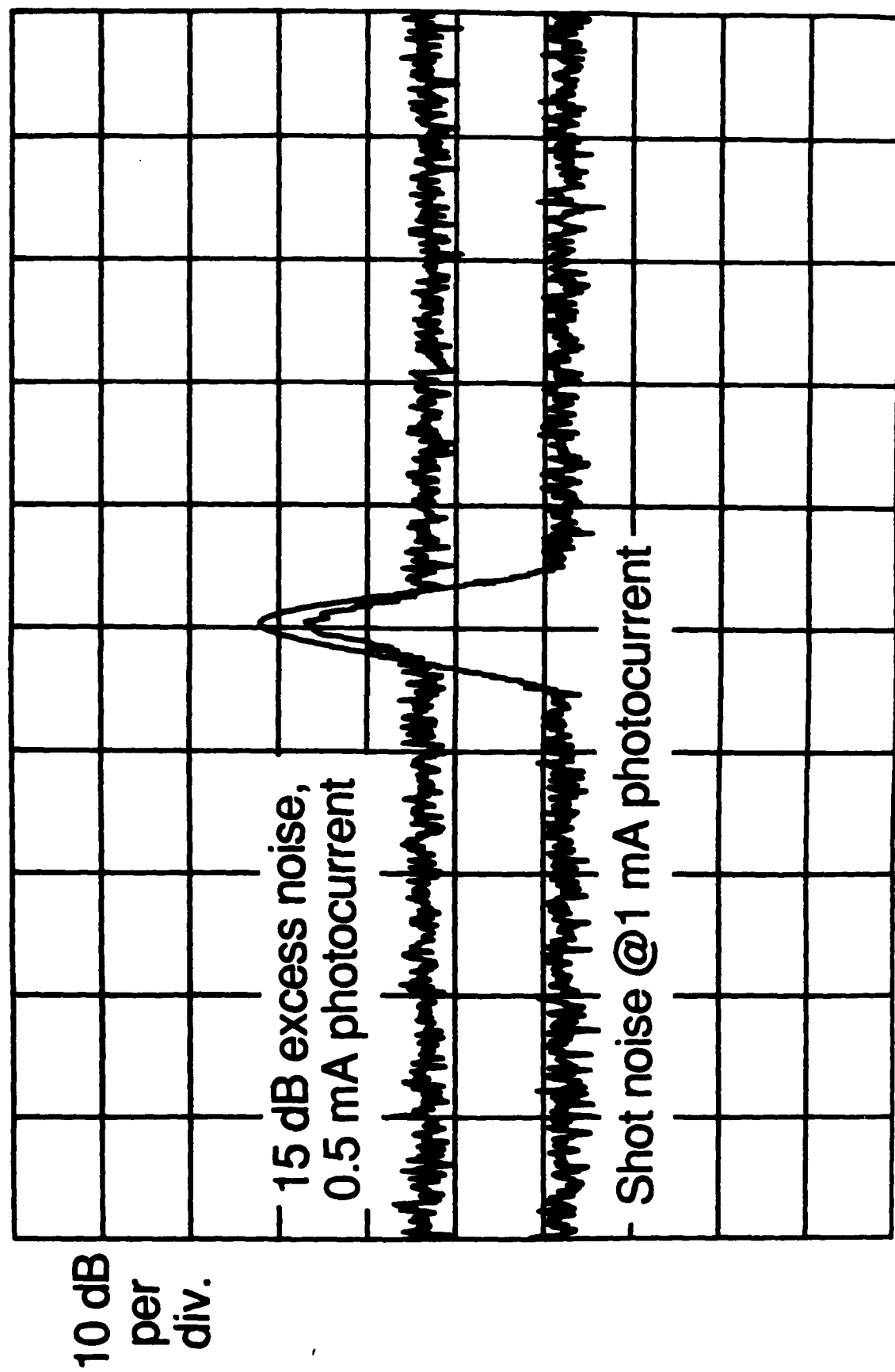
Figure 21: Periodic noise spectrum indicative of a parasitic fiber-Raman laser for the pulse compressor operated near the stimulated Raman threshold.

Center 10 MHz 5 kHz/div Resolution 1 kHz



Center 10 MHz 5 kHz/div Resolution 1 kHz

Figure 22: Excess amplitude noise due to misadjustment of the polarization from the output of the pulse compressor



results in second-order intensity variations due to polarization fluctuations, reducing this excess noise to a level approaching the shot noise limit (Figure 22). However, the pulse compressor with the relatively long 1 km fiber typically contributes 5 to 15 dB of excess amplitude noise. To suppress polarization drift, the non-polarization-preserving fiber is placed in a temperature-stabilized environment.

3.4. Linearity

Because typical circuit voltages are small compared to the half-wave voltage V_{π} , the probe beam intensity modulation is small and very nearly linear with respect to the probed voltage. An analysis of the linearity and dynamic range of the probe due to the sinusoidal dependence of the probe intensity with respect to signal voltage [27] shows the probe is linear to within 1% for signal voltages ≤ 200 volts with the system set at the quarter-wave bias (the linear region of the sinusoidal transmission) as in Eqn. 8.

3.5. Spatial resolution

The minimum achievable spot diameter (full-width half maximum) for diffraction limited optics is

$$d_0 \equiv \frac{\lambda \sqrt{1-NA^2}}{2NA} \quad (32)$$

where λ is the optical wavelength and NA is the numerical aperture of the focusing lens. With a high NA lens spot sizes approaching the optical wavelength are possible. Standard microscope objectives (focal length of 8 mm and NA of 0.4, for example) routinely achieve spot sizes of 3 μm , suitable for probing most IC interconnects but not for probing very small features such as sub-micron gate lines.

While achieving small spots at the front surface, the Gaussian beam is diverging and forming a 50 to 100 μm spot at the back surface. To fully consider the effect of the Gaussian beam on the electrooptic measurement, we must have an analysis that includes the full beam profile and how it interacts with arbitrary circuit fields.

The electromagnetic reciprocity relation, commonly used in microwave transmission problems, provides an expression for the electrooptic signal with general optical and circuit fields [52]:

$$V_{eo} \approx \int_{GaAs} E_{opt} \cdot \Delta\epsilon(E_{ckt}) \cdot E_{opt} dV \quad (33)$$

The change in the dielectric tensor, $\Delta\epsilon$ is set by the electrooptic tensor for GaAs and the circuit fields, E_{ckt} . The optical fields are analytically expressed. The circuit fields acquire more physical meaning when they are expressed in terms of a Fourier sum

$$\phi(x,z) = \sum_{n=0}^{\infty} \Phi(\alpha_n) \cos(\alpha_n x) \exp(-\alpha_n z) \quad (34)$$

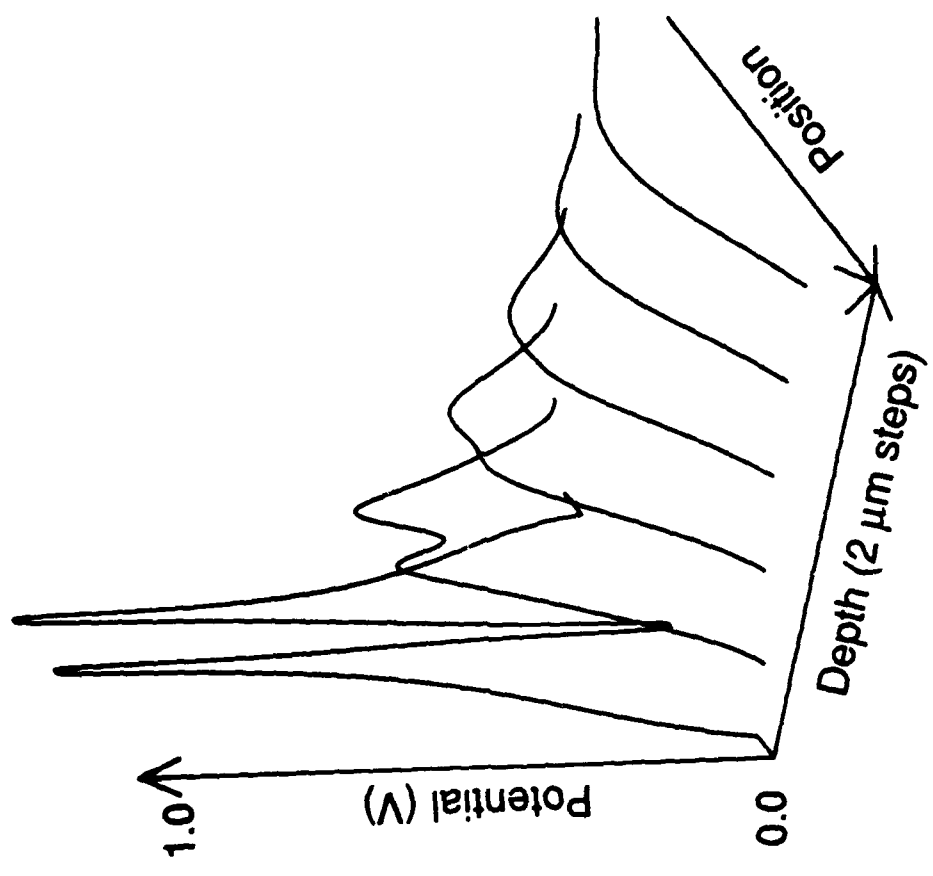


Figure 23: Decay into the substrate of high spatial frequency components of the potential profile. 2 μ m/step; lines are 2 μ m wide, 3 μ m apart.

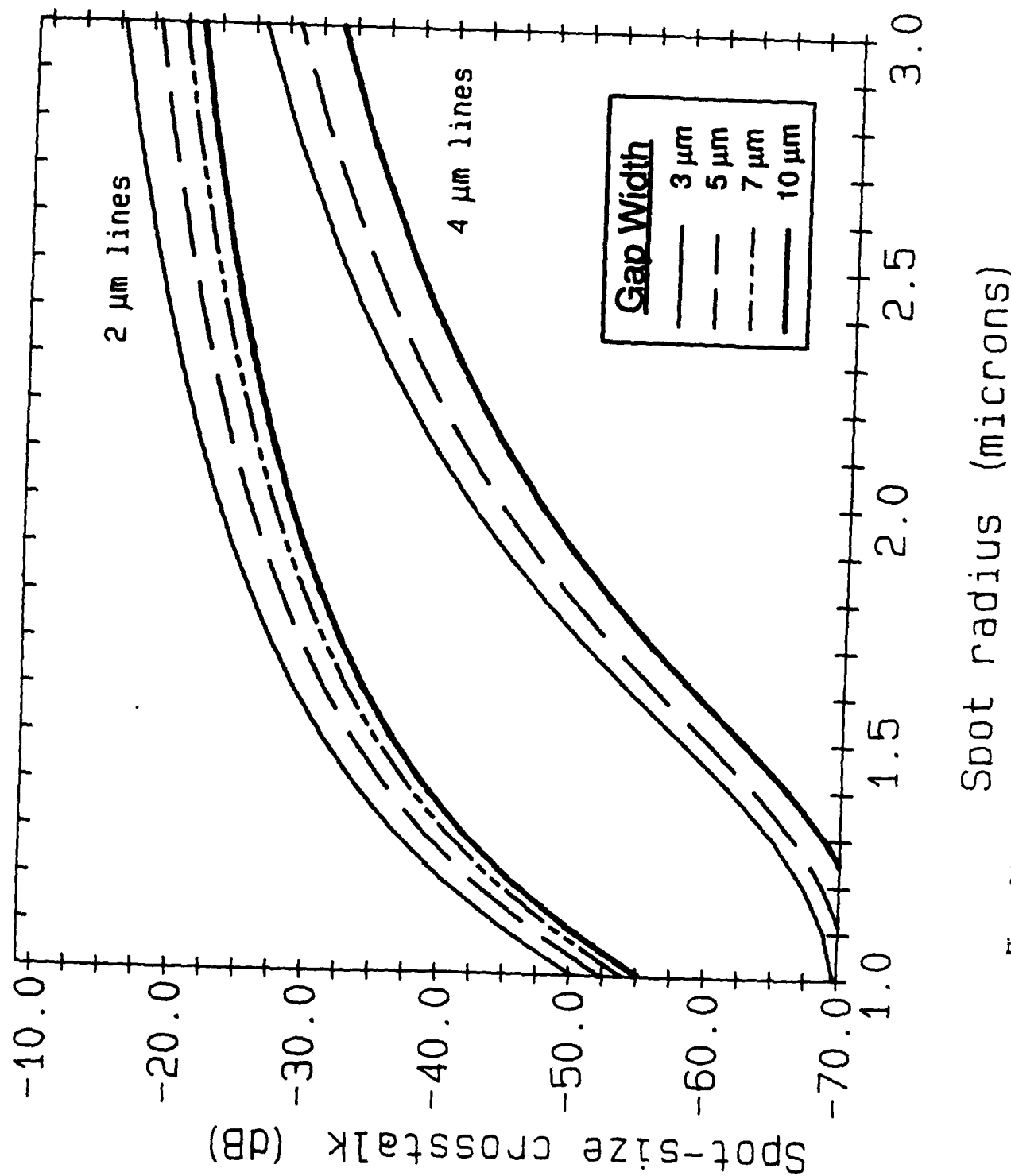


Figure 24: Electrooptic crosstalk errors when the optical spot is comparable to the line width.

Each Fourier term has a periodic spatial variation across the substrate and decays into the substrate with the same factor. Figure 23 illustrates. High spatial frequency components quickly decay in the substrate, leaving only broad components to the potential. The Fourier expression of the fields can be inserted in Equation (33) with the electrooptic tensor and optical fields, and integrated. The electrooptic signal can then be calculated as a function of position by summing over the Fourier components with weights $\Phi(\alpha_n)$, calculated for a general structure with a finite-difference program. From these calculations we draw several conclusions: 1) The wide beam at the backside does not degrade the spatial resolution expected from the Gaussian spot at the front surface; 2) The probe remains insensitive to transverse circuit fields even with the non-zero longitudinal optical fields in the expanding beam. Both results derive from the exponential falloff with depth of high spatial frequency components in the potential and the linear increase of the beam width with depth. The beam width deep in the substrate is then always small compared to the typical transverse variation of the circuit potential, and probes the potential accurately.

To summarize, applying the general theory to the electrooptic problem has confirmed that the spatial resolution is properly described by the frontside Gaussian spot, that the probe is insensitive to transverse circuit fields, and that the probe signal is the potential difference between the front and back substrate planes.

3.6. Accuracy

With the probe modeled as a potential difference probe with spatial resolution of the frontside Gaussian spot, we can examine the accuracy of direct electrooptic probing. Errors are typically of two sorts: electrooptic calibration errors, and electrooptic crosstalk errors. If the magnitude of the component of desired signal returned by the probe depends on the conductor geometry, an electrooptic calibration error exists. If the electrooptic signal also includes signals other than that on the line being probed, electrooptic crosstalk exists. Note that real electrical crosstalk is not an error in the measurement; it is properly part of the signal to be measured.

Electrooptic calibration and crosstalk errors arise through spatial resolution, or spot-size, limits and by non-zero backside potentials. Whenever the optical beam has significant content beyond the conductor under test, the electrooptic signal is in error. The magnitude of the error depends on the spacing to the nearby conductors, the width of the beam, and the width of the conductor. To calculate or measure spot-size electrooptic crosstalk, a narrow grounded line bordered by driven lines on two sides and with a grounded substrate backside is probed. Any electrooptic signal is crosstalk. Figure 24 shows the results of calculations of electrooptic crosstalk to such a thin interconnect. The error is plotted in dB, where -20 dB means that the error signal measured beneath the center line is 10% of the signal applied to the side lines. Note that the error is less than about 3% if the optical spot is less than 1.5 times the line width. Experimental measurements of crosstalk in these structures using a 5 μm spot agrees well with the numerical results.

A non-zero backside potential also can create an electrooptic error. Figure 25 plots calculated frontside and backside potentials for a large, long coplanar waveguide (CPW) transmission line on 20 mil thick semi-insulating GaAs [53]. At the backside, only a broad potential remains, reflecting the decay of the high spatial frequency components of the surface potential. The electrooptic probe

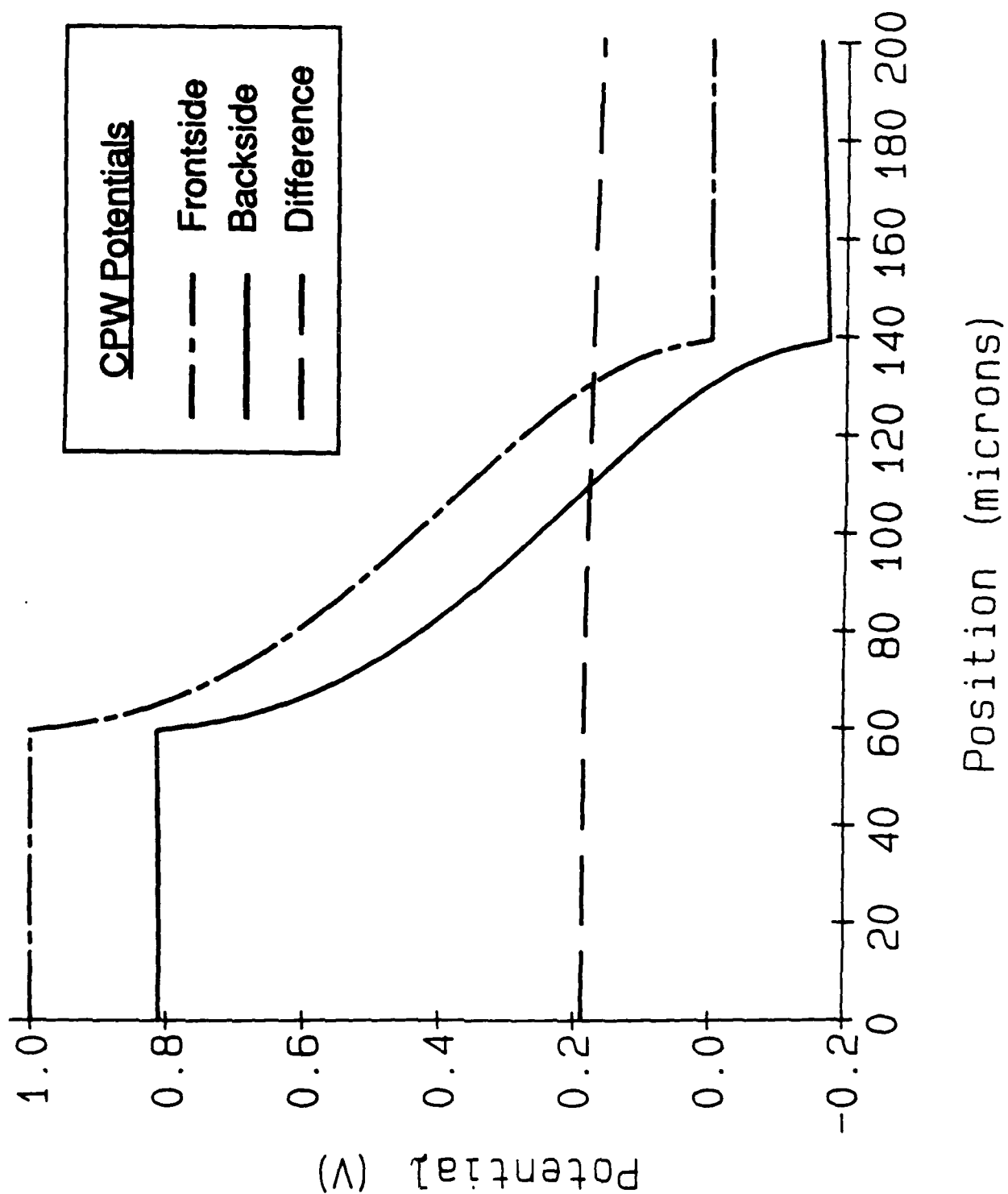


Figure 25: Calculated potentials for a large CPW.

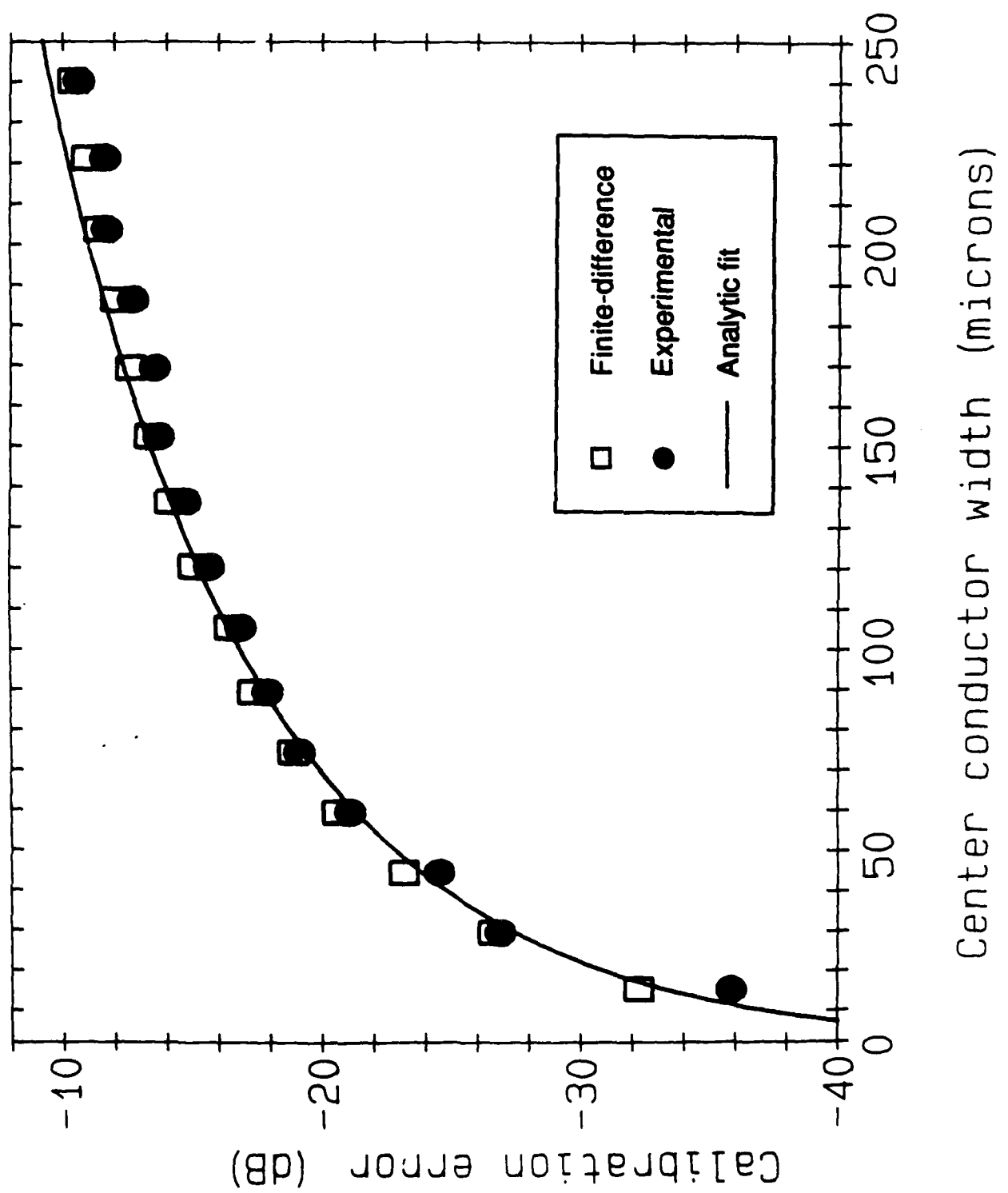


Figure 26: Experimental, numerical, and theoretical results for electrooptic calibrations errors in CPWs.

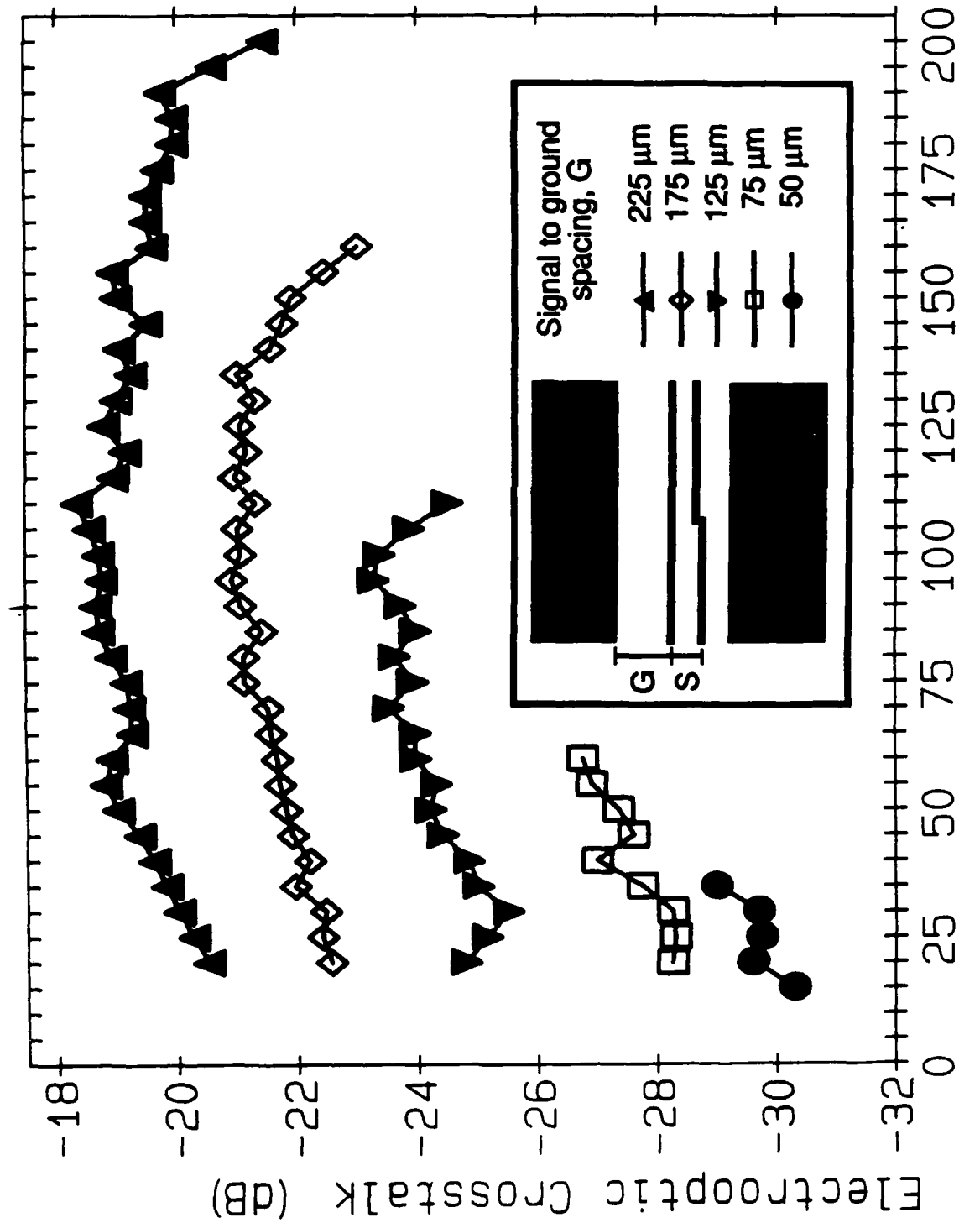


Figure 27: Electrooptic backside crosstalk for two-line digital-like geometries.

takes the difference of the backside and frontside potentials, shown in trace (C). Note that the electrooptic signal beneath the ground is negative---a key characteristic of a backside error. Figure 26 plots the measured and calculated backside errors versus ground spacing for 50Ω CPWs. Errors for the sizes of CPW used in microwave integrated circuits are less than 10%.

More complex are digital circuits. Multiple conductors each contribute to a backside potential that then enters the measurement on each other line. Two structures analyze the electrooptic crosstalk for digital-like geometries. One centers a single $8 \mu\text{m}$ line (wide enough to eliminate spot-size errors from a $5 \mu\text{m}$ beam) between distant ground planes, then adds a second $8 \mu\text{m}$ line between the center and one of the grounds. Both the spacing between the two signal lines and the spacing between the center and the ground were varied. By applying different frequencies to the two lines, and measuring the magnitude at each frequency beneath the two lines, the electrooptic crosstalk is found. The crosstalk here is defined as the magnitude of the center frequency component beneath the side line to the magnitude beneath the center line, corrected for the influence of the backside signal on the measurement beneath the center line. Figure 27 plots these results. The error depends only on the ground-to-ground spacing, not the signal line spacing (the decreased error for the largest and smallest spacings reflects the approaching pads at the end of the structure). Numerical results agree well with these experimental measurements.

A more complex digital circuit can be represented by an array of parallel lines. Chosen were $5 \mu\text{m}$ lines, at $15, 20, 25$, and $30 \mu\text{m}$ pitches on 20 mil thick GaAs. The structures were 8 mm long, and 1.5 mm wide to achieve a backside potential determined only by line spacing. A line near the center is driven and all other lines are grounded; more complex potential patterns clearly can be obtained by superposition. The electrooptic crosstalk is the measured electrooptic signal beneath each ground line as a function of line number, with 1 being adjacent to the driven line. Figure 28 plots the results. For lines 3 to 9, the electrooptic crosstalk---the backside potential---is nearly constant because only a broad potential remains at the substrate backside. Nearer lines suffer real electrical crosstalk that partially cancels the constant negative electrooptic crosstalk, reducing the apparent crosstalk. Again, numerical analysis gives results agreeing within 1-2 dB with experiment.

We conclude that ground-to-ground spacing, or, equivalently, line pitch, is the strongest determinant of backside electrooptic crosstalk. Circuits with many overlaid orthogonal interconnects will further ground backside signals. At any given conductor, though, the backside signal will be a sum of all the signal lines nearby; the total error then depends on the vector sum of the contributing signals.

To reduce electrooptic errors, a transparent backside conducting layer can be applied either to the wafer or to the wafer holder. Even if not grounded, such a layer forces an equipotential at the backside, reducing the local backside signal. Experimentally, depositing the transparent conductor Indium-Tin-Oxide on the wafer backside reduced electrooptic crosstalk to below 3% for all reasonably sized test structures. The finite resistivity of the layer and its affect on frontside transmission line impedances will reduce its effectiveness at microwave frequencies. Measuring the electrooptic signal beneath a known ground and subtracting it from the electrooptic measurement beneath the desired node may be the most effective and practical method of eliminating backside errors.

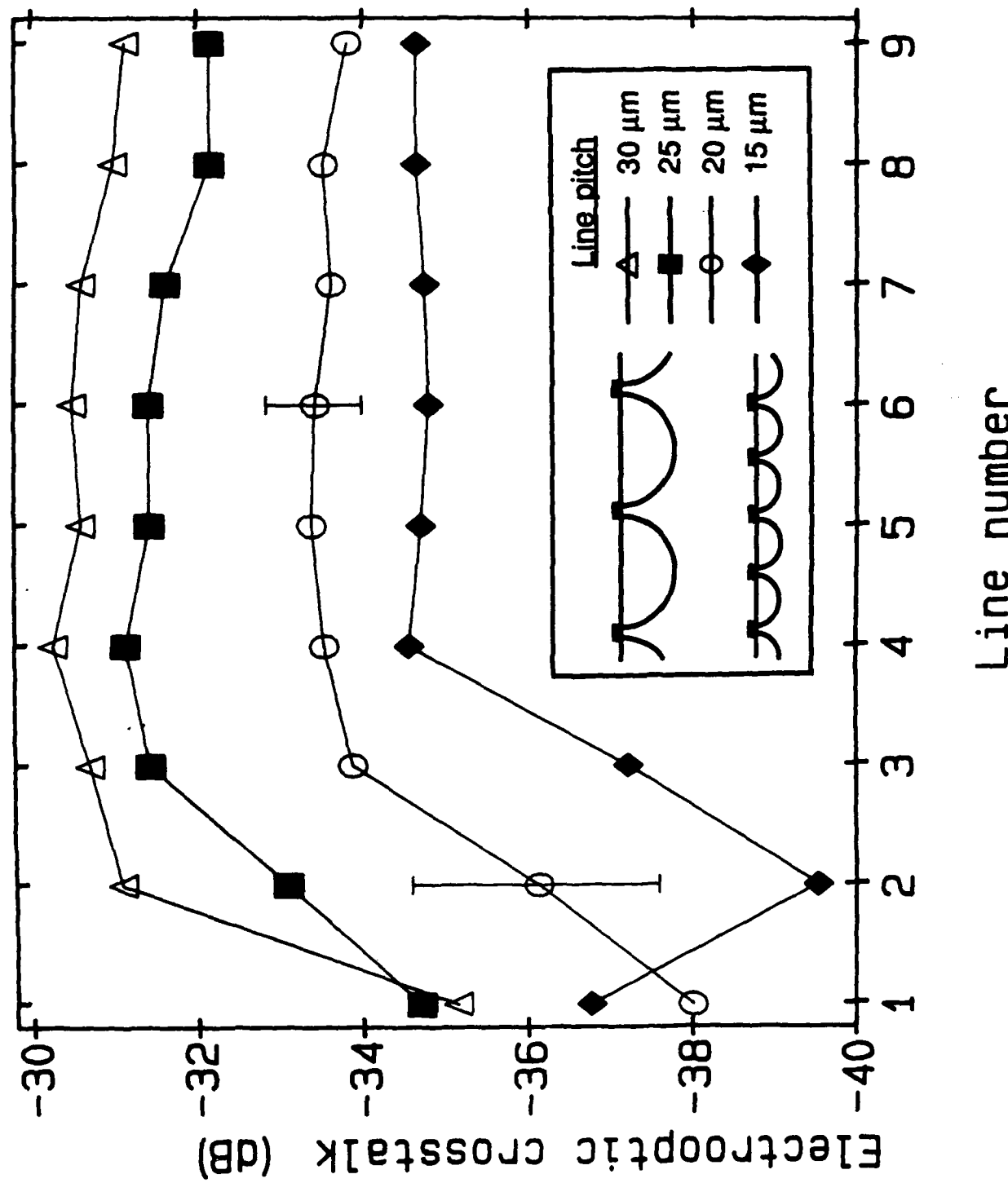


Figure 28: Electrooptic backside crosstalk for many-line structures.

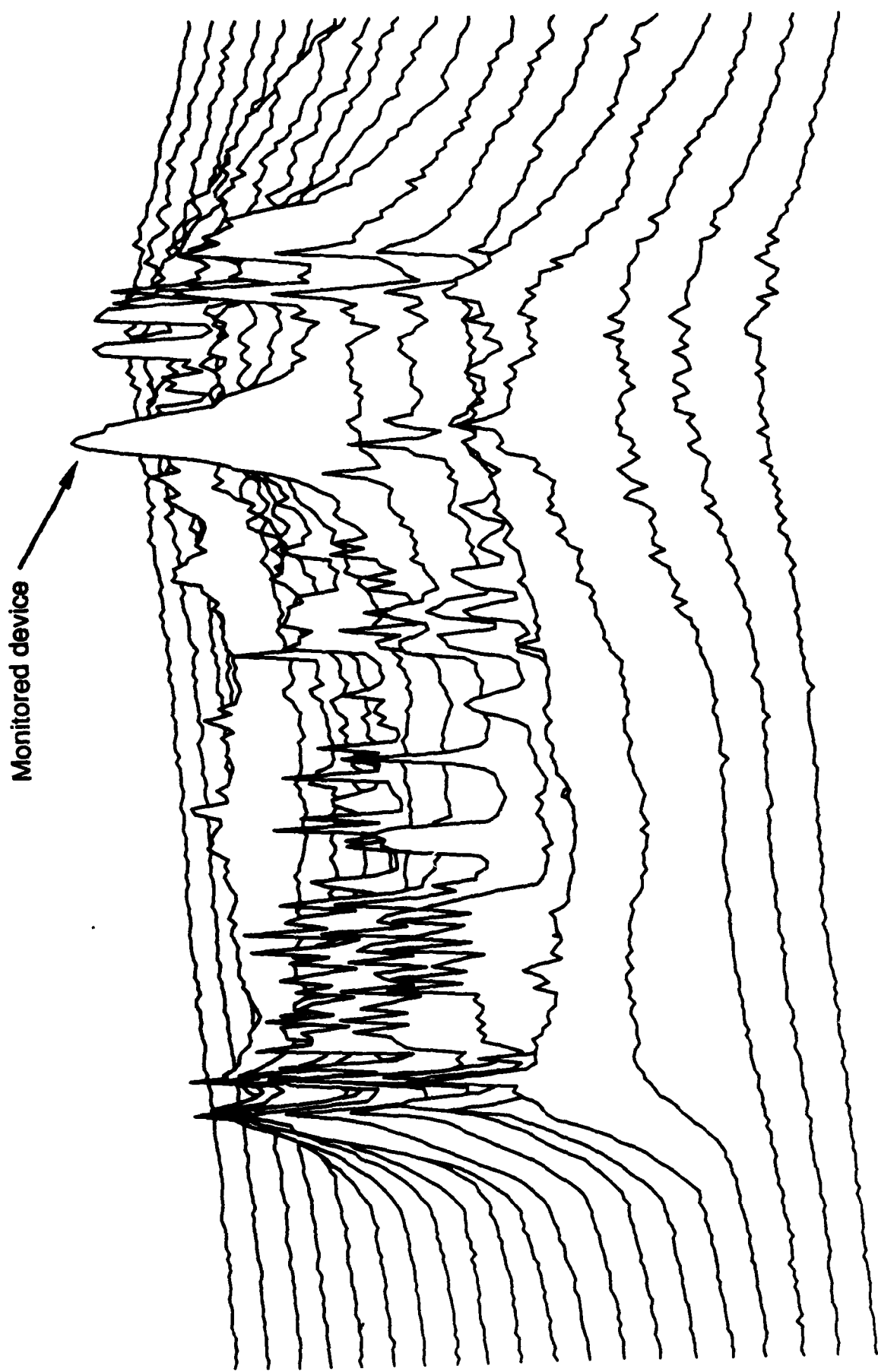


Figure 29: Optically-induced increase in drain current as beam scans around large test chip.

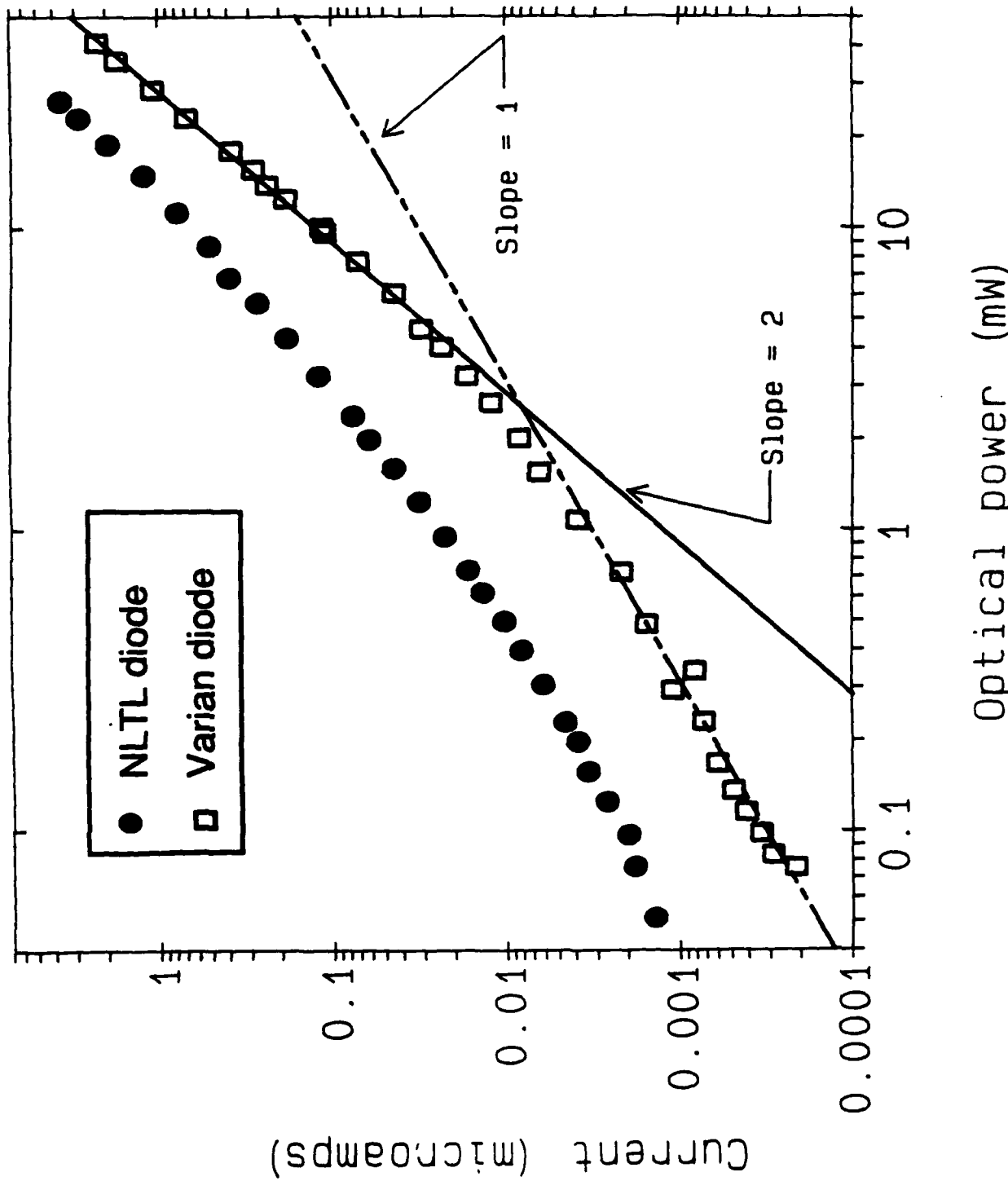


Figure 30: Dominance of two-photon absorption above several mW of average optical power.
NLTTL= Nonlinear transmission line test diode; Varian=Varian diode from microwave MESFET test chip.

3.7. Invasiveness

One important feature of optical probing of IC's is the non-contact, non-destructive nature of the technique. Compared to conventional electrical probes, the optical probe makes no mechanical contact to the IC, avoiding physical damage to the circuit, does not require the test point to drive a $50\ \Omega$ load impedance, and has no parasitic impedances. The lack of parasitic impedances is an important characteristic for measurement frequencies in the upper microwave and millimeter-wave region, where even the small parasitic impedances of well-designed electrical probes become significant.

Most circuits are not perturbed by direct electrooptic sampling: the gain of a microwave distributed amplifier, for example, changes by only .1 dB when probed by an intense 125 mW 1.06 μm beam. A MUX/DEMUX from TriQuint Semiconductor, however, was strongly perturbed by such a beam. To avoid or minimize this invasiveness, we must understand the mechanisms causing it.

Since the beam probes only interconnects, devices cannot be directly illuminated by the subbandgap light. After the beam reflects from the front surface, though, it is 30% reflected at the backside and forms a second, broad spot at the frontside. Light from both this large spot and the smaller probe spot can scatter from surface roughness associated with active devices, such as the ohmic contacts and gate etches. Any light scattered at an angle greater than 16° from the surface normal is totally internally reflected at the GaAs-air interfaces and waveguides in the substrate. Devices millimeters away from the probe point can be perturbed. Experimentally, this process appears as an increase in the drain current whenever the probe is in a region dense with active devices (see Figure 29). The result of the scattering and the second, large spot is a weak flood-like illumination of the substrate.

The beam must then be absorbed. Deep-level (DL) and two-photon absorption (TPA) are the dominant processes for creating charge from the subbandgap light. The first has a quadratic dependence on intensity; the second, linear. Figure 30 plots the short-circuit current of two Schottky diodes versus optical power. Because this current is proportional to the generated charge density, the slope 2 on the log-log scale reveals that TPA dominates DL absorption above several milliwatts of optical power. Estimates of the generated current and of the crossover from DL to TPA agree well with experiment. TPA generates charge at the focus of the beam; everywhere else, though, deep-levels absorb the light and create free carriers.

The perturbation to a Schottky diode is that of a solar cell; the dark I-V curve is shifted down in current by the illuminated short-circuit current I_{sc} . Tens of microamps at most, I_{sc} is generally negligible, but the open-circuit voltage V_{oc} can be some tenths of a volt. These two manifestations of the same light-induced perturbation are a useful division: the short-circuit current depends linearly on the charge, requires a small load to be seen, and, because of the small load, is typically fast; the open-circuit voltage depends logarithmically on the charge, requires a large load, and then is slow. Only for large loads on a line will the appreciable V_{oc} be manifested.

The division of perturbations for the diode may equally well be applied to the MESFET. Perturbations may be fast and linear with charge or slow and logarithmic with charge. Figure 31 shows a typical change to the DC IV curves of a microwave MESFET with a gate about 2 by 200 μm when the beam directly illuminates a portion of the gate region. All the curves shift up in current as

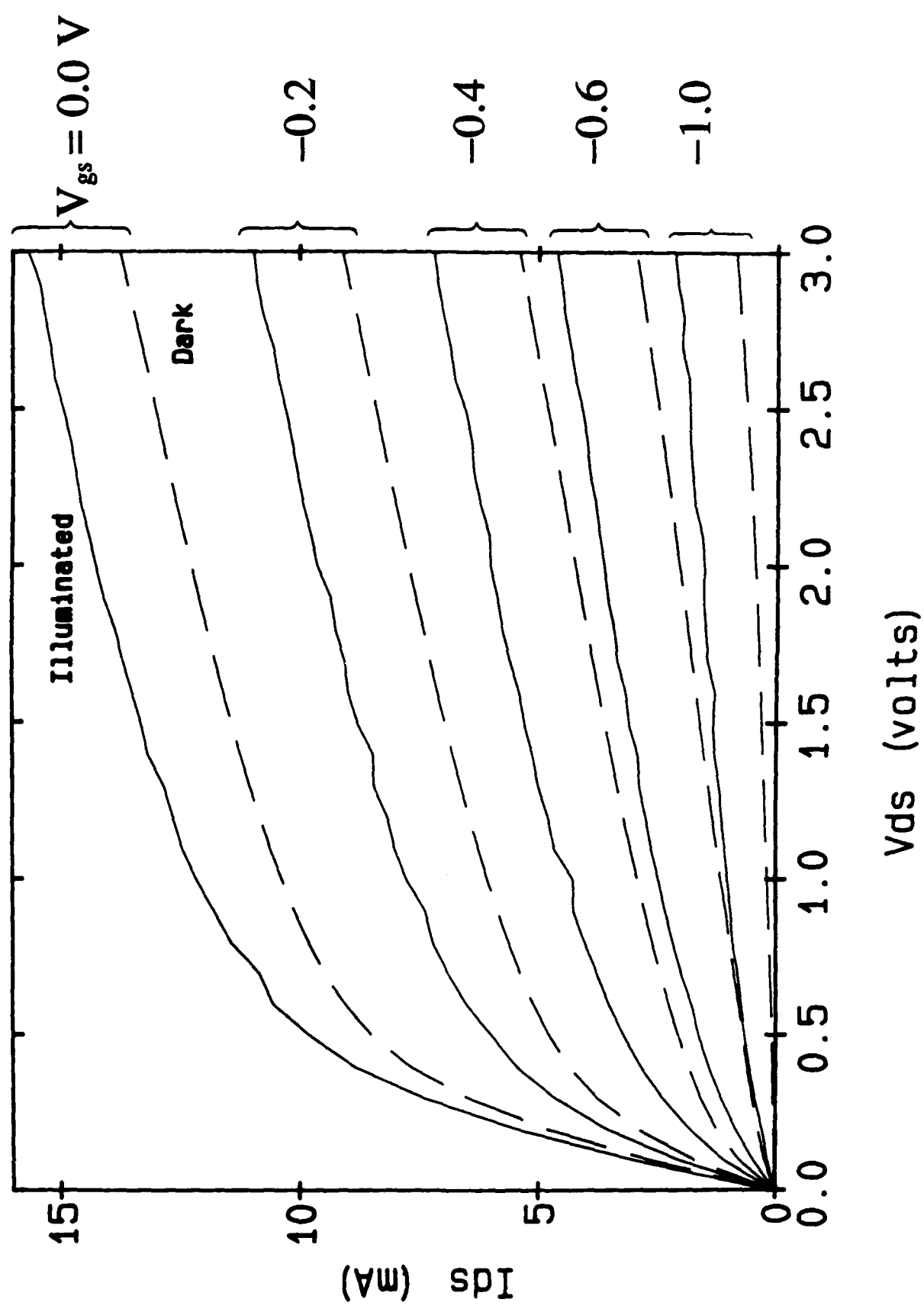


Figure 31: Optically-induced shift in DC I-V curves for a large microwave MESFET.

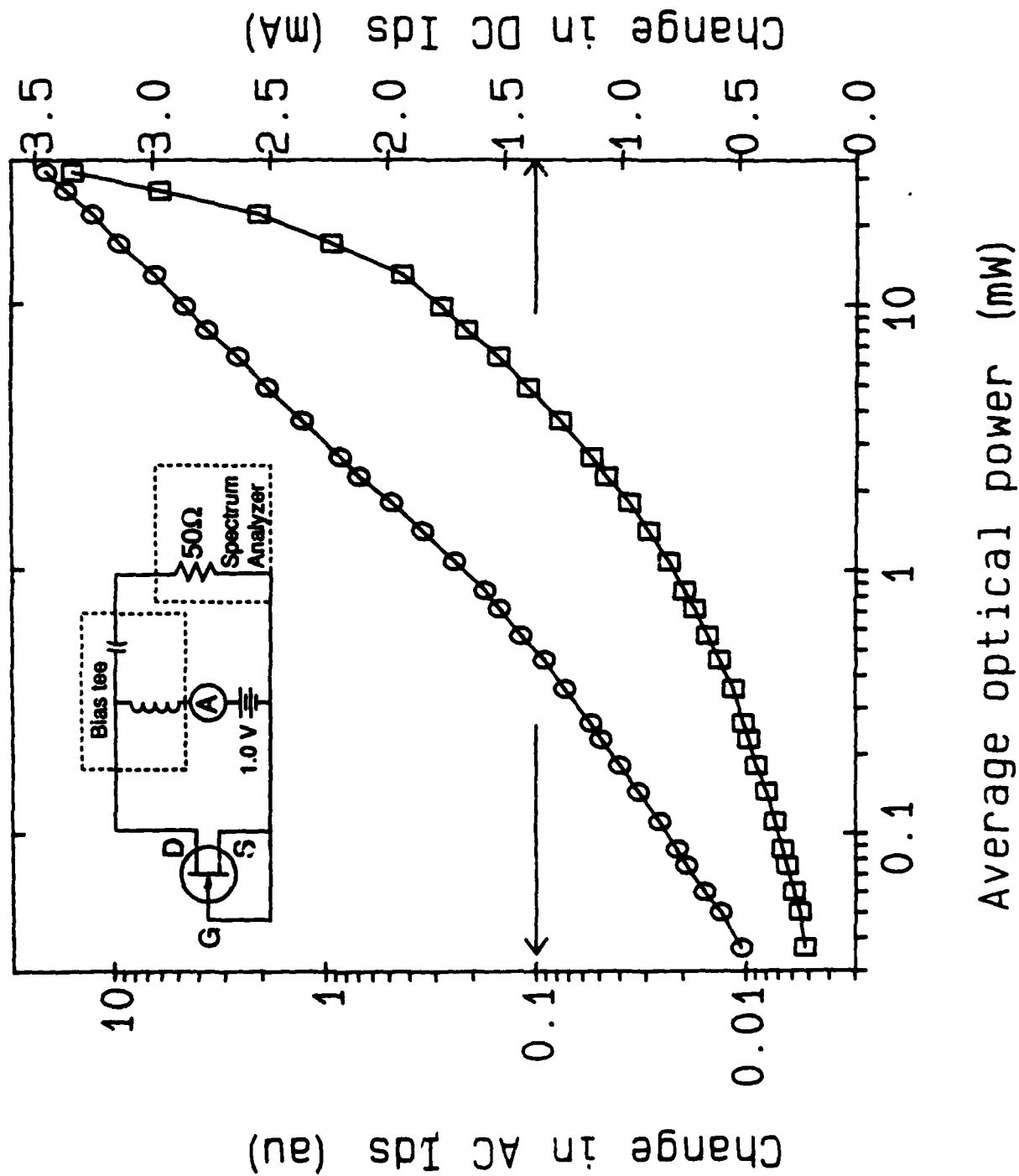


Figure 32: Optical power dependencies of MESFET current perturbations. Note the different scales for the DC and AC components.

100 ps/div

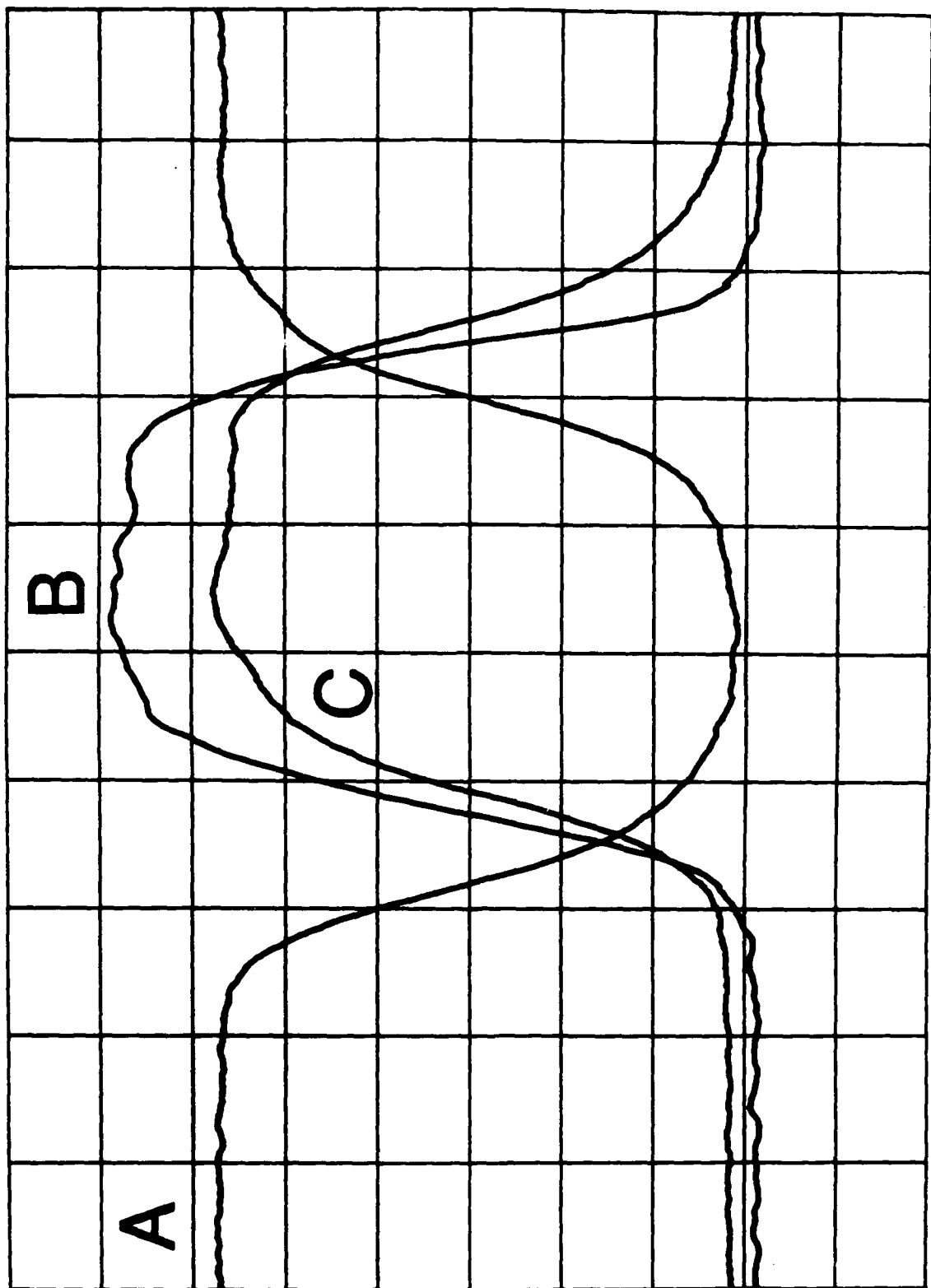


Figure 33: Voltage waveforms at the input (a), source-follower gate (b), and output (c) of GaAs buffered-FET-logic inverter gate [46].

if the gate voltage was increased. More detailed inspection of I_{ds} vs. V_{gs} for this and smaller MESFETs shows that at these large optical powers, the MESFET cannot be pinched off. A photocurrent mechanism, such as an I_{sc} at a device terminal, or a photoconductive process in the channel must be present. Given the large optical power in the FET (about 40 mW), such a process, linear in charge, is expected.

Figure 32 monitors the same MESFET, but breaks the drain current into DC and AC components with a bias tee. The left axis plots the magnitude of a single spectral line of the AC output on a log-log scale versus the optical power. The curve is nearly linear (TPA probably contributes for large optical powers), consistent with a photocurrent process. The right axis plots the change in the DC photocurrent on a semi-log scale versus the optical power. The curve is not linear but more nearly logarithmic in power. At the highest powers, the curve jumps up sharply when the non-zero DC average of the AC component exceeds the DC component. Above a few milliwatts, TPA also draws the curve upwards. This logarithmic dependence on optical power of the slow current perturbation is consistent with a photovoltage. While the linear AC portion will quickly decay with power, the logarithmic DC portion remains, even 3 decades down in optical power. The most likely site for this DC photovoltage is the large depletion region at the interface of the channel and the high-resistivity substrate.

The path of the MESFET perturbation is then as follows: Light scatters from surface roughness, waveguides through the substrate, generates free carriers by deep-level absorption, creates a DC photovoltage at the channel-substrate junction because of the large substrate resistivity, and backgates the MESFET. The logarithmic dependence on intensity provides little incentive to reduce optical power; a better choice is to avoid surface roughness and, if possible, use a longer wavelength, where deep-level absorption decreases [54,55]. The correlation of scattering with device density suggests that direct electrooptic sampling may be best suited to ultrafast small-scale integration circuits.

4. Circuit measurements

4.1. Realistic circuit testing conditions

Optical probing, providing access to the high-impedance internal nodes of IC's with picosecond time resolution and micron spatial resolution, permits direct measurements of the performance of state-of-the-art microwave and digital GaAs circuits. To permit meaningful evaluations of a circuit's performance and to provide meaningful comparisons between competing circuit technologies, these measurements must be made under realistic circuit operating conditions. The propagation delay of switching devices in simple test circuits, measured by either electrooptic sampling or by conventional methods, are used to project the maximum clock frequency of these devices used in digital systems. Unless the test circuit provides representative switching voltages, interface impedances, and fan-outs, the measured delays will not correlate well with the maximum clock frequency of circuits such as shift registers, binary multipliers, and memory. For example, the response of a transistor driven by a low-impedance photoconductor and loaded by a low-impedance, $50\ \Omega$ transmission line is in general much faster than the response of a logic gate driven by the normal output impedance of a driving gate and loaded by the normal input capacitances of cascaded gates. If the test circuit is con-

structed in hybrid form with wire bonds between the tested device and the transmission lines, the interconnect parasitics may dominate the circuit response.

Ring oscillators and inverter strings, the simplest digital test structures, are often used as benchmarks of circuit speed. These circuits load the gates with unity fan-out and tend to give optimistically small delay measurements. Ring oscillators often operate small-signal, without full logic-level swings, while inverter strings operate with full logic-level swings. Master-slave flip-flops, connected as binary frequency dividers, operate with logic signal levels and with each gate loaded by a fan-out of two, and serve as better performance indicators.

For microwave/analog circuits such as distributed amplifiers, appropriate test signals are swept-frequency sinusoids for small-signal transfer function measurements, or single-frequency signals set to larger amplitudes for large-signal and saturation measurements. Signal sources and terminations should have $50\ \Omega$ impedances to eliminate source and load reflections.

4.2. Digital circuit measurements

Ring oscillators provide a measure of a gate delay from the rate of a free-running signal propagating around an odd-numbered ring of inverters, i.e. the repetition period corresponds to product of the average gate delay and the number of gates. These free-running circuits are not readily clocked with an external signal, making synchronization to the probe pulses for electrooptic sampling difficult. Inverter chains, however, consisting of series of cascaded inverting logic gates, must be clocked with an external signal, permitting the synchronization of probe pulses for electrooptic measurements and assuring full logic-level switching of the gates. Typically, average gate delays are measured with sampling oscilloscopes; the propagation delay of the entire chain is measured and divided by the number of inverters to obtain the average delay of an individual inverter. For electrooptic testing the input inverter is switched with a microwave synthesizer, generating a square wave that ripples through the test structure. The first several inverters condition the input signal, sharpening the switching transients until the signal risetimes and falltimes reach a steady-state value. The optical probe is then positioned from node-to-node, measuring directly the propagation delays and signal risetimes at gate input and output nodes and at nodes internal to the gate.

Figure 33 shows a gate delay measurement on an inverter chain implemented in $1\mu\text{m}$ gate-length buffered-FET logic MESFETS, with Figure 34 showing an SEM picture of one inverter. The delay between curves A and B of Figure 33 is the propagation delay of the inverting common-source stage, 60 ps, while the delay between curves B and C is the delay of the source-follower buffer and diode level-shifter, 15 ps. The inverter chain from Lawrence Livermore National Labs [56] consisted of 20 gates each with a fan-in and fan-out of unity.

The timing of inverter chains has also been examined by Zhang, *et. al.* [57], optically triggering an inverter in the chain and using electrooptic sampling to measure the circuit response and gate propagation delays in a pump/probe configuration. A frequency-doubled portion of the probe beam (at $\lambda=532\ \text{nm}$) focused on the gate region of a FET photoconductively generates carriers, turning on the FET and generating a switching transient that propagates down the test structure. The probe beam, positioned at a node after the switched gate, is successively delayed with respect to the switching

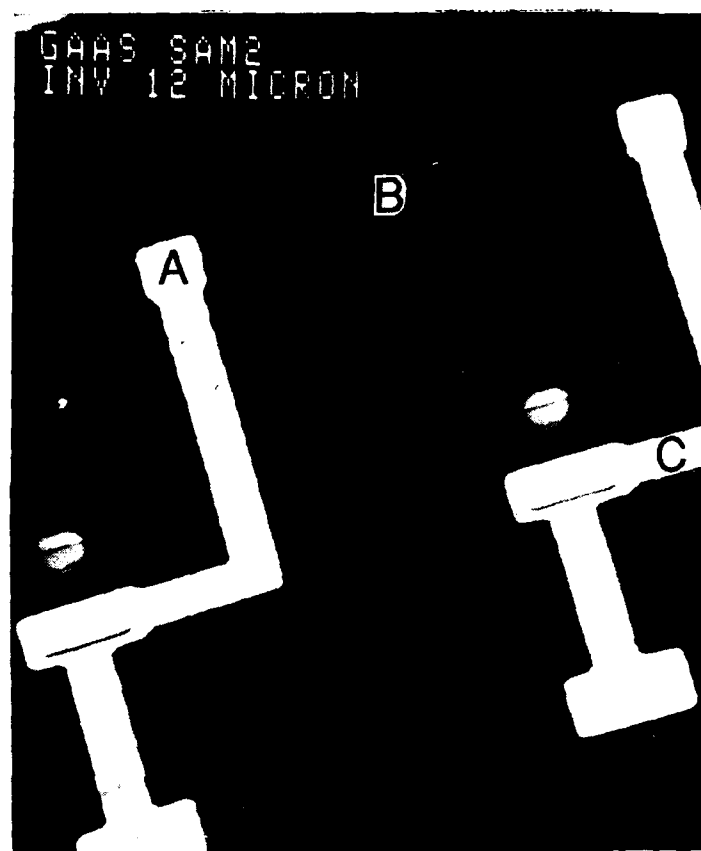


Figure 34: A single inverter within the buffered-FET-logic inverter chain [54]. Photo courtesy of S. Swierkowski, Lawrence Livermore National Labs.

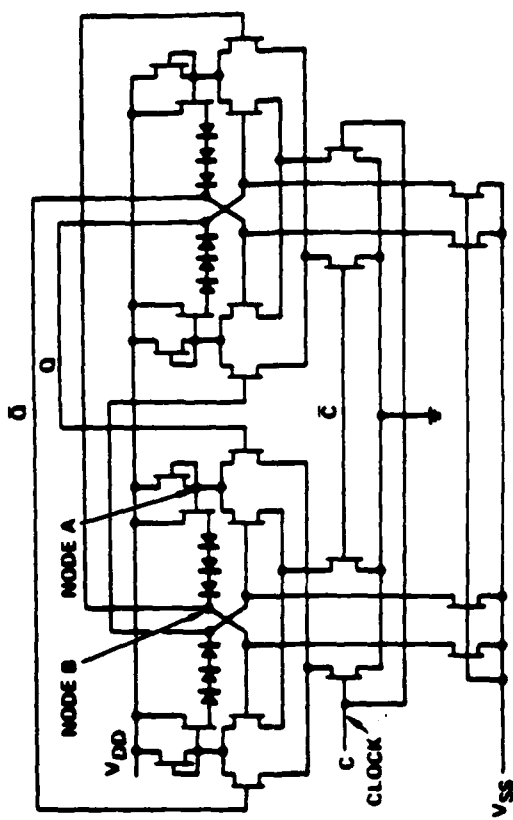


Figure 35: Schematic diagram of a static frequency divider using buffer-PET logic. The labeled points refer to the electrooptically measured data in Fig. 27

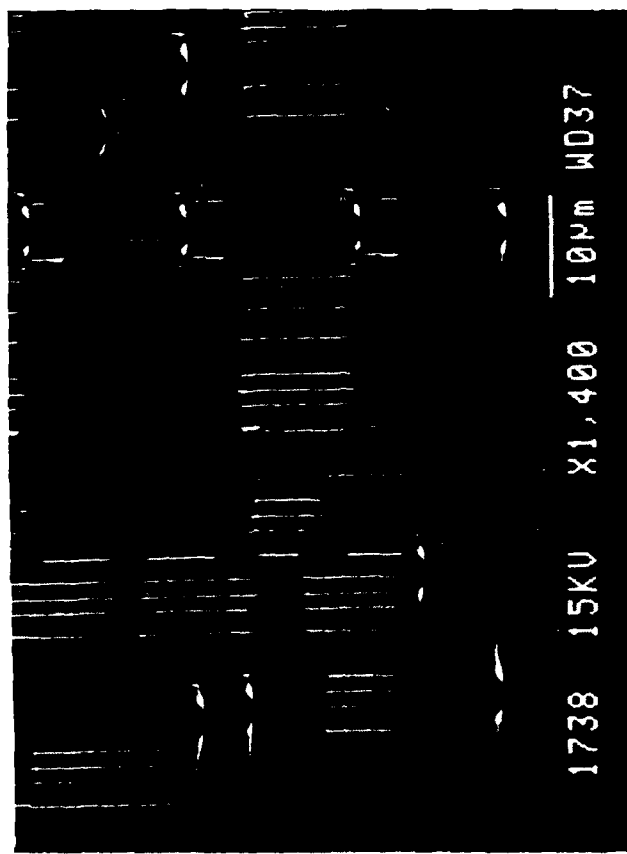


Figure 36: Scanning-electron microscope picture of a section of an 18 GHz static frequency divider [4], courtesy of J.F. Jensen, Hughes Research Laboratories. The circuit used 0.2 μm e-beam written gates, molecular-beam epitaxy-grown channels, air-bridge lines to reduce interconnect capacitance, and optimized feedback to achieve high frequency clock rates.

pulse to map the transient waveform. This technique offers an all-optical approach, avoiding microwave connection to the IC, which is suitable for testing of simple IC test structures. However, optical triggering is an impractical method for generating the multiple clock and data signals required to drive large scale IC's.

A higher-level test circuit for IC performance is the static frequency divider, consisting of two flip-flops in a master-slave divide-by-two arrangement [4]. The maximum clock frequency of the divider, set by the propagation delays through the master-slave feedback path, provide an indirect measure of the devices' speed. Testing this circuit is normally accomplished by increasing the clock rate of the divider until its divide-by-two output fails.

The schematic of such a frequency divider is shown in Figure 35. The circuit, from Hughes Research Laboratories (see Figure 36), uses 0.2 μm e-beam written gates, molecular-beam epitaxy grown channels, air-bridge interconnects, and optimized feedback to achieve high frequency clock rates. The dividers were implemented in two circuit families, buffered-FET logic (BFL) and capacitively enhanced logic (CEL). Conventional testing, using transmission line probes to drive the circuit and monitor its output on a spectrum analyzer indicated correct circuit operation to 18 GHz. However, the spectrum analyzer gives inconclusive evidence of correct divider operation, since it measures only the output frequency and not the time waveforms. By direct waveform measurements using electrooptic sampling, correct divide-by-two operation was verified, gate propagation delays of 20-30 ps were measured and correlated to maximum clock frequencies (Figure 37), and the internal delays through the inverting and source-follower stages of individual BFL gates were identified [58]. Note that while the scaled 0.2 μm gate-length FET's had significantly shorter delay through the inverting stage, the delay through the buffer stage was comparable to the 1 μm BFL from LLNL. These data suggest the speed limitation through the buffer stage is no longer *transistor* limited but limited by the resistance-capacitance time constant of the level-shifting diode resistance and the input capacitance of the cascaded gates.

The spatial resolution of the electrooptic sampler permits probing of MSI GaAs digital IC's to determine signal risetimes and relative timing. Figure 38 shows serial output waveform probed on a 2 μm conductor internal to the output buffer in a 2.7 GHz 8-bit multiplexer/demultiplexer from Tri-Quint Semiconductor [59] and Figure 39 shows the 8-phase clock waveforms probed on 3 μm metal interconnects spaced by 6 μm . Similar measurements have recently been made on gigahertz logic flip-flops and counters [60].

4.3. Microwave circuit measurements

At microwave and millimeter-wave frequencies, where conductor lengths and circuit element sizes often become large with respect to the electrical wavelength, direct measurements of conductor voltages and currents are difficult, particularly with conventional electrical test instrumentation. Directional couplers and directional bridges separate the forward and reverse waves on a transmission line; standard microwave test instruments use these to measure the incident and reflected waves at the ports of a microwave device or network. The relationship between these waves is expressed as the wave scattering matrix S known as the *scattering parameters* [61]. The electrooptic sampler directly

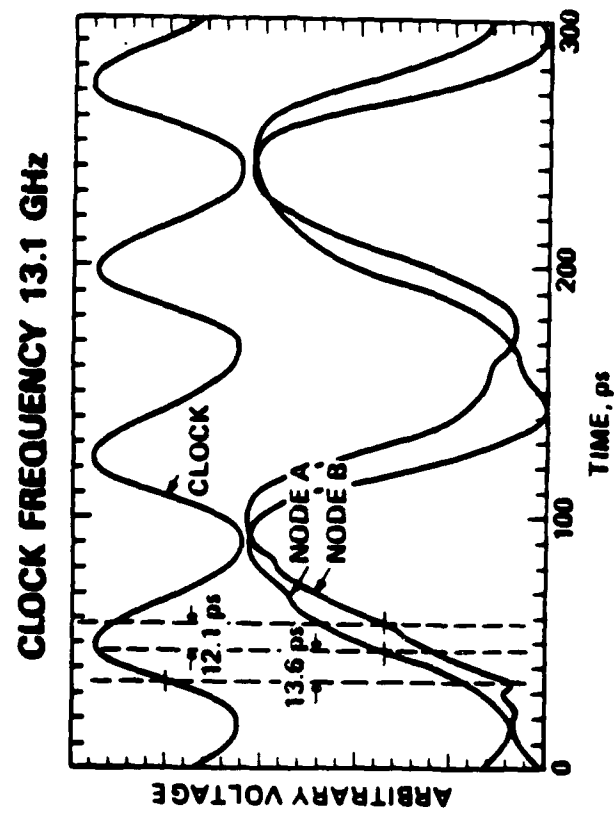
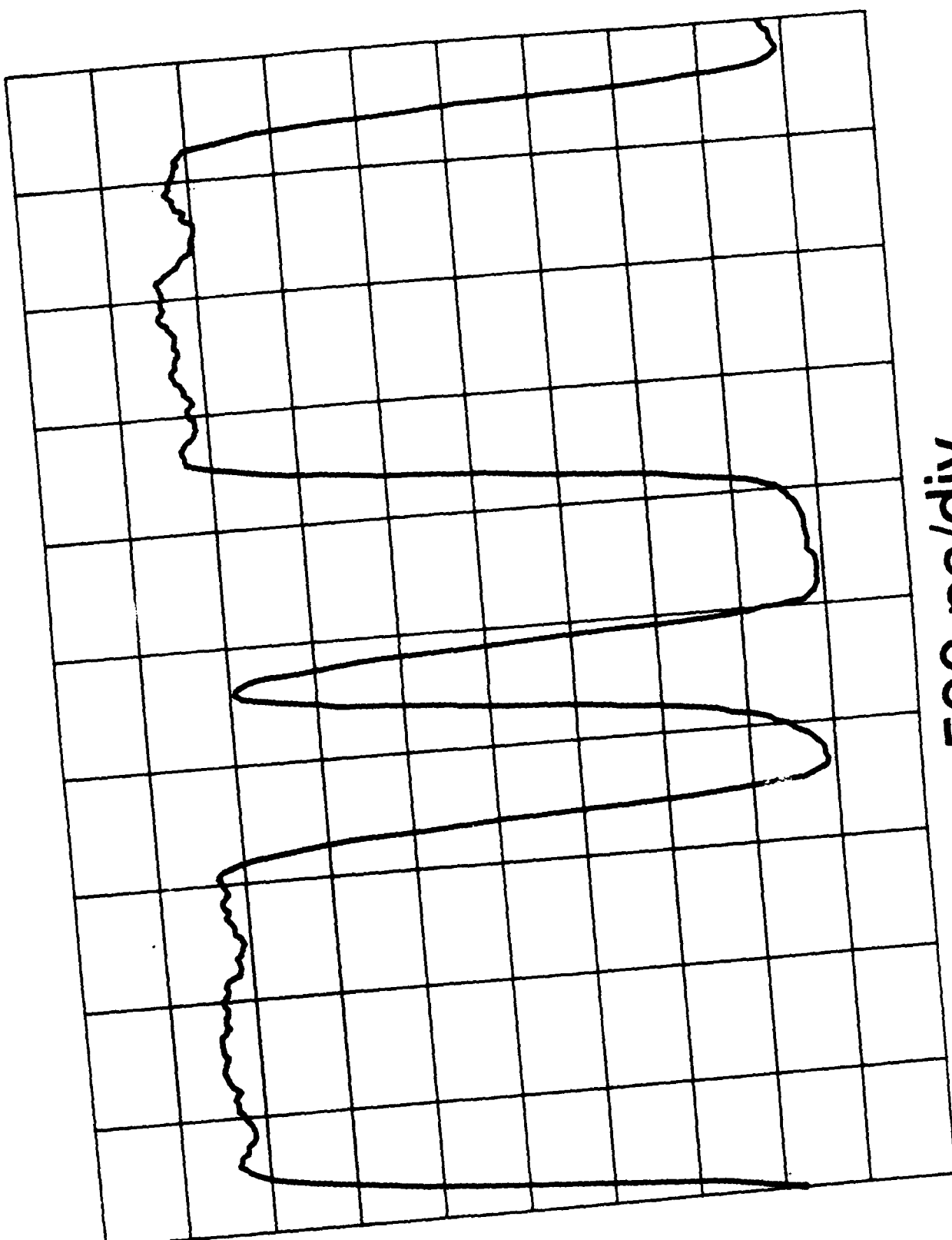


Figure 37: Clock signal and divide-by-two waveforms measured with direct electrooptic sampling. The test points are indicated in Fig. 25.

500 ps/div

Figure 38: Serial output waveform of a 2.7 GHz, 8-bit multiplexer/demultiplexer[57] measured by electrooptic sampling. The output word is 11110100.



300 ps/div

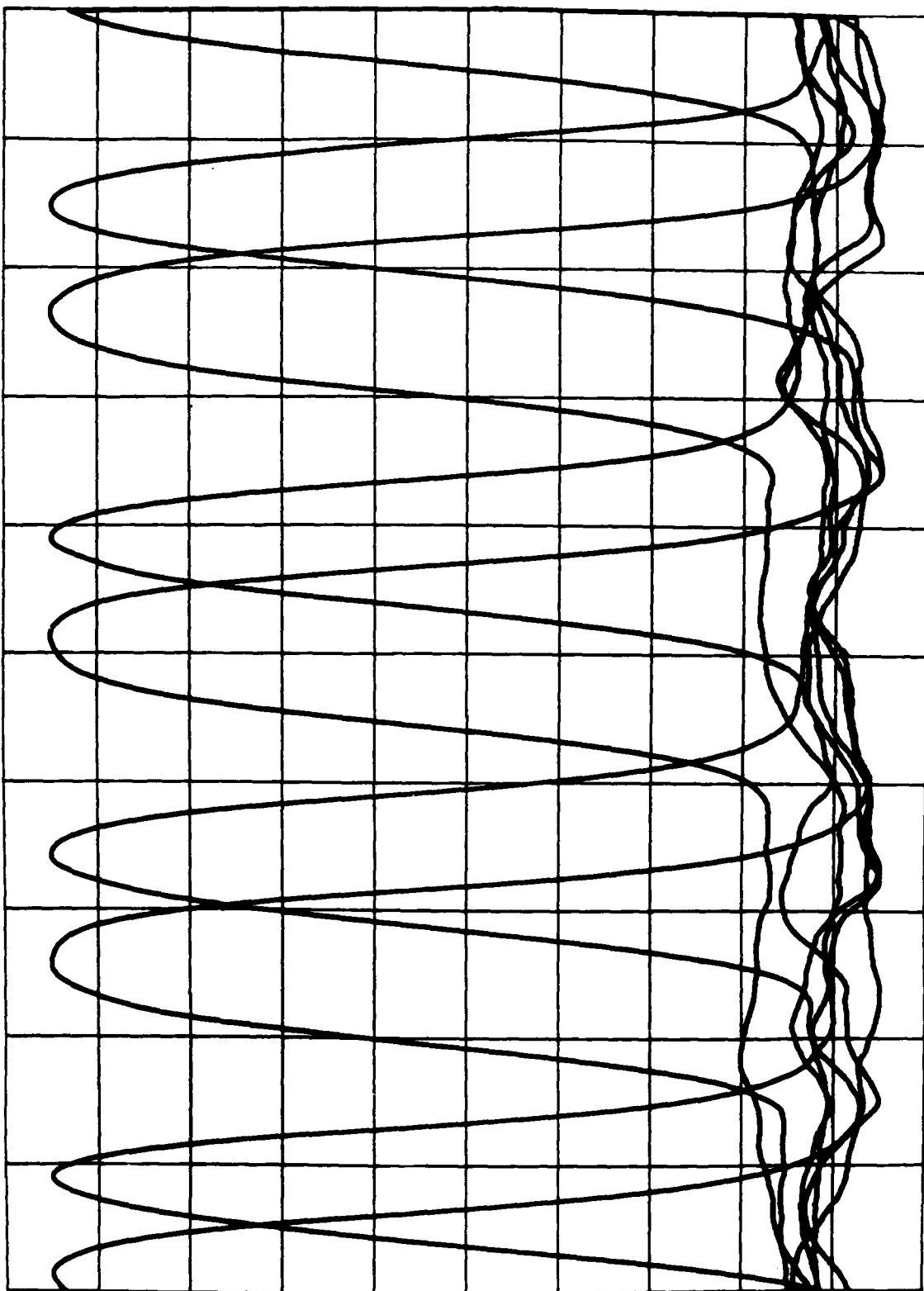


Figure 39: 8-phase clock waveforms in 2.7 GHz multiplexer. An asymmetrical 2.7 GHz clock input results in timing skew in the 8-phase counter.

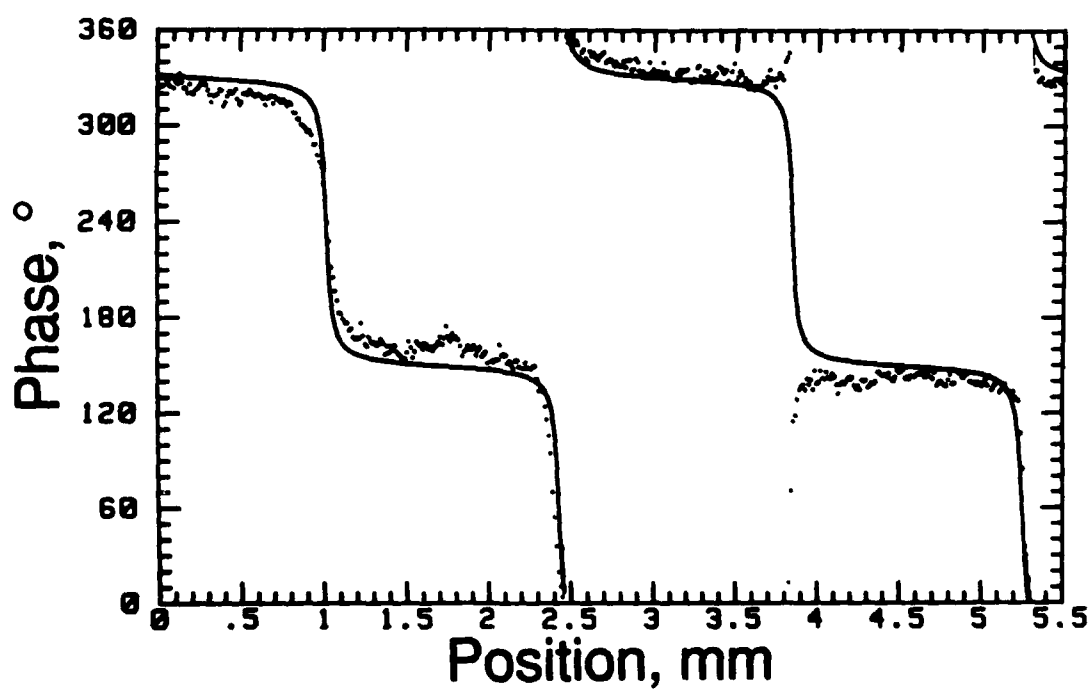
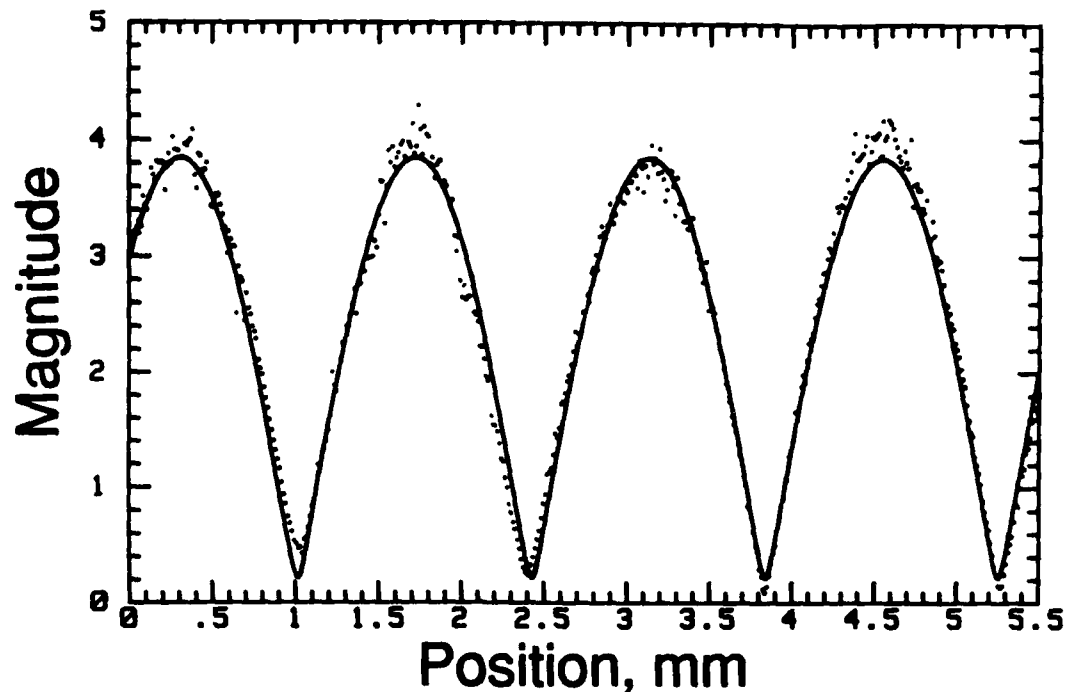


Figure 40: Magnitude (a) and phase (b) of a 40 GHz voltage standing wave on an open-terminated GaAs coplanar waveguide transmission line. The points are the data and the solid line is the fitted curve. From this measurement a reflection coefficient of 0.90 @ -80° is calculated. Each division of 10° in phase corresponds to 0.7 ps in time.

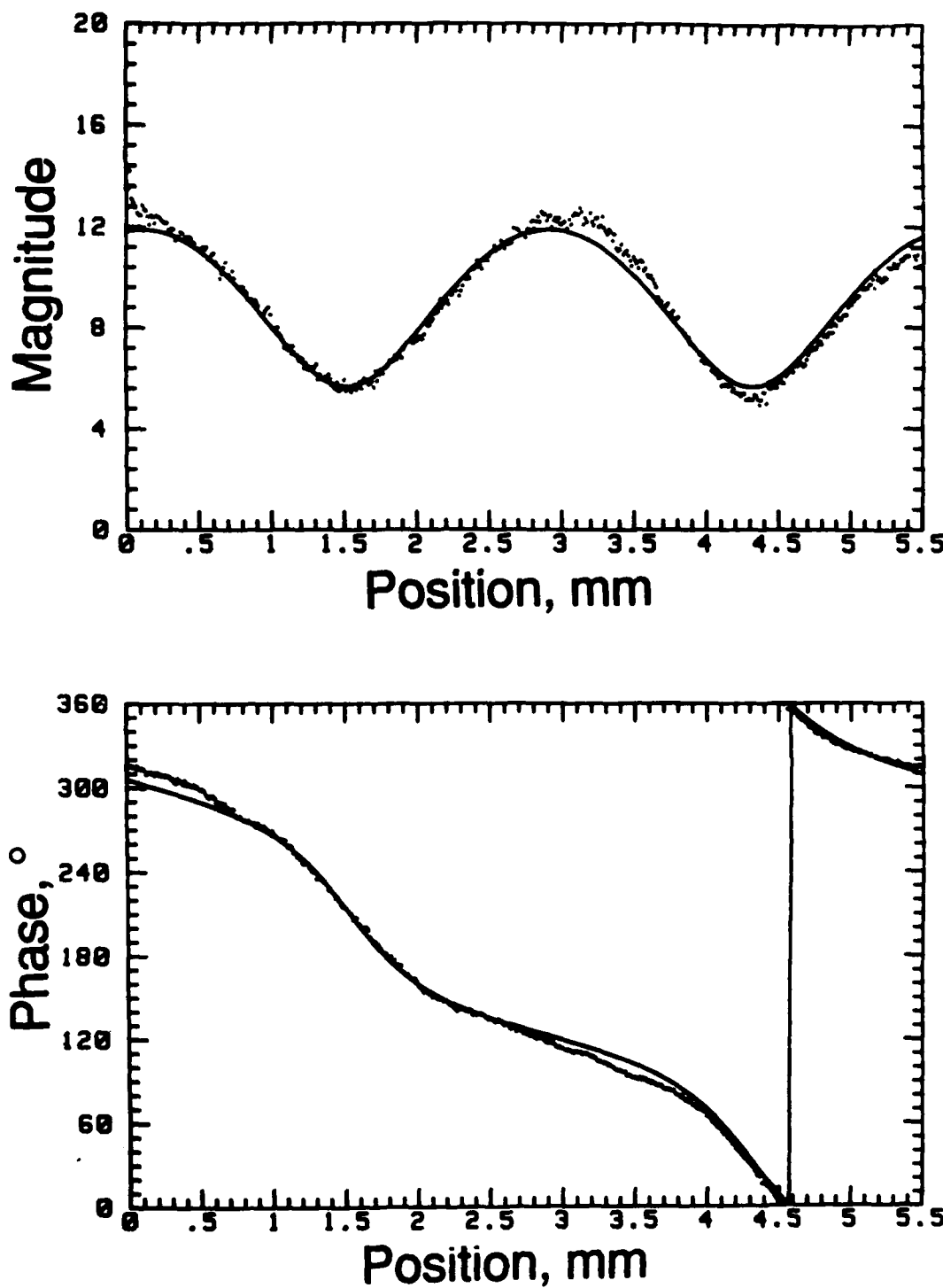


Figure 41: Magnitude (a) and phase (b) of a 20 GHz voltage standing wave on a GaAs coplanar waveguide transmission line with a mismatched termination. The points are the data and the solid line is the fitted curve. From this measurement a reflection coefficient of 0.35 @-15° is calculated.

measures voltages, but not currents, preventing a direct measure of 2-port parameters. Measuring the voltage as a function of position with the optical probe [62], similar to a slotted-line measurement, permits calculation of the incident and reverse waves on the transmission lines connecting to devices. From this information the network scattering parameters can then be determined.

The vector voltage due to the sum of the forward and reverse traveling waves on a lossless transmission line conductor is

$$V(z) = V^+ \exp(-j\beta z) + V^- \exp(+j\beta z) \quad (33)$$

where V^+ and V^- are the forward and reverse traveling wave coefficients, β is the wavenumber $2\pi/\lambda$, and z is the position. The traveling-wave coefficients are calculated by measuring this vector voltage as a function of position along a conductor using the optical probe then solving for these coefficients. For a one-port transmission line the ratio of the traveling wave coefficients V^+ and V^- is the reflection coefficient Γ , or S_{11} , the return loss. An example of such a measured vector standing wave and the calculated reflection coefficient for an unterminated CPW transmission line at a drive frequency of 40 GHz is shown in Figure 40, and a similar measurement with an unmatched load terminating the line at 20 GHz is shown in Figure 41. Extending this technique to calculate the incident and reflected waves on the input and output ports of a network allows for calculation of the S-parameters with a reference plane defined on the integrated circuit.

On GaAs microwave amplifiers and similar MMIC's, the propagation of microwave signals internal to the circuit can be measured. Figure 42 is a monolithic 2-18 GHz MESFET distributed amplifier from Varian Research Labs [63,64] with coplanar-waveguide transmission line interconnects. The circuit diagram is shown in Figure 43. In a distributed amplifier, a series of small transistors are connected at regular spacings between two high-impedance transmission lines. The high-impedance lines and the FET input and output capacitances together form synthetic transmission lines of 50Ω characteristic impedance. Series stubs are used in the drain circuit, equalizing the phase velocities of the two lines and providing partial matching between the low impedance of the output line and the higher output impedances of the FET's at high frequencies, thereby peaking the gain. Measurements of interest include the relative drive levels to the individual FET's as influenced by the loss and cutoff frequency of the synthetic gate line, the small-signal voltage at the drain of each FET, and identification of the saturation mechanisms leading to amplifier gain compression.

Figure 44 shows the small-signal gate voltages versus frequency for the amplifier of Figure 42; several features can be noted. The rolloff beyond 18 GHz is the cutoff frequency of the periodically-loaded gate line, the slow rolloff with frequency is the gate line attenuation arising from the real part of the FET input admittance, and the ripples are standing waves resulting from mistermination of the gate line (i.e. the load resistance not equal to the synthetic line's characteristic impedance.)

Similar measurements can be made on MMIC's using microstrip transmission lines. Figures 45 and 46 show the small-signal drain voltages versus frequency for a distributed amplifier with microstrip transmission lines (Figure 47, also from Varian Associates.) The strong variation with frequency and position results from interference of the forward and reverse waves on the drain transmission line.

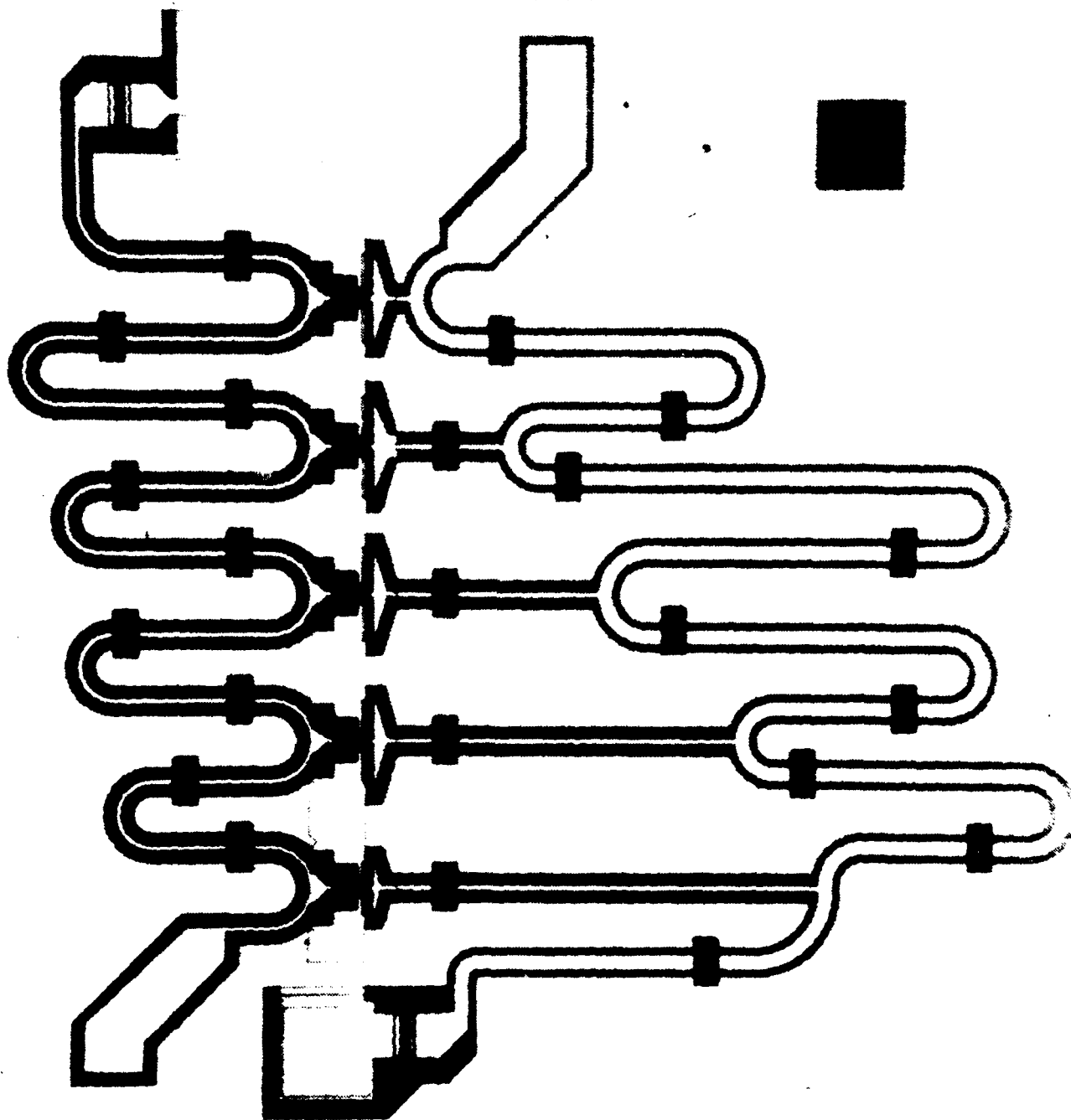


Figure 42: Traveling-wave amplifier using coplanar waveguide transmission-line interconnects[62].
Photo courtesy of M. Riazat, Varian Research Center

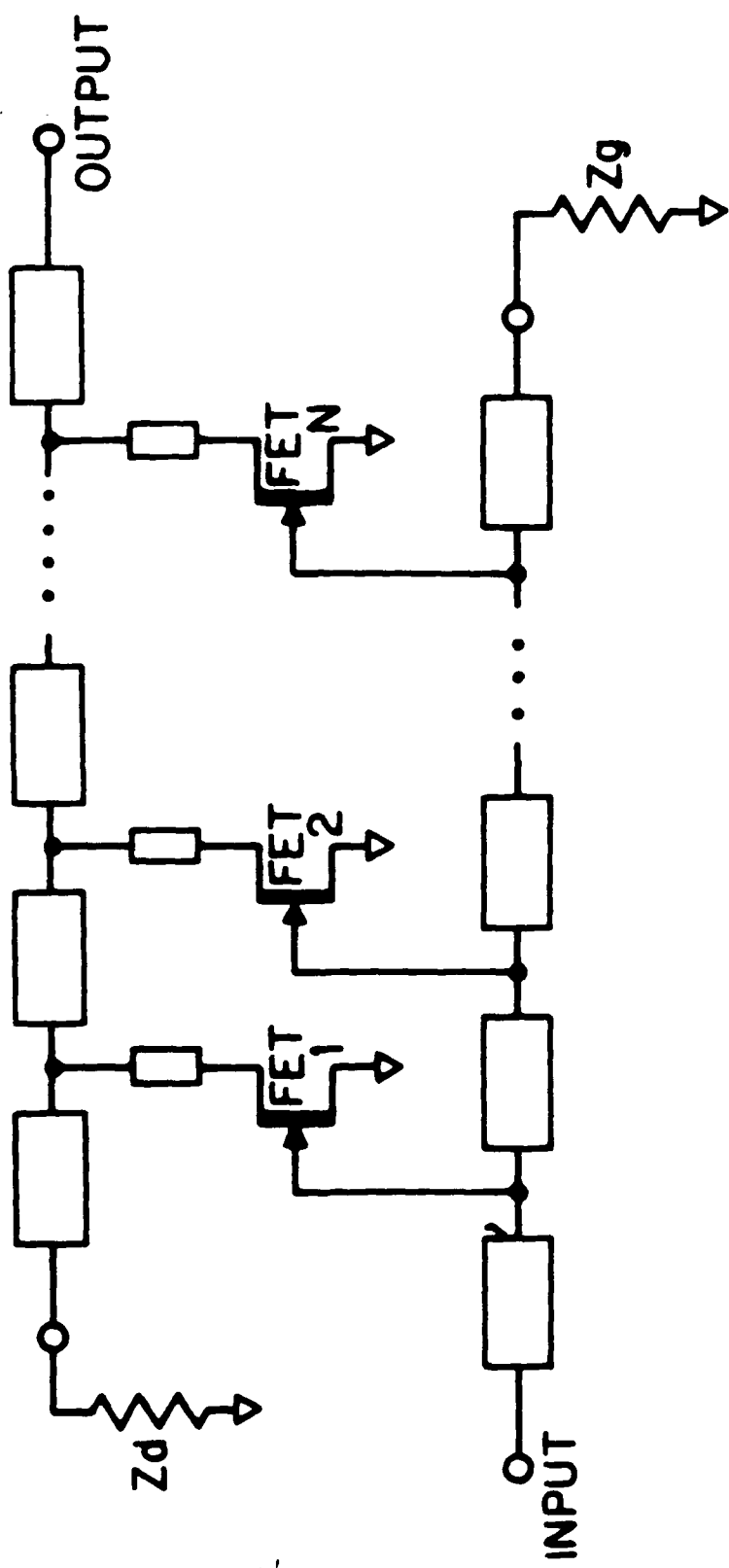


Figure 43: Circuit diagram of distributed amplifier.

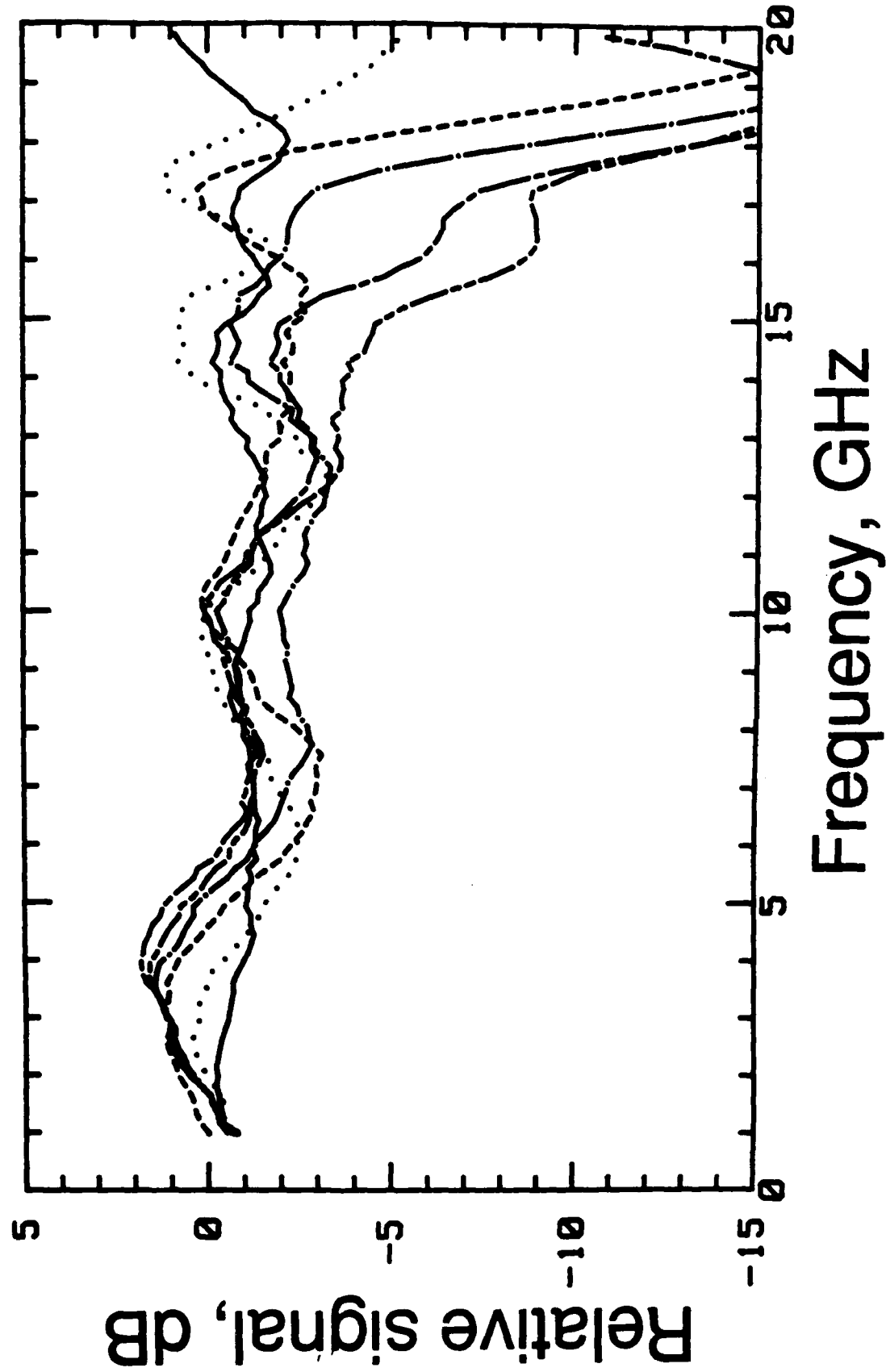


Figure 44: Small-signal voltages at the five gates and at the gate termination resistor in the coplanar 2 - 18 GHz distributed amplifier of Fig. 33. The line labeled 1 is the FET nearest the input, 2 is the next FET, and so on, until 6 which is the reverse termination.

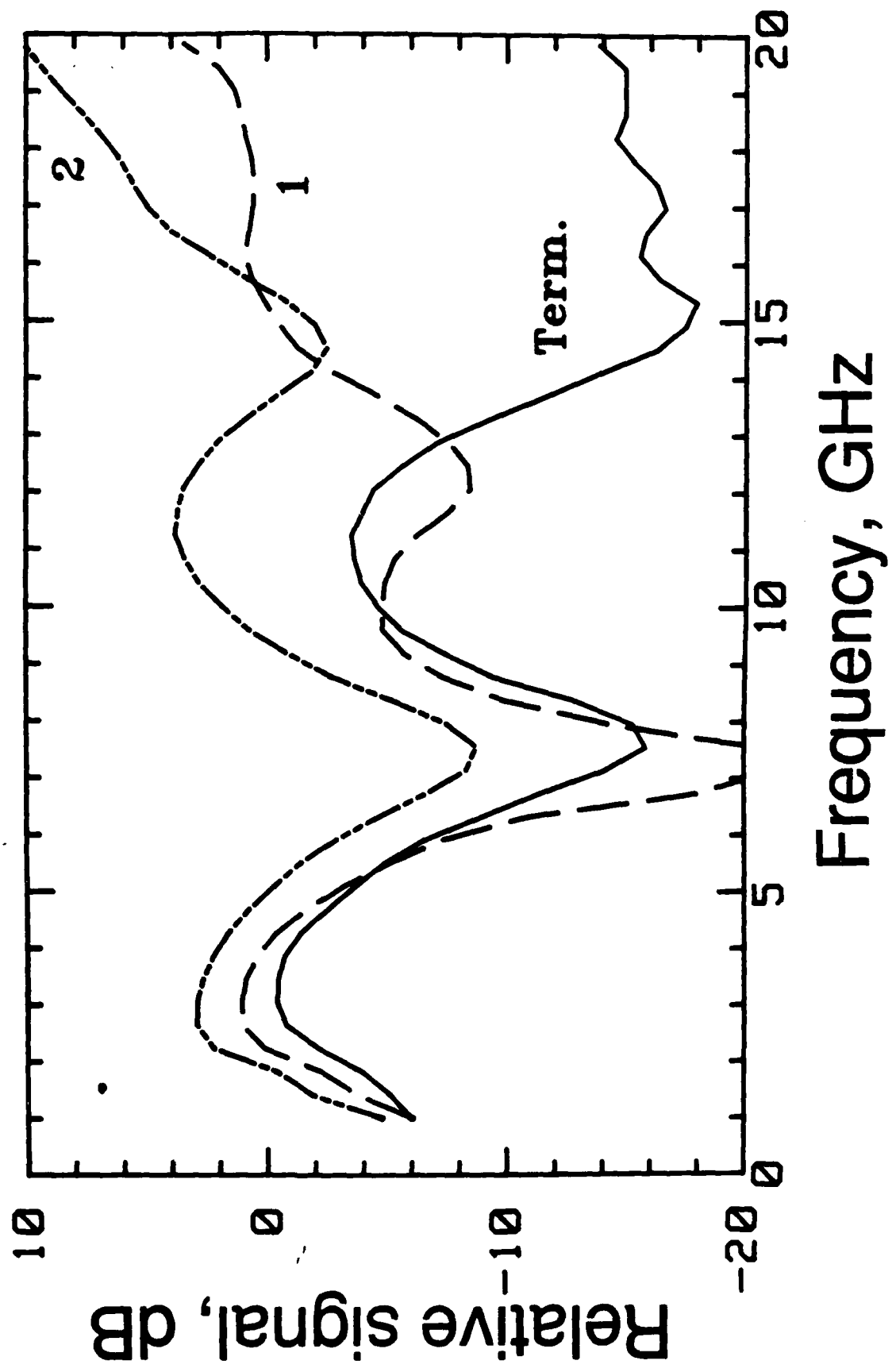


Figure 45: Small-signal voltages at the first and second drains, and at the drain line reverse termination resistor, in a 2-18 GHz distributed amplifier using microstrip transmission lines [61].

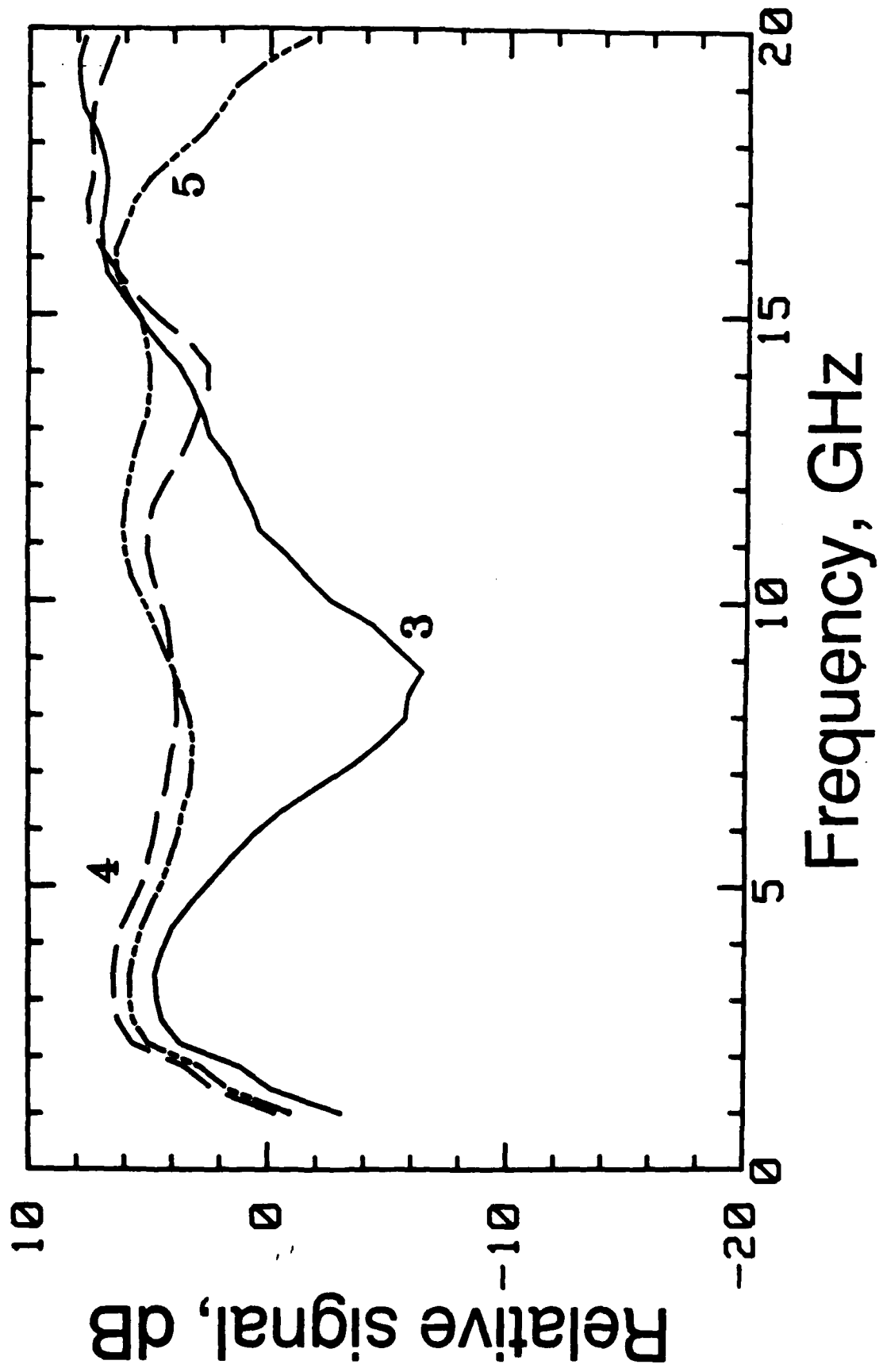


Figure 46: Small-signal voltages at drains 3, 4, and 5 of the microstrip distributed amplifier.

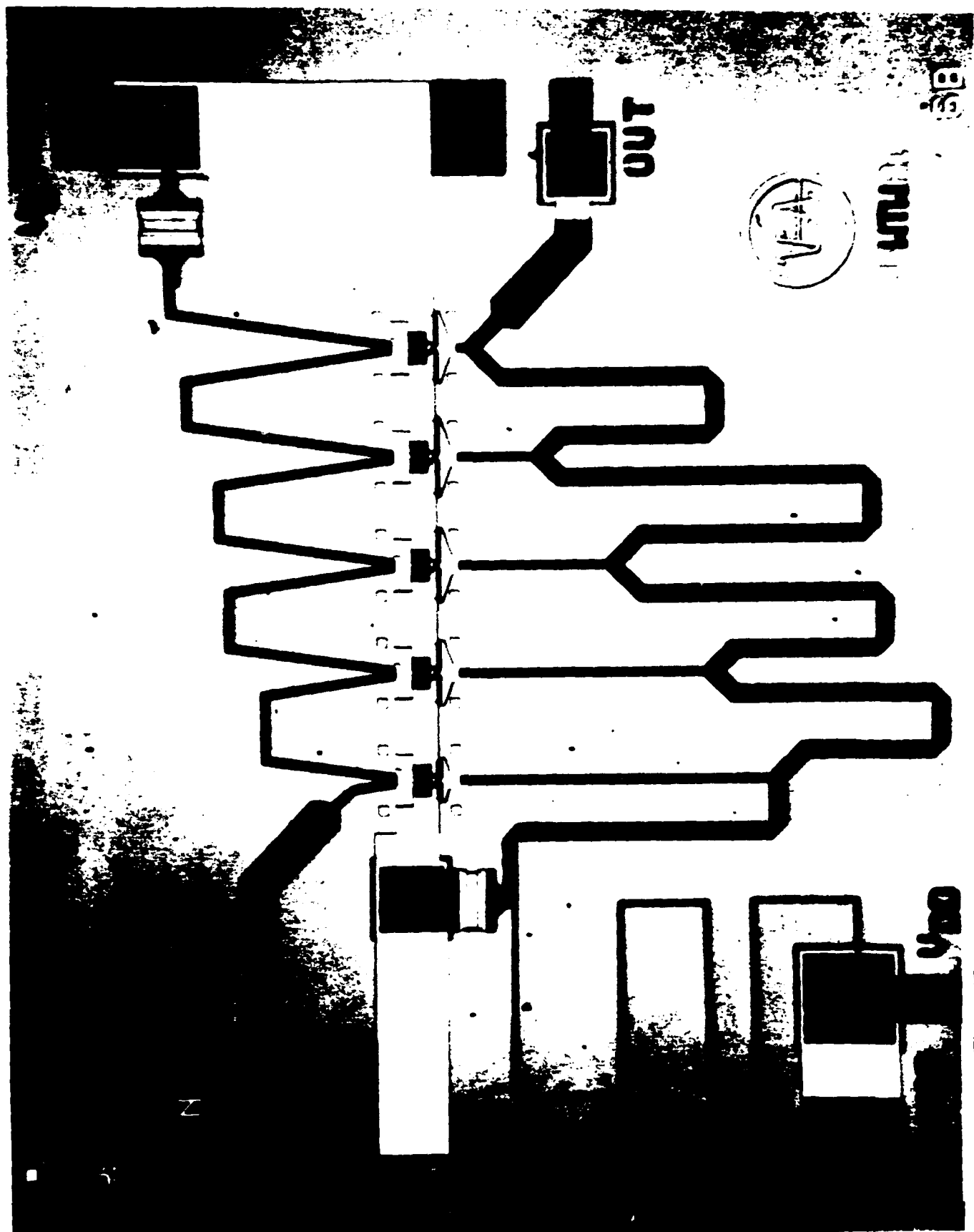


Figure 47: Traveling-wave amplifier using microstrip transmission line interconnects [62]. Photo courtesy of R. LaRue, Varian Research Center.

Used in the synchronous sampling mode, the electrooptic sampler can measure the voltage waveforms at internal nodes under conditions of circuit saturation, permitting identification of the saturation mechanisms. Figure 48 shows the voltage waveforms at drains 4 and 5 of the microstrip distributed amplifier operating at 10 GHz and 7 dBm input power, corresponding to the 1 dB gain compression point. For this amplifier, at frequencies above 5 GHz, gain saturation arises predominantly from drain saturation (i.e. reduction of V_{dg} to the point where the drain end of the channel is no longer pinched off) of the fourth and fifth FET's. Saturation at drive frequencies as high as 21 GHz can be observed (Figure 49). Even if the probed points had been accessible with electrical probes, these measurements would not be possible with sampling oscilloscopes (due to limited bandwidth), spectrum analyzers (magnitude response only), or network analyzers (small-signal response only).

4.4. Millimeter-wave circuit measurements

The probe station for on-wafer millimeter-wave measurements of GaAs devices and circuits consists of the electrooptic sampler and a new device, the active probe. The active probe converts an input microwave signal to a higher harmonic at millimeter-wave frequencies and delivers it to the device or circuit under test on the wafer. It is, in essence, a source multiplier. Millimeter-wave characterization of GaAs devices and circuits have been performed on a Cascade probe station modified for electrooptic sampling. The bandwidth of the electrooptic sampling system, discussed in Section 3.2, has a 3 dB point in excess of 200 GHz. The timing jitter of the laser output pulses corresponds to a phase uncertainty of approximately $\pm 12^\circ$ at 100 GHz.

A. Active probe

Conventional millimeter wave sources have waveguide outputs incompatible with wafer probing [65]. To bring the millimeter-wave signal on-chip without waveguides, an active probe frequency multiplier has been developed [66]. The active probe has a coaxial input and a coplanar waveguide (CPW) output which contacts the device's input ground-signal-ground pads. A 12-20 GHz input signal to the active probe, provided by a commercially available microwave synthesizer, is quintupled to generate the 60-100 GHz output signal. Vector or time waveform measurements of devices can then be made (see Sections 4.1-4.3) electrooptically.

The active probe, shown schematically in Figure 50, consists of a low-pass filter and an input matching network before the nonlinear element. A beam-lead antiparallel GaAs Schottky diode pair was used as the nonlinear element [67], [68], with a matching network and a bandpass filter at the output to pass the fifth harmonic and to reject the fundamental and the undesired harmonics [69]. The circuit design was implemented in coplanar waveguide with the layout shown in Figure 51. The assembled active probe (Figure 52) closely resembles commercial passive probes used at lower frequencies. A maximum output power of -15 dBm between 60-100 GHz was obtained from the first iteration design of the active probe quintupler. The minimum conversion loss was approximately -32 dB.

The output waveform of the active probe at 77 GHz (input frequency = 15.4 GHz) is shown in Figure 53. Since the output bandpass filter of the frequency multiplier does not completely reject the

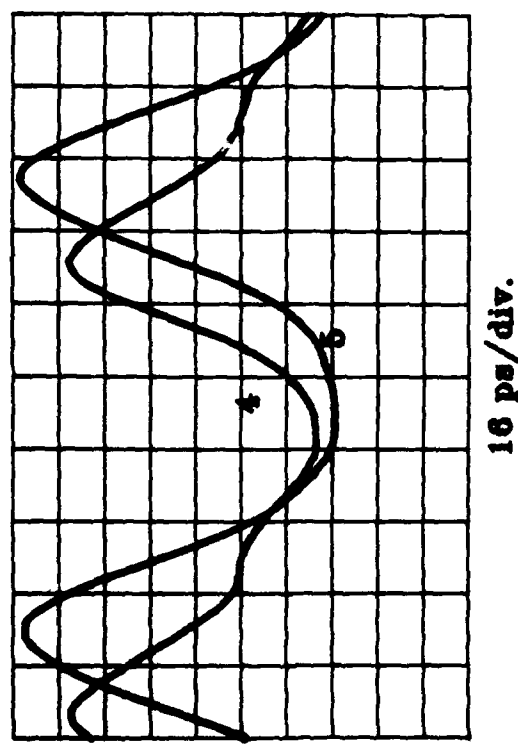


Figure 48: Saturation at draws 4 and 5 of the microstrip distributed amplifier at 10 GHz and 7 dBm input power, the 1 dB gain compression point.

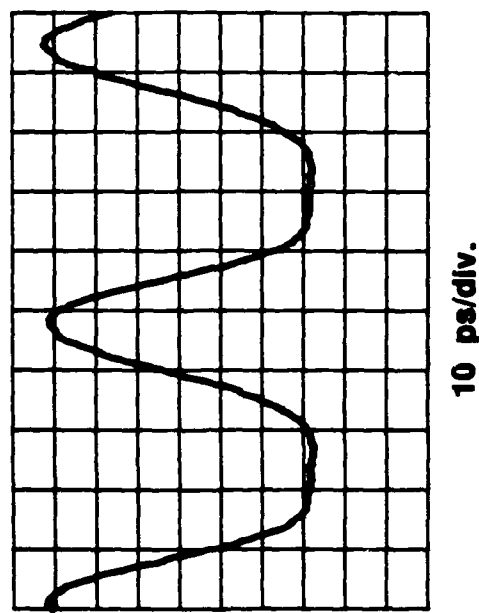


Figure 49: Saturation at drain 3 of the microstrip distributed amplifier at 21 GHz drive frequency.

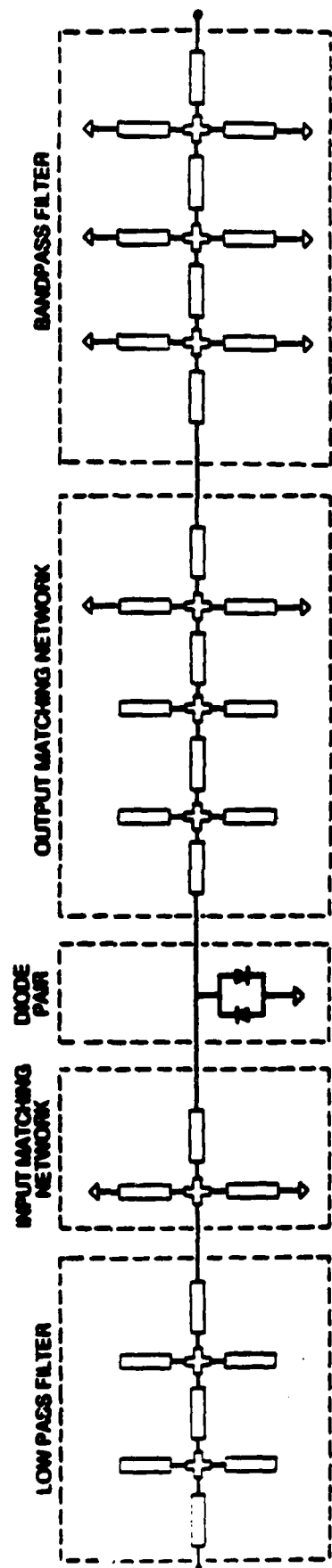


Figure 50: Schematic circuit diagram of the active probe quintupler which generates the millimeter-wave input signal to the device under test for on-wafer characterization of GaAs devices and IC's using electrooptic sampling technique. The quintupler circuit consists of a lowpass filter and an input matching network before the nonlinear element followed by an output matching network and a bandpass filter.

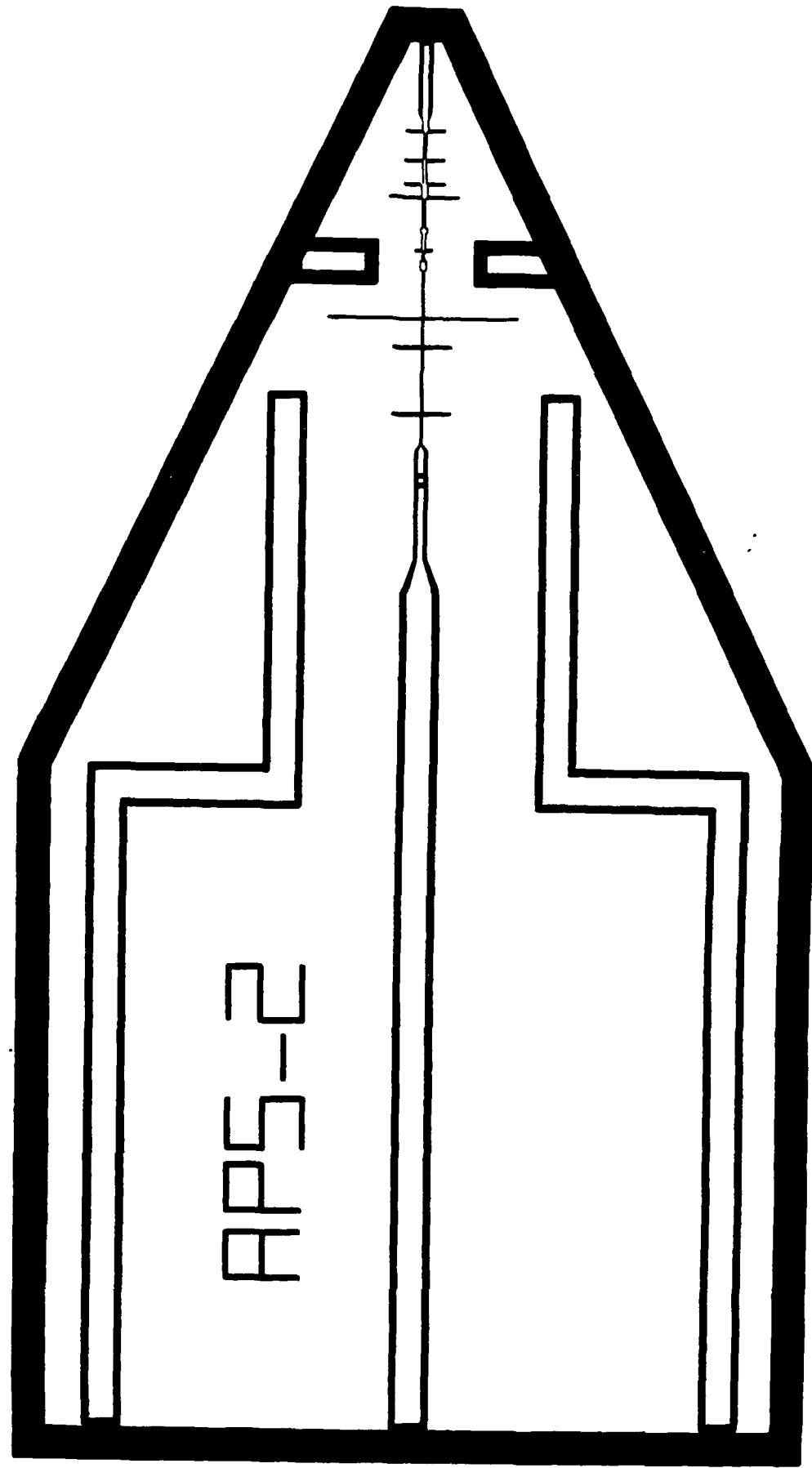


Figure 51: Circuit layout of the frequency multiplier active probe. The quintupler circuit, the 50 ohm CPW's connecting the quintupler circuit to the CPW-to-coax transition and the output pads and the DC lines which provide the bias to the diodes are included in the circuit layout.

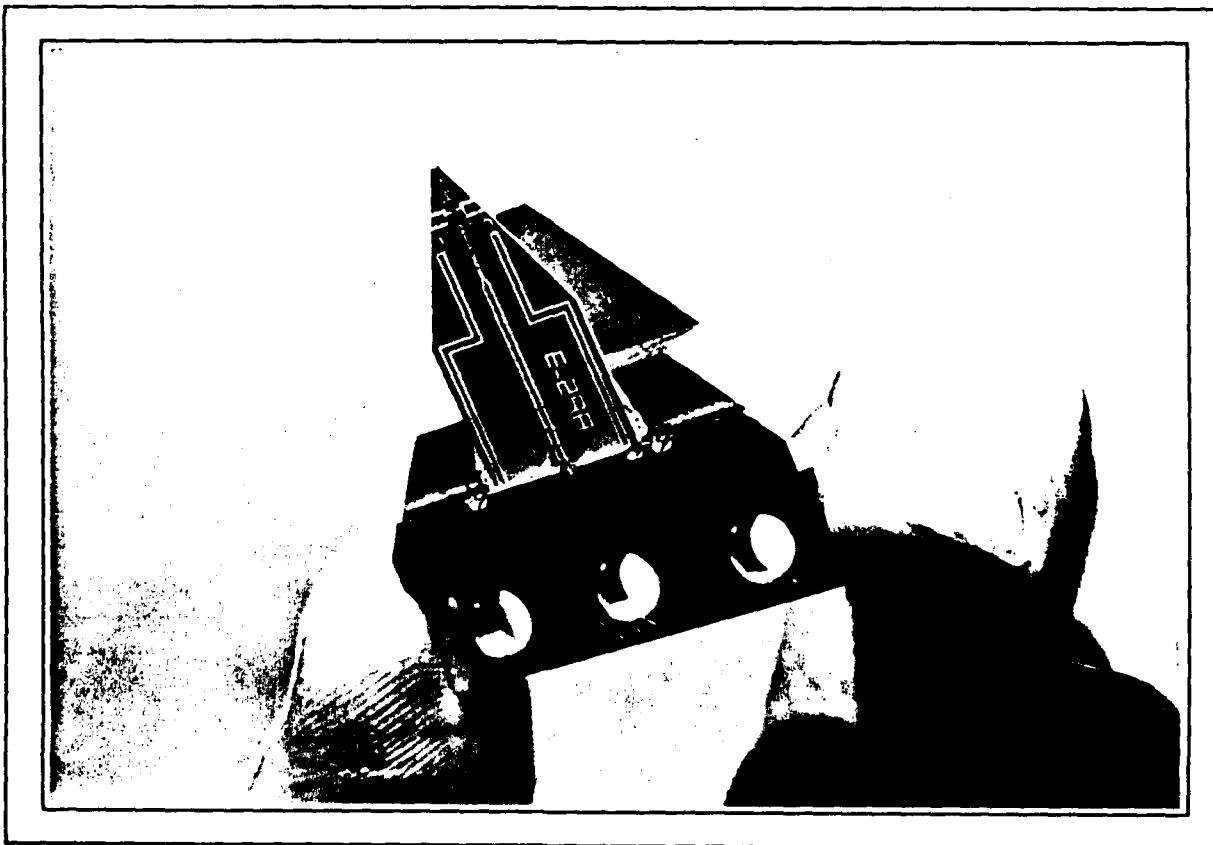
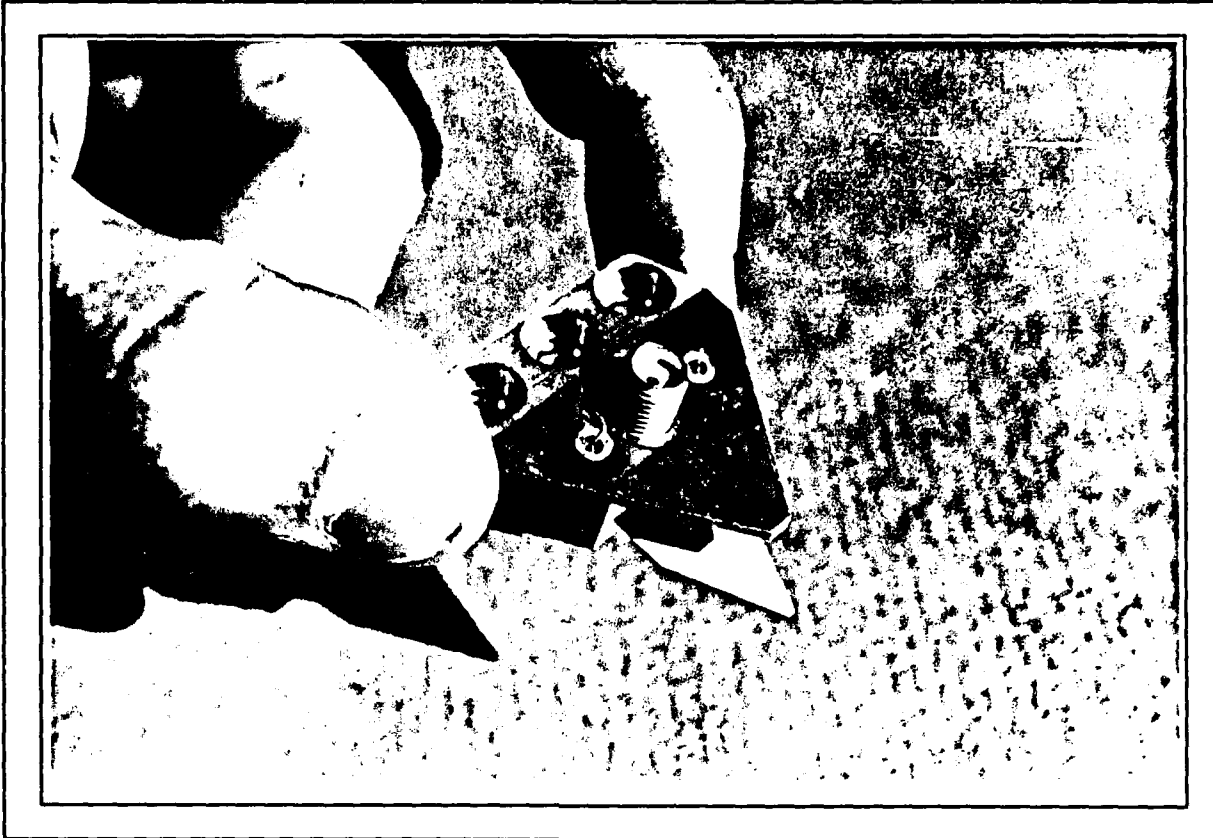


Figure 52: Photographs of assembled 60-100 GHz active wafer probe. In use the probes are mounted in the electrooptic probe station to provide millimeter-wave drive signals to circuits under test.

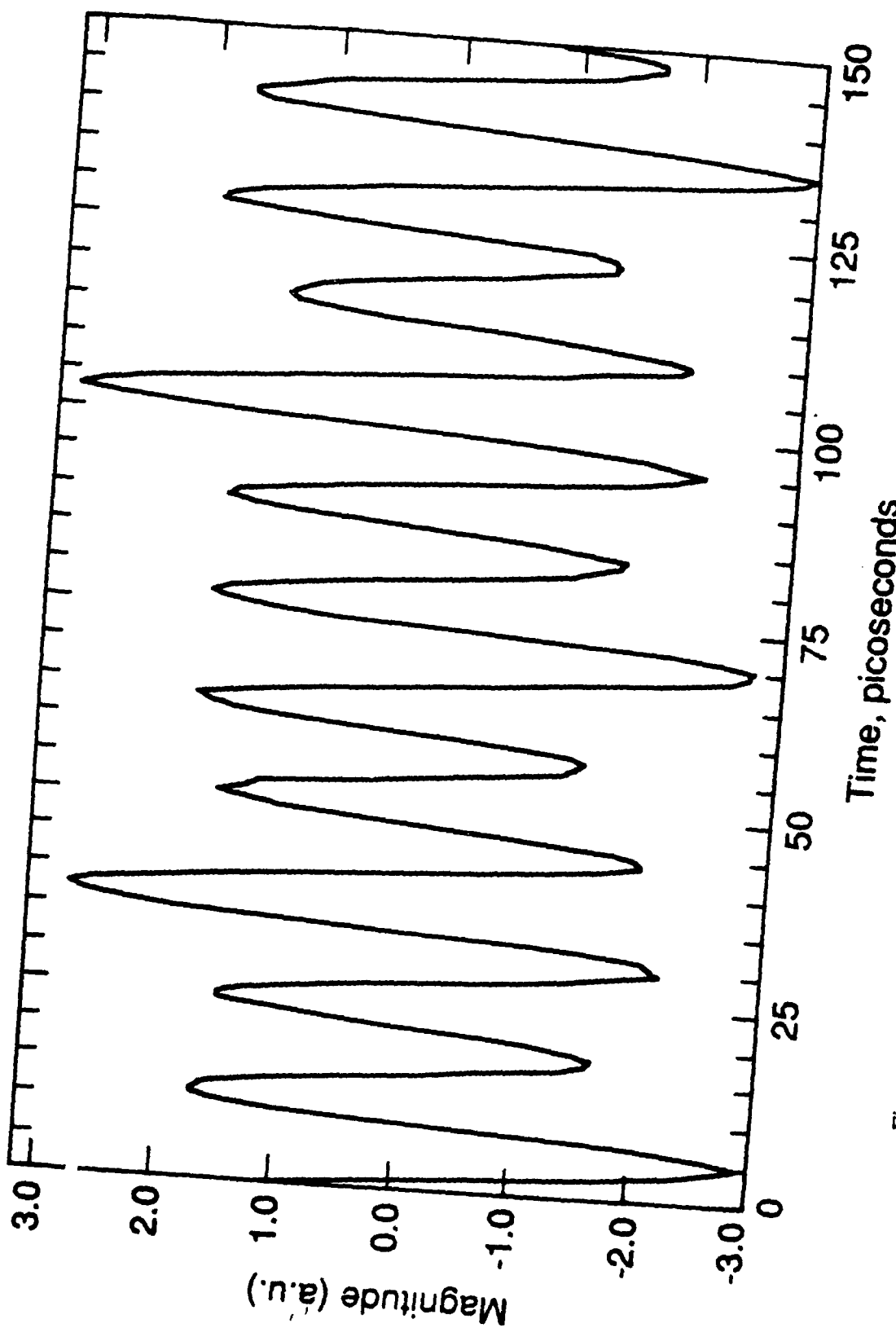


Figure 53: Time-waveform of the frequency multiplier active probe at 77 GHz on a 50 ohm CPW. The waveform has an envelope at 15.4 GHz due to finite rejection of the fundamental frequency by the output bandpass filter of the frequency multiplier.

component of the signal at the fundamental frequency, the output waveform at 77 GHz has an envelope at 15.4 GHz.

The active probe promises to extend the range of coaxial millimeter-wave network analysis. The frequency range of conventional network analyzers, such as the HP 8510, is extended to millimeter-wave frequencies by using an external frequency-multiplier and harmonic mixers with waveguide inputs and outputs. A harmonic-mixer active probe with a CPW input and a coaxial output, used in conjunction with the frequency-multiplier active probe, would provide a non-optical alternative approach for millimeter-wave linear network analysis. In this approach, the input millimeter-wave test signal is supplied by the frequency-multiplier active probe to a device under test. The output of the device then would be down-converted in the harmonic-mixer active probe to an intermediate frequency for detection and post-processing by a conventional network analyzer.

The development of a harmonic-mixer active probe directly benefits from the work done on the frequency-multiplier active probe. A scaled model of the harmonic mixer active probe has been developed and evaluated. By using calibration standards fabricated on GaAs the systematic errors in the measurements of GaAs devices and ICs can be corrected.

Extension of the active probes to 300 GHz will require monolithic integration of the nonlinear circuit elements. At Stanford, integrated millimeter-wave diodes with cutoff frequencies in excess of 1 THz have been fabricated. By exploiting this in-house technology, 300 GHz probes should be feasible.

B. Millimeter-wave potential mapping

Planar transmission lines are the most suitable geometries for millimeter-wave integrated circuits on GaAs. Although the most commonly used planar transmission line is microstrip, coplanar structures, where the ground and signal conductors are on the same plane (see Figure 54), are becoming more popular. Coplanar waveguide (CPW) [70], slot line [71], [72], and coplanar strips (CPS) are the best known transmission lines of this type. They have significant advantages over microstrip for monolithic microwave integrated circuit (MMIC) applications at millimeter-wave frequencies [73]. These advantages include low sensitivity to substrate thickness variation, low-inductance access to topside ground plane, realization of both series and shunt transmission line stubs, planar shunt connection of devices, and novel structures based on CPW-slot line junctions.

Electrooptic sampling has been used to measure propagation properties of these uniplanar transmission lines [74], [75]. The terms CPW and coupled slot line are used interchangeably, referring to the same physical structure [76]. The CPW mode, which is the same as the odd mode of the coupled slot line, has the electric fields of opposing polarity in the two slots. The even mode of the coupled slot line, referred to as the coupled slot mode, has the electric fields of the same polarity in the two slots. When the CPW mode is used, the coupled slot mode is suppressed by shorting the two outer conductors with an air bridge. Two different Cascade probes excited the even and odd modes of CPW, slot line and CPS: for the CPW odd mode, a ground-signal-ground probe was used; for the CPW even mode, slot line and CPS, a signal-ground-signal probe was used.

By scanning the optical beam across the conductors, transverse to the direction of propagation, the potential distribution over the guide cross section is measured. The transverse potential distributions

of the CPW, slot line and the CPS were measured. Figure 55 shows the cross section and the potential distribution of the odd mode of the CPW. In the odd mode the signal is applied to the center conductor and the outer conductors are at ground potential as indicated by the data. The cross section and transverse potential of slot line is shown in Figure 56. Figure 57 shows the results of the transverse scan and the cross section of CPS. In the slot line and CPS the difference in the potential amplitude on the two conductors is due to the presence of unbalanced modes. These undesired modes are excited by the imperfect launching of the signal from the Cascade probe. The standing wave measurements of the slot line and CPS verified the presence of these parasitic modes.

Measurement of standing waves on uniplanar guides were obtained by scanning the probe along the direction of propagation. Figure 58 shows the magnitude and phase of the odd mode voltage standing wave on the center conductor at 18.464 GHZ. Even mode measurement results at 18.464 GHZ are shown in Figure 59. The standing waves on slot line and CPS at 40 GHz are shown in Figures 60 and 61. In the standing waves measured on the slot line, the amplitudes of the minima are not equal to zero and there are also variations in the amplitudes of the maxima and minima. The cause of these deviations is the propagation of undesired unbalanced modes in addition to the fundamental balanced mode, as described in the preceding section. Because the guide wavelengths for these undesired modes differ from the guide wavelength of the fundamental mode, the undesired and desired modes interfere, changing the amplitudes of the maxima and minima of the standing waves as a function of distance along the direction of propagation.

The single-mode guide wavelength of a 50Ω CPW under odd-mode excitation was measured from 15 to 100 GHz (see Figure 62) and, under even mode excitation, from 15 to 40 GHz (see Figure 63). The odd mode was excited by applying the signal to the center conductor and grounding the outer conductors. The same CPW was then excited in the even mode by applying two signals of equal amplitude and opposite phase to the outer conductors and grounding the center conductor. Note that the dispersion of the odd mode is significantly less than the even mode. The standing wave measurements from 15 to 40 GHz were then repeated on the slot line. The dispersion characteristics are shown in Figure 64. Since the cutoff frequency of the lowest order quasi-slab mode is 45 GHz, coupling to parasitic slab modes can be ignored in all three cases.

These dispersion characteristics are particularly important in designing broadband millimeter-wave GaAs integrated circuits. Still under investigation are the dispersion of higher-order modes of CPW. Such higher-order modes significantly affect the dispersion characteristics of the quasi-TEM mode. Electrooptic sampling has been used to experimentally determine the frequency range of strong coupling and interaction between the quasi-TEM mode and the higher order slab modes. Empirical design rules will eventually be derived from these measurements and used to design broadband CPW millimeter-wave integrated circuits on GaAs.

C. Nonlinear network analysis

Because power amplifiers, frequency multipliers, and limiters are inherently nonlinear, their behavior cannot be characterized by the linear concept of S-parameters. Instead, the time waveform must be studied directly. The electrooptic probe used in the equivalent-time sampling mode can directly measure these distorted waveforms. We have used this approach for nonlinear waveform measurements up to 100 GHz, in designing and evaluating several important nonlinear circuits.

The distorted time-waveforms provide information about the type of nonlinearity and its magnitude. The time-waveform of the frequency multiplier active probe output, measured electrooptically, was shown in Figure 52. A 15.4 GHz sinusoidal input waveform is distorted and filtered by the multiplier to generate the fifth harmonic, at 77 GHz. By extracting the device parameters from the large-signal measurements, computer simulation models can be derived and used to optimize circuit and device design.

D. S-parameter measurements

Understanding the physics and frequency limitations of millimeter-wave devices requires accurate characterization of the operational parameters. Conventional network analyzers, such as the HP-8510, operate to 26.5 GHz. Calibration is typically obtained by a series of measurements resulting in a twelve-term error model. Extrapolation to higher frequencies of S-parameters measured below 26.5 GHz using conventional network analyzers does not provide an accurate millimeter-wave characterization of these devices. To extend the frequency range of network measurement instruments to 100 GHz, external frequency multipliers and mixers with waveguide outputs are added and a waveguide fixture for the device is used. They result in a significant reduction in the measurement accuracy.

An alternative is on-chip 100 GHz S-parameter measurements using electrooptic sampling. The combination of 200 GHz electrooptic sampler bandwidth and an active wafer probe to provide input drive signals up to 100 GHz give a powerful new tool for S-parameter characterization. Calibration in the electrooptic approach is straightforward, requiring only a two-term error model for source and load mismatch corrections. Since this is an optical measurement technique, the harmonic mixer and waveguide fixturing of the device and the corresponding waveguide network are eliminated. This new technique opens the way to the accurate on-chip characterization of emerging millimeter-wave electronic devices and the development of a new industry standard for millimeter wave measurement methodology.

Figure 65 shows the standing wave measured by electrooptic sampling on a 50 ohm CPW terminated in a short circuit with a 100 GHz input signal supplied by the active probe. Using a linear estimation algorithm on a HP 9836 computer, the standing wave data obtained is converted to S-parameters. The reflection coefficient of the 1.0 millimeter long 50 ohm CPW terminated in a short circuit in Figure 65 was calculated to be 0.93 @ -94°. The frequency response of this one-port network was obtained by repeating the standing wave measurement at each frequency. Figure 66 shows an example of such a measurement of the same test structure obtained using the active probe and the electrooptic sampler over 60 to 100 GHz.

On-wafer S-parameter measurements of two-port networks at millimeter-wave frequencies using electrooptic sampling, are based on an extension of one-port network measurement scheme. Calibration is based on a two-term error model consisting of load and source match error terms. The measured S-parameters are then corrected for these error terms. Figure 67 shows 50 to 95 GHz S-parameter measurements of a test structure consisting of a 25 ohm CPW of 500 microns length. Also shown in that Figure is the frequency response of a simple CPW model which does not include the effects of the discontinuities and the losses. Although the ground-to-ground spacing of

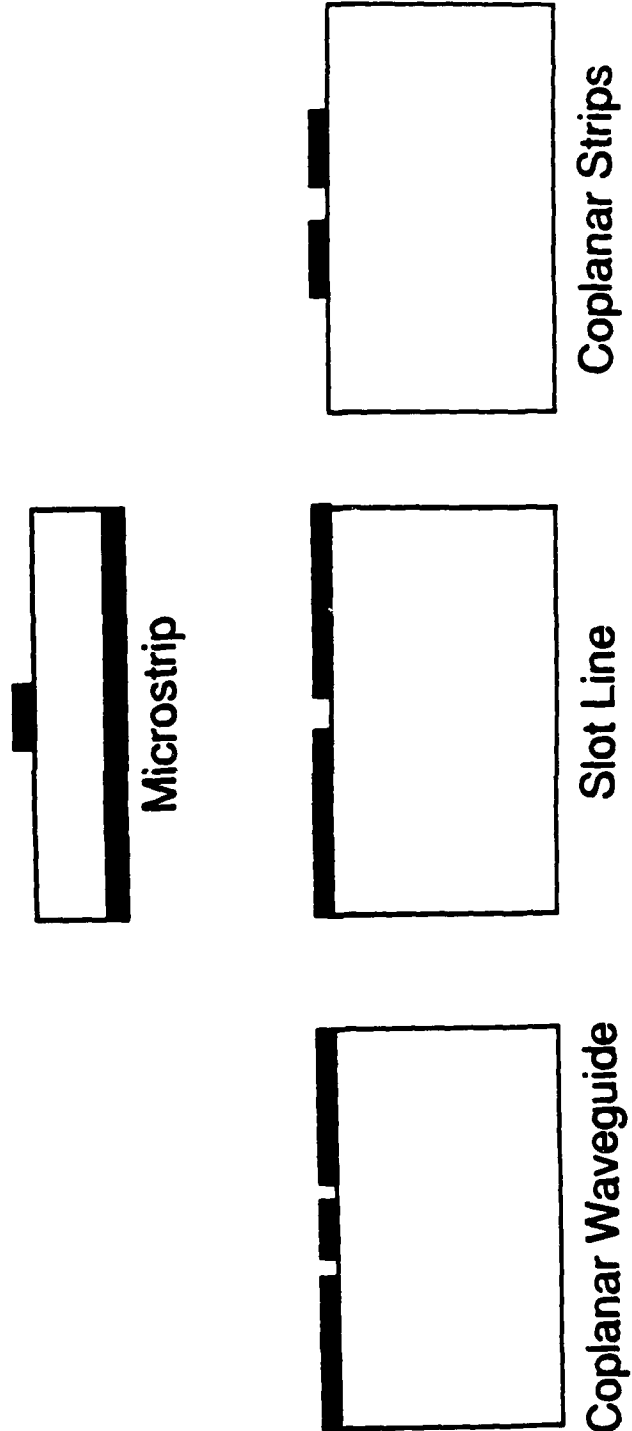


Figure 54: Cross sections of microstrip, CPW, slot line and CPS. Uniplanar guides, including CPW, slot line and CPS have all their conductors in the same plane on the top-side of the substrate, thus making them with backside probing using electrooptic sampling. Microstrip, in contrast, has conductors on both sides of the substrate and therefore frontside probing is used in making electrooptic sampling measurements.

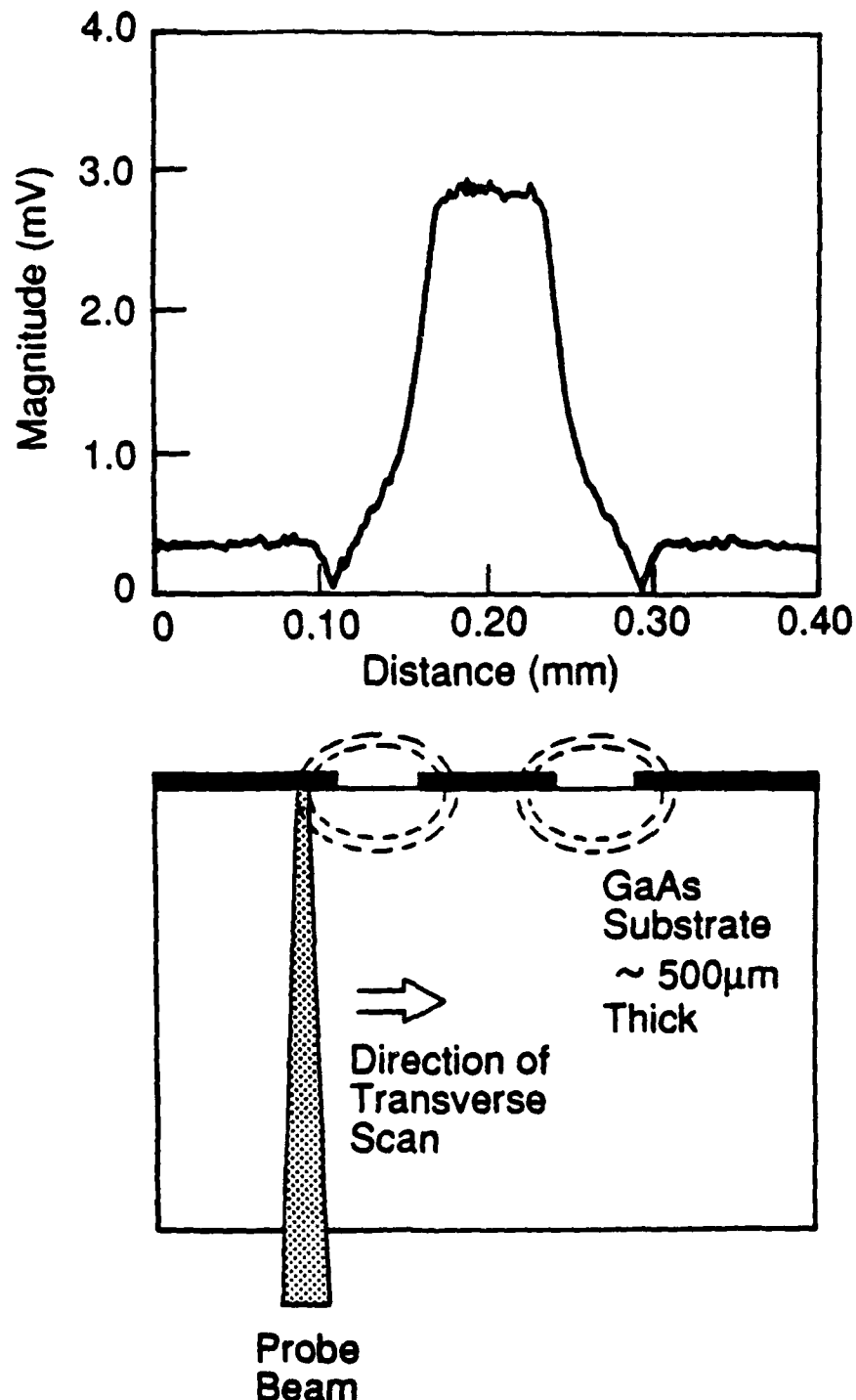


Figure 55: Transverse potential distribution of CPW odd mode. The test structure had 180 microns ground-to-ground spacing, a center conductor width of 80 microns and 50 microns wide gaps on a 500 microns thick GaAs substrate. The outer conductors were at ground potential and the signal is applied to the center conductor. The non-zero potential shown in the figure is due to the non-zero back-side potential.

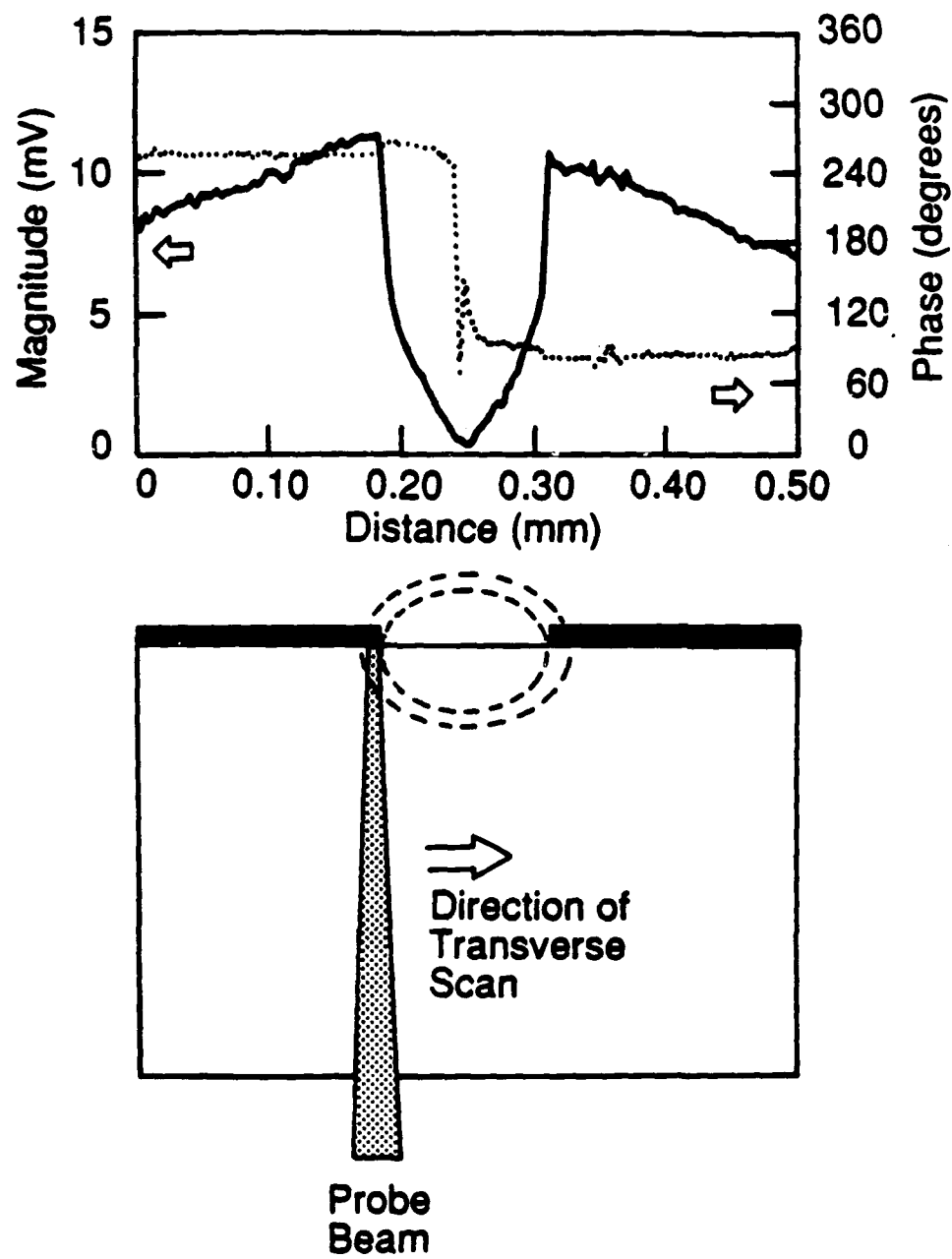


Figure 56: Transverse potential distribution of slot line. The test structure has a slot width of 125 microns on a 500 microns thick GaAs substrate. The voltage on the two conductors are equal in magnitude and 180° out-of-phase. The small difference in the magnitudes of the voltages on the two conductors, is due to a combination of the variations in the metal reselectivities for the optical beam and presence of small amount of undesired unbalanced modes.

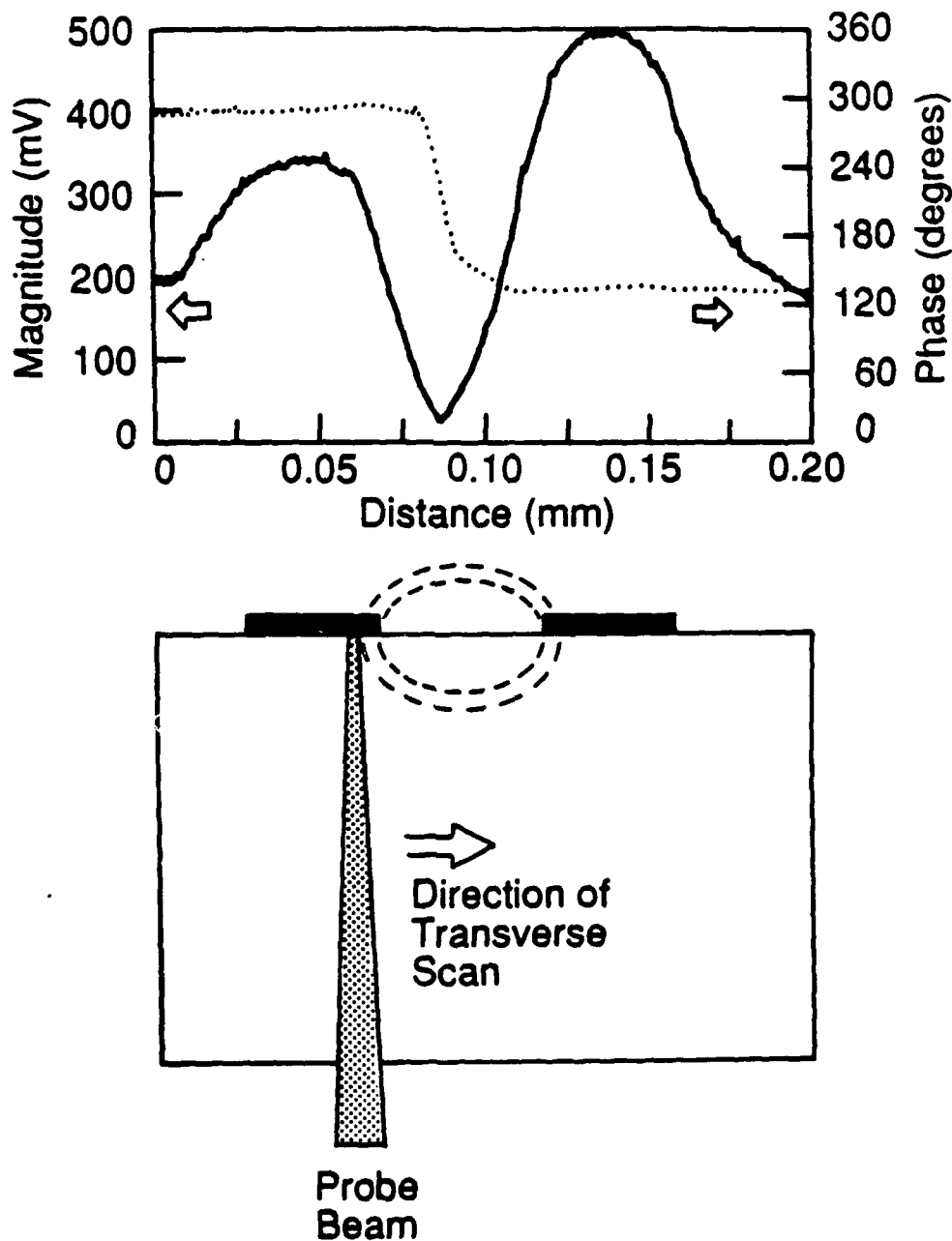


Figure 57: Transverse potential distribution of CPS. The test structure had microns wide conductor strips separated by a microns wide gap on a 500 microns thick GaAs substrate. The difference in the magnitudes of the voltages on the two conductors was due to the presence of the unbalanced modes. The phase difference however was still 180° .

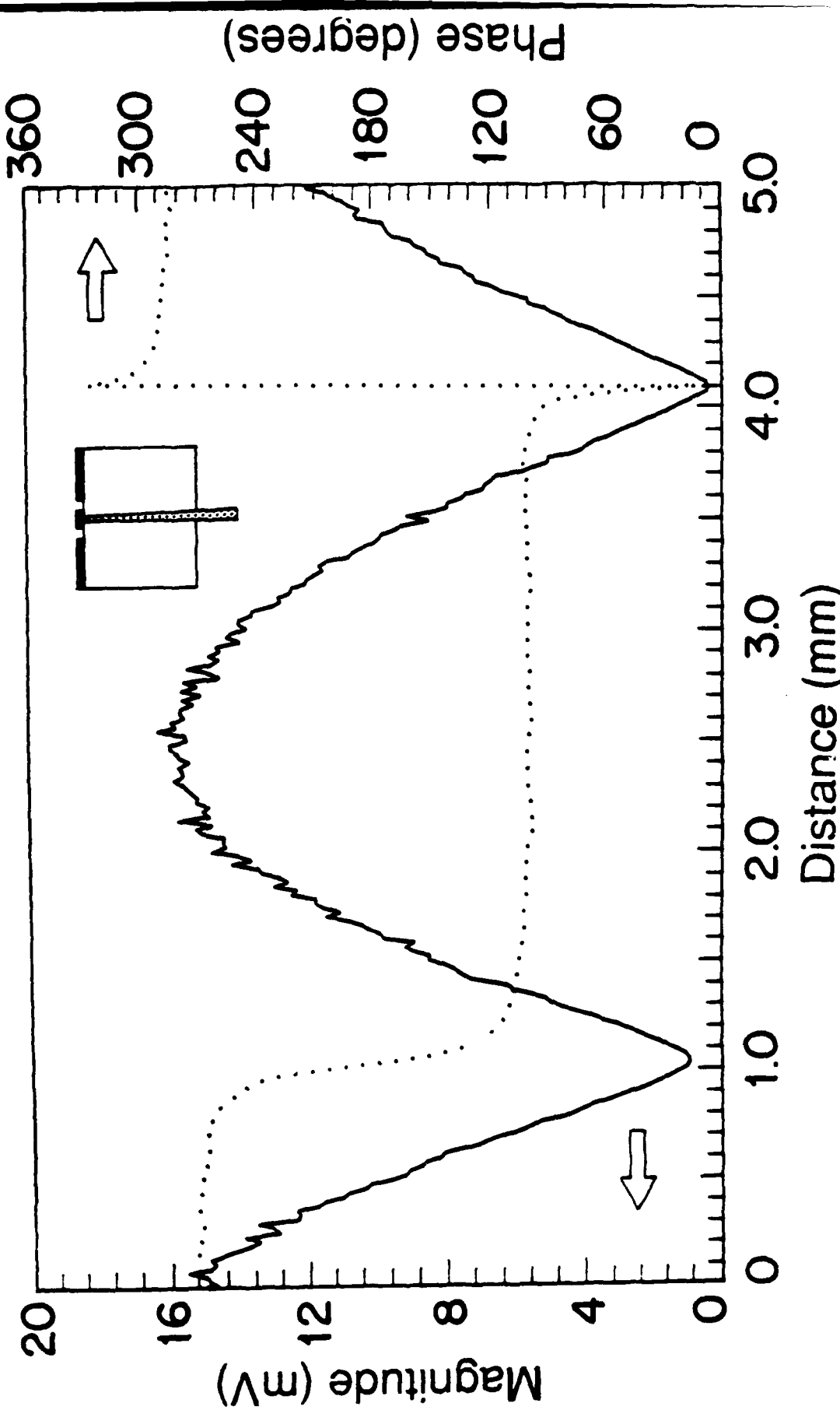


Figure 58: Magnitude and phase of the CPW odd mode 18.5 GHz standing wave. The standing wave minima are separated by 3.1 mm which is half of the odd mode wavelength at 18.5 GHz. The phase changes by 180° at the positions of the minima.

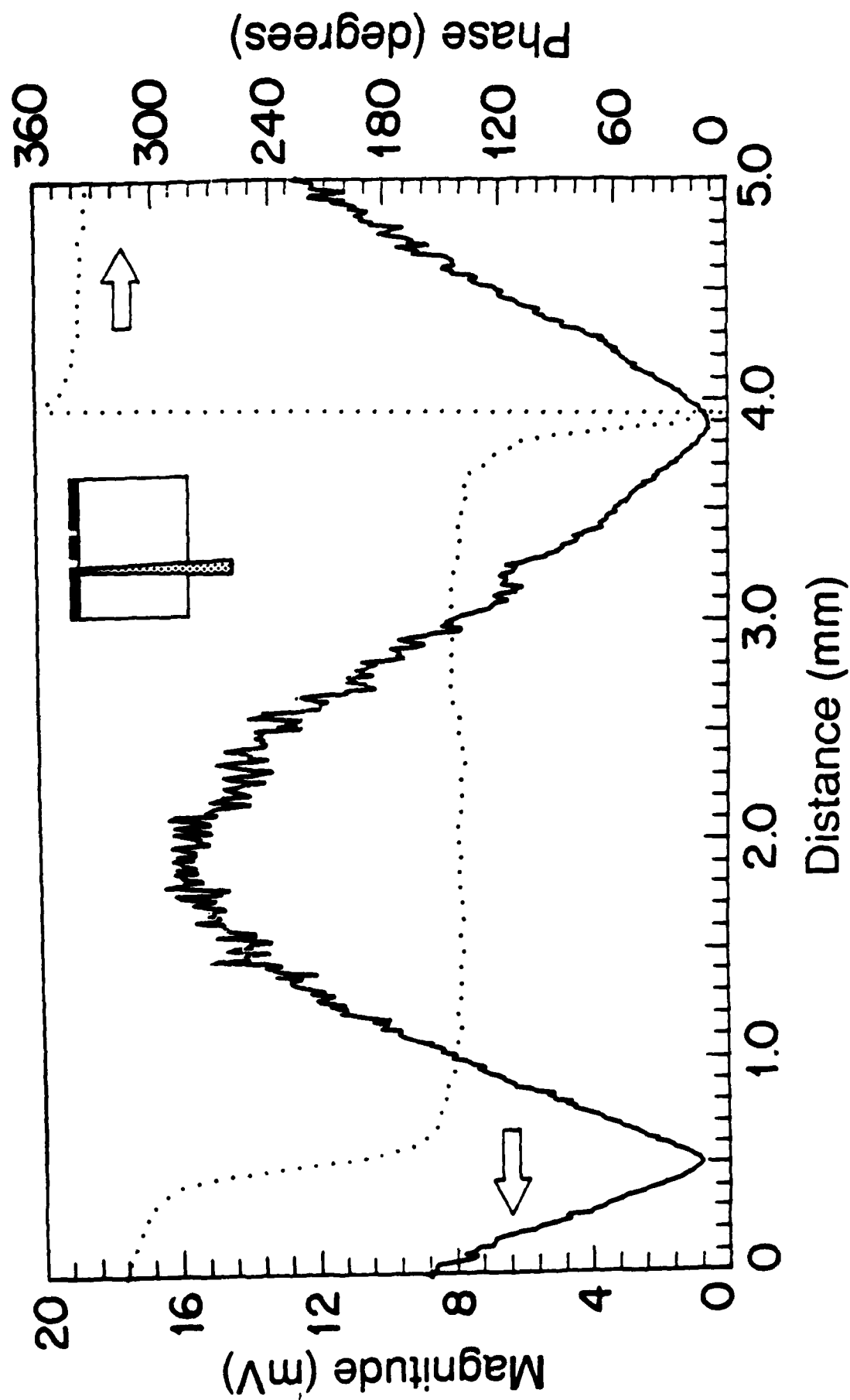


Figure 59: Magnitude and phase of the CPW odd mode 18.5 GHz standing wave. The standing wave minima are separated by 3.4 mm which is half of the even mode guide-wavelength at 18.5 GHz. The phase changes by 180° at the positions of the minima.

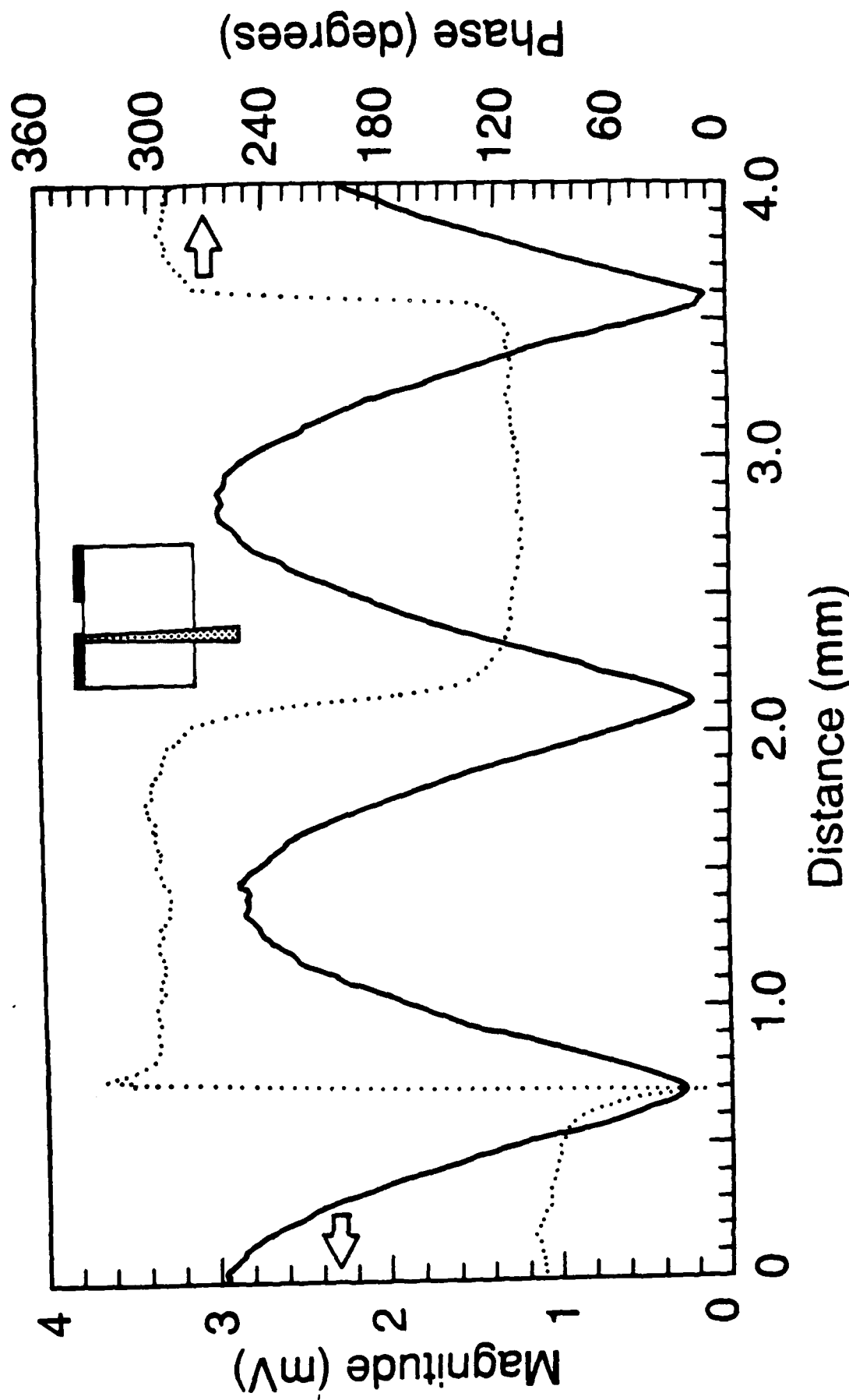


Figure 60: Magnitude and phase of the slot line 40 GHz standing wave. The standing wave minima are separated by 1.45 mm which is half of the slot line guide-wavelength at 40 GHz. The phase changes by 180° at the positions of the minima.

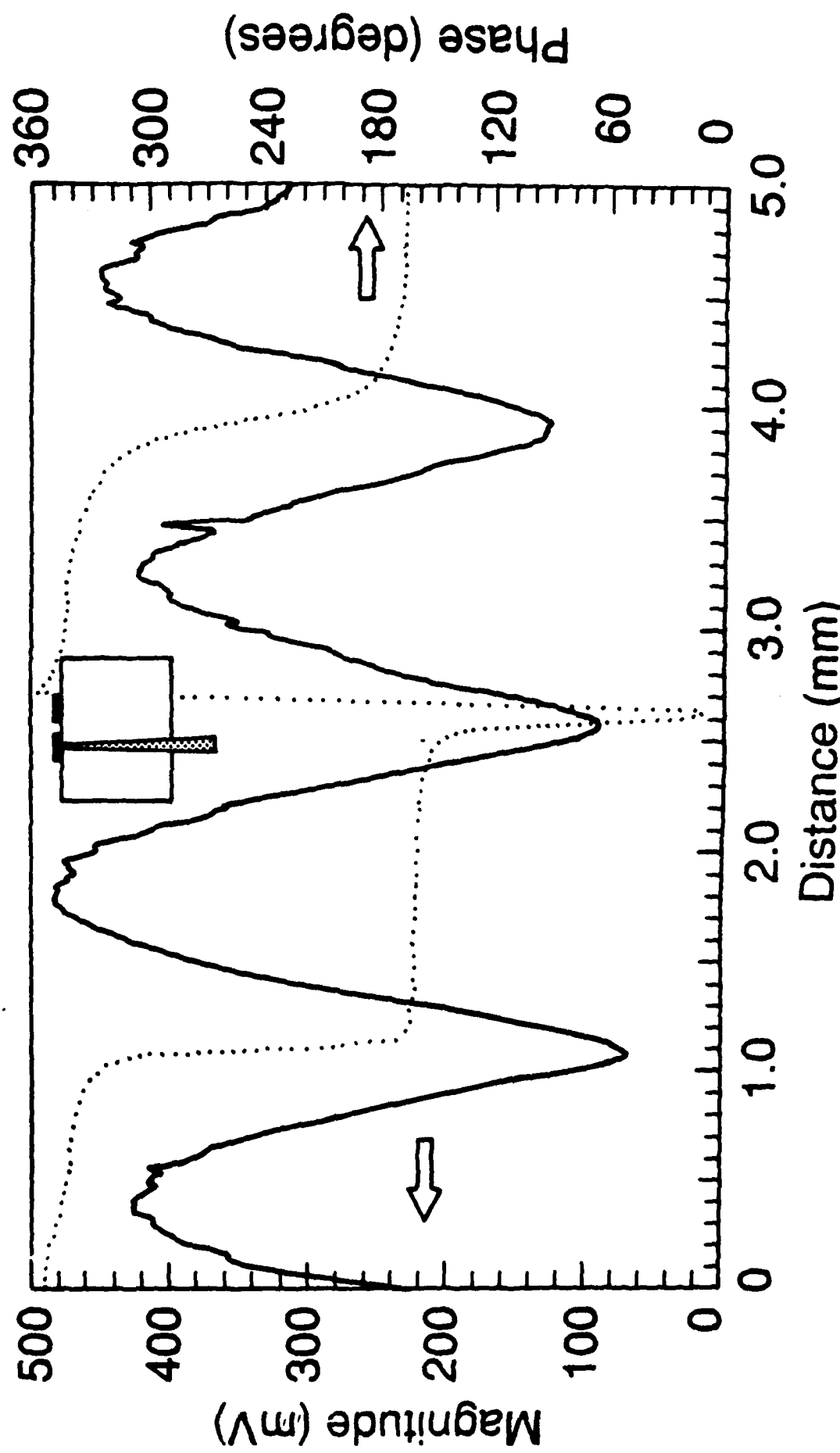


Figure 61: Magnitude and phase of the CPS 40 GHz standing wave. The standing wave minima are separated by 1.5 mm which is half of the CPS guide-wavelength at 40 GHz. The phase changes by 180° at the positions of the minima.

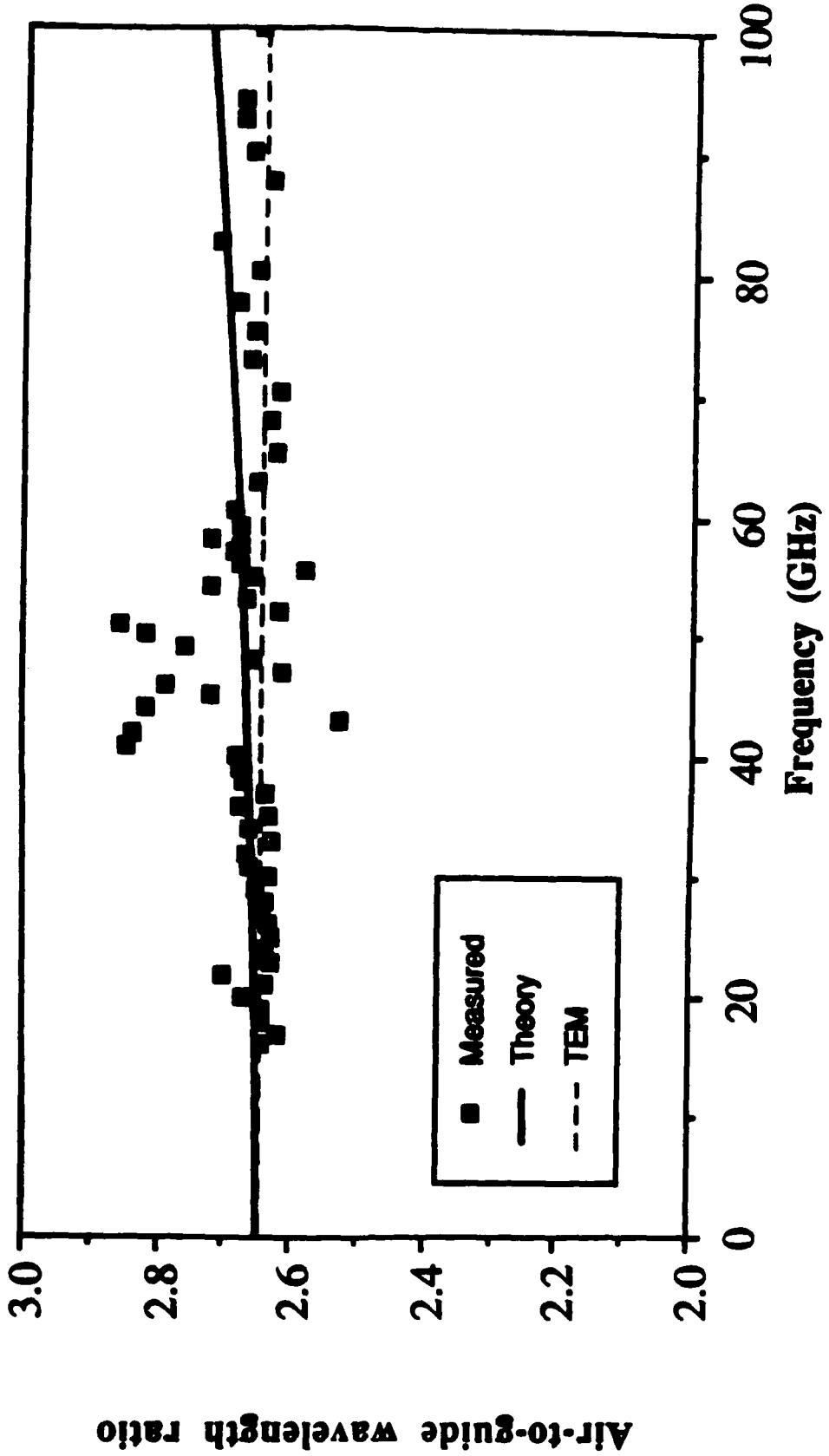


Figure 62: 15 to 100 GHz dispersion characteristics of the CPW odd mode. The 60 to 100 GHz signal was provided by the active probe frequency multiplier. The coupling between the quasi-slab mode and the quasi-TEM mode in the CPW occurs between 45 and 60 GHz. In this frequency range due to small differences between these two modes either one could be excited depending on the signal launching characteristics resulting in a larger data scatter.

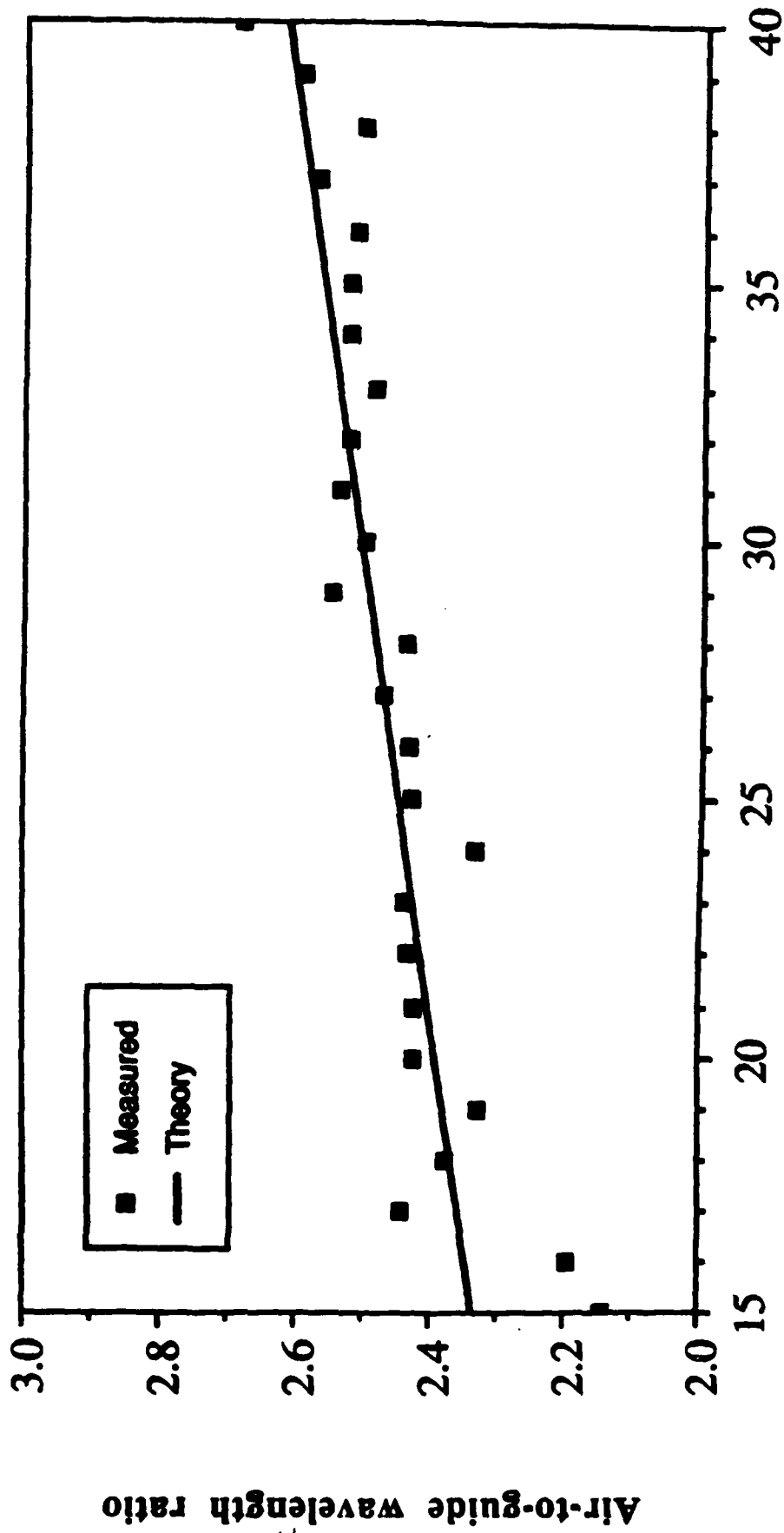


Figure 63: 15 to 40 GHz dispersion characteristics of the CPW even mode. The theoretical curve is obtained by approximating the even mode by a slot line with a slot width equal to the ground-to-ground spacing of the CPW. This is a good approximation in the case of small center conductor width.

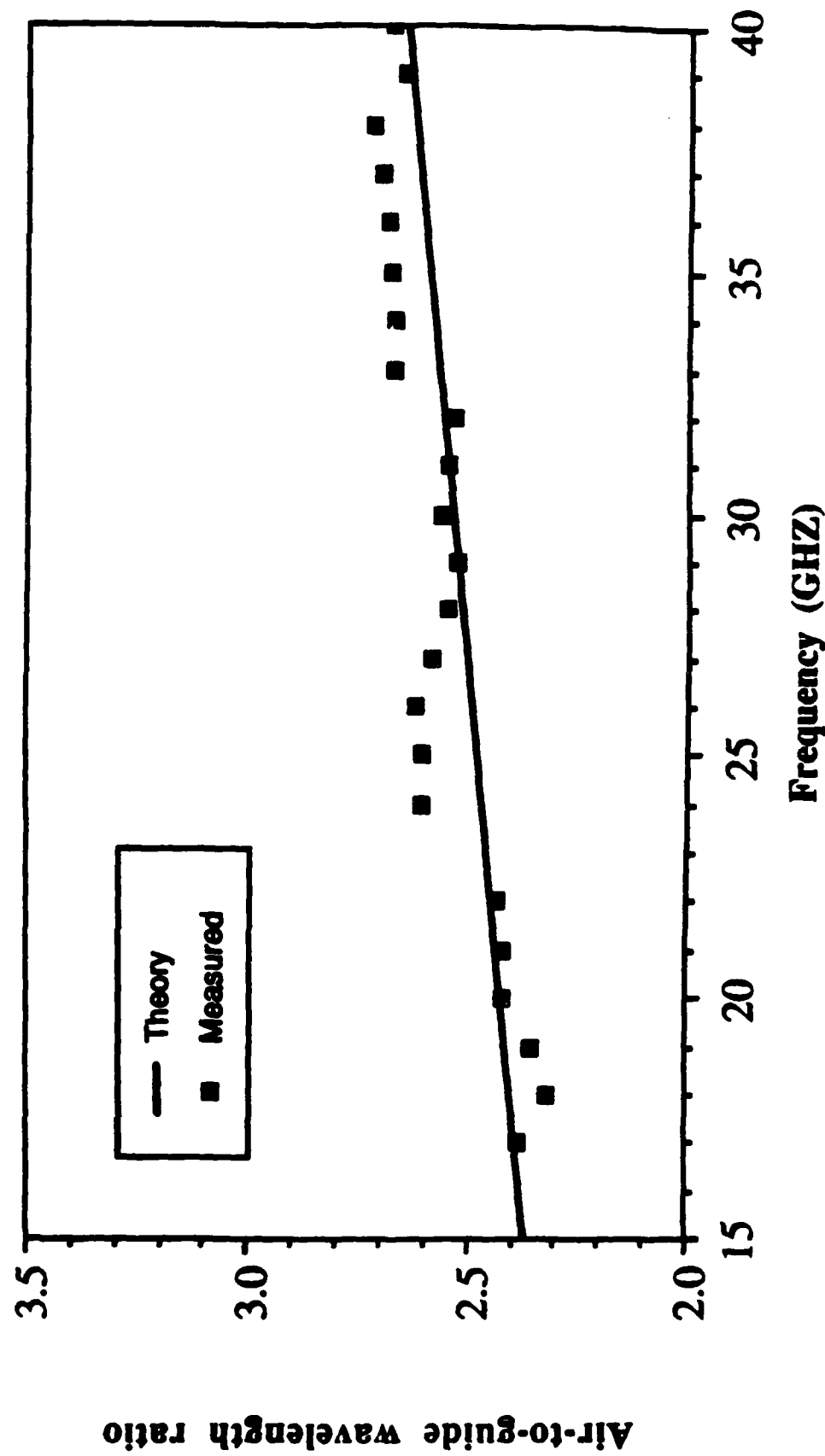


Figure 64: 16 to 40 GHz dispersion characteristics of the slot line.

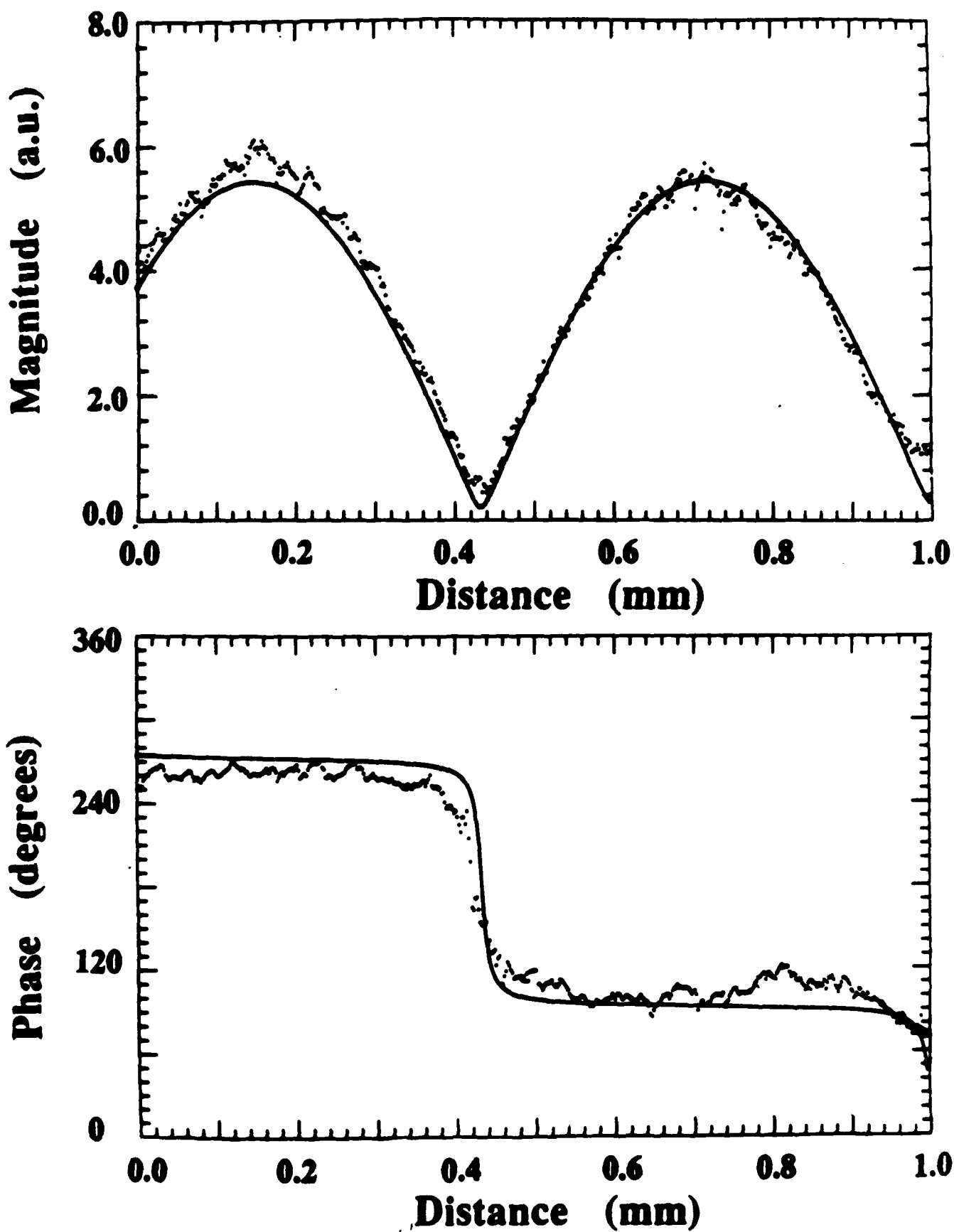
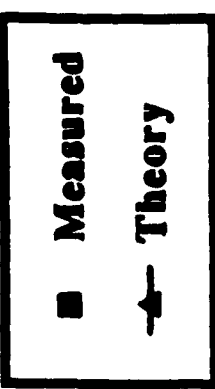


Figure 65: Magnitude and phase of the standing wave measured on a 50 ohm CPW terminated in short circuit at 100 GHz, using electrooptic sampling technique. The dotted line is the actual data from which the input reflection coefficient is calculated. The solid line is the standing wave calculated form the input reflection coefficient.



Test Structure

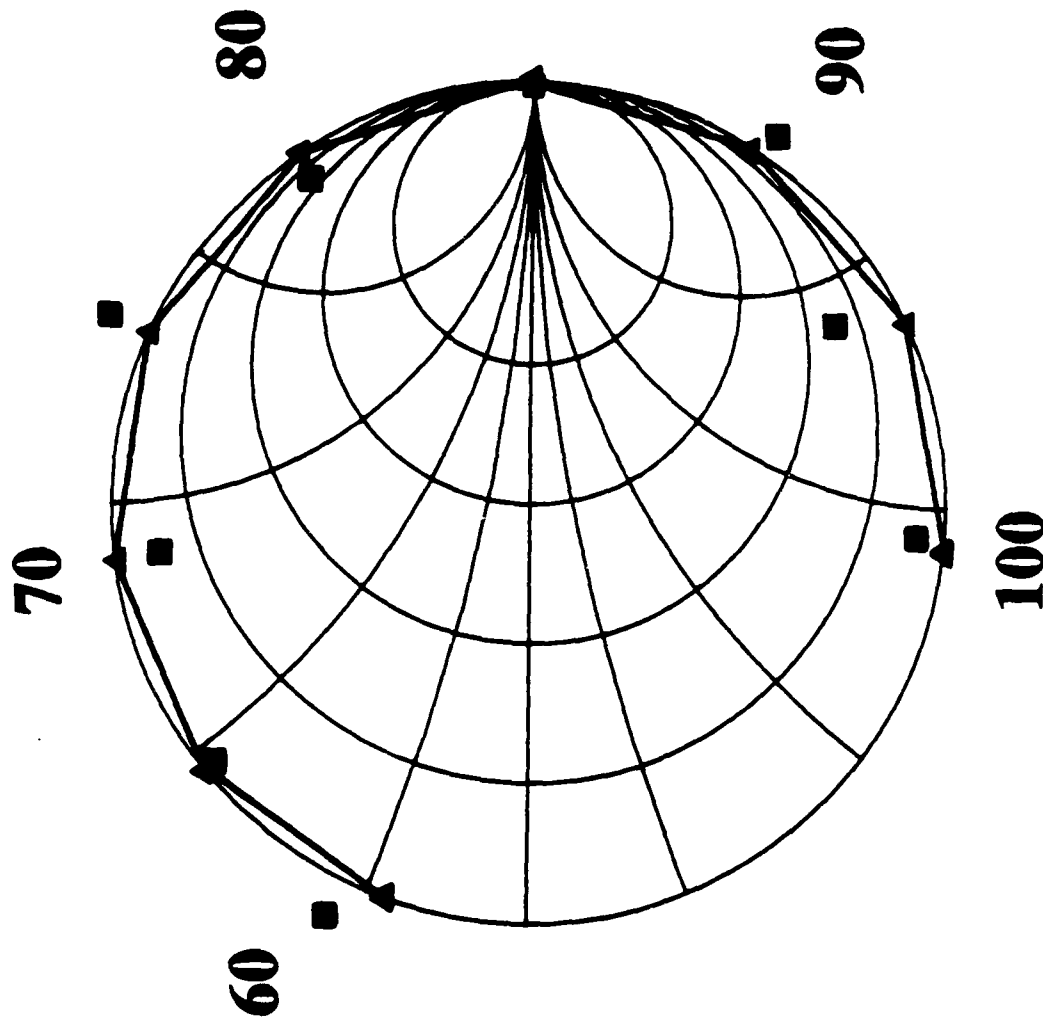
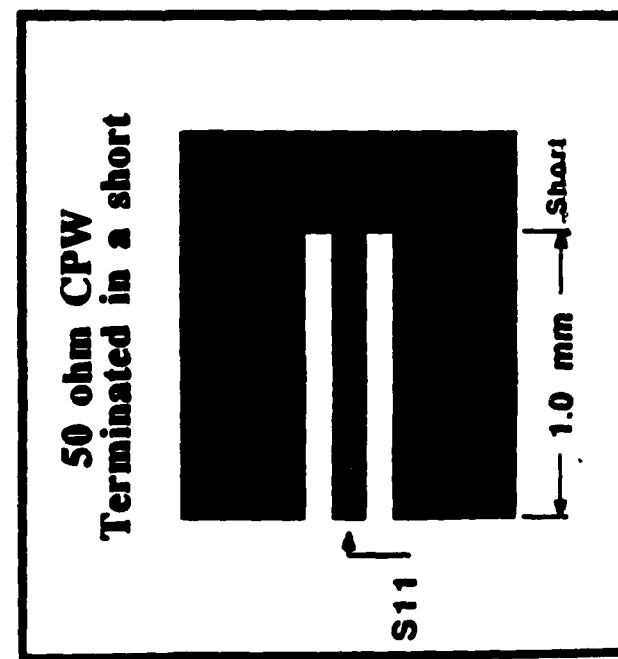


Figure 66: One-port S-parameter measurements obtained using the active probe and the electrooptic sampler over the frequency range of 60 to 100 GHz. The circuit consisted of a 1.0 millimeter long, 50 ohm CPW terminated in short circuit. The squares are the measured S-parameter; and the triangles are the simulation results. The shorted-end inductive effect was not included in the model.

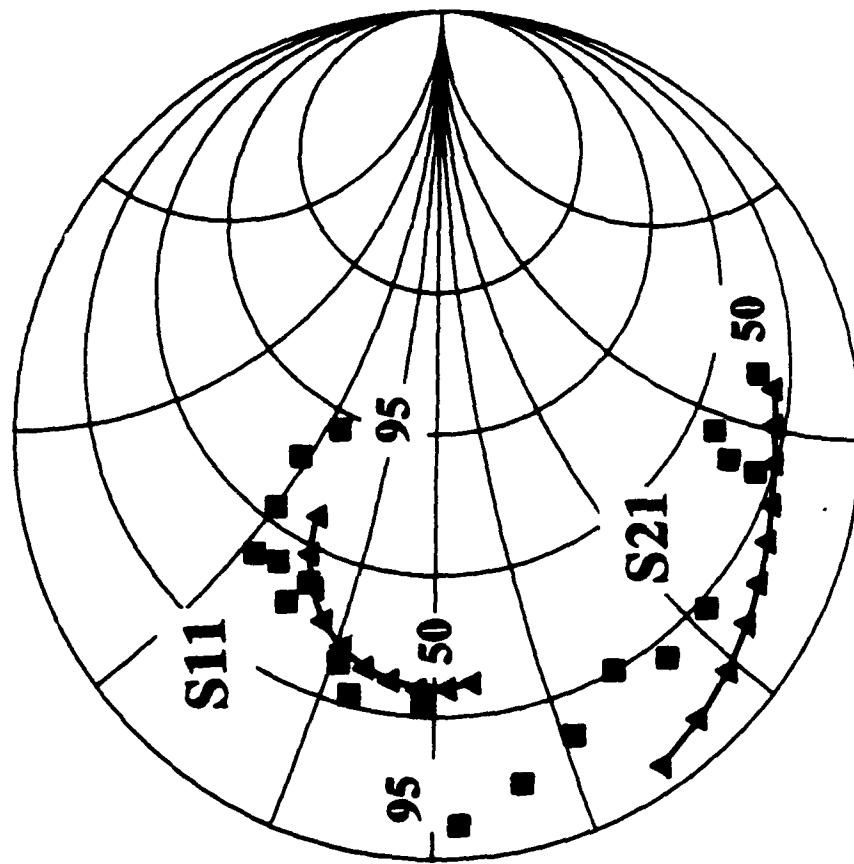
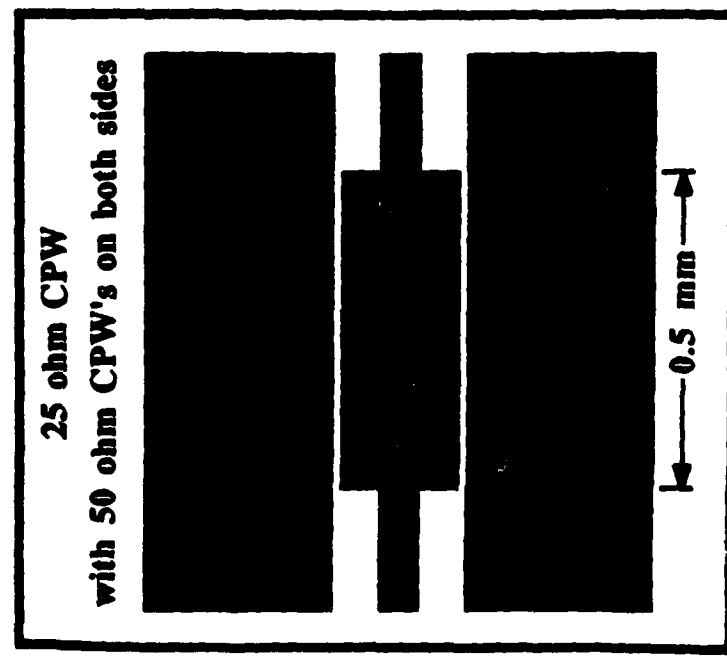
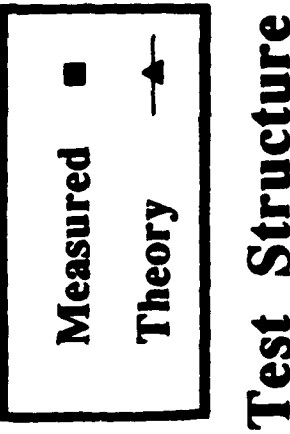
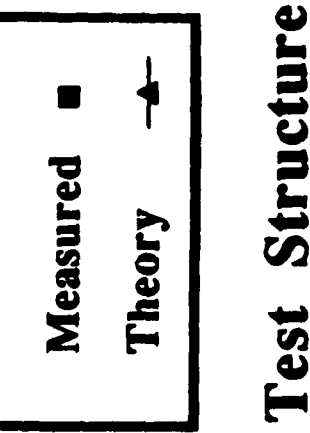


Figure 67: 50 to 95 GHz two-port S-parameter measurements using the active probe and the electrooptic sampler. The test structure consist of the a 25 ohm CPW which has a center conductor width of 42 microns and a gap-spacing of 2 microns on a 500 microns substrate. The theoretical curve does not include the effects of the discontinuities and the losses in the model. The frequency dispersion in this model is therefore less than the actual data.



Test Structure

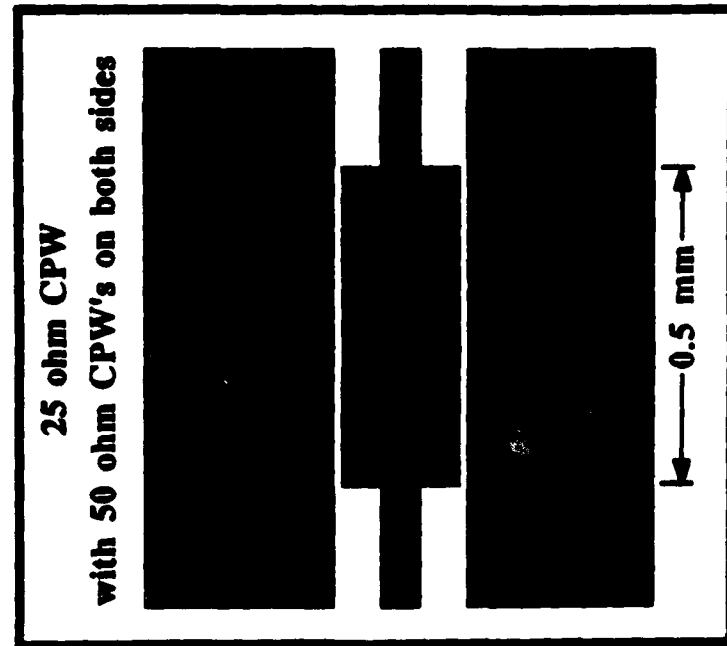


Figure 68: 50 to 95 GHz two-port S-parameter measurements using the active probe and the electrooptic sampler. The test structure consist of the a 25 ohm CPW which has a center conductor width of 42 microns and a gap-spacing of 2 microns on a 500 microns substrate. In this figure the theoretical curve includes the effects of the discontinuities and the losses in the model. The frequency dispersion in this model is therefore closer to the actual data compared with figure 67.

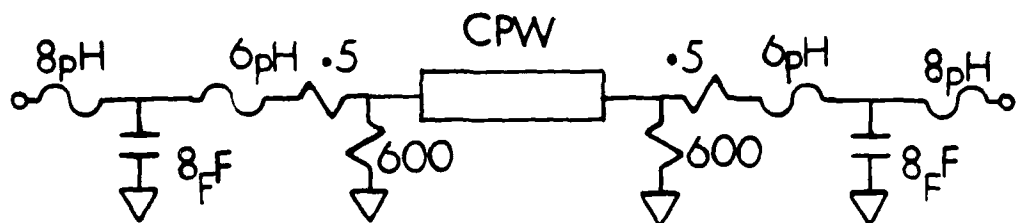


Figure 69: The CPW with the discontinuity models and losses modelled by lumped resistors.

the test-structure was less than 50 microns and there are no discontinuities in the ground planes, the center conductor discontinuities are not negligible at millimeter-wave frequencies. Figure 68 shows the same data compared to an approximate model which includes lumped circuit models for the discontinuities and the losses. The circuit model is shown in Figure 69. The correlation between the model and the data is improved by incorporating these parasitic effects.

5. Conclusion

A variety of new probing techniques for high-speed integrated circuits have been investigated by researchers, with the objective of providing an instrument with bandwidth greater than that of the tested device, a spatial resolution sufficient to permit access to finely spaced conductors within these circuits, measuring their potential independent of the potential of nearby conductors, and with negligible degradation of measurement accuracy from circuit perturbation. The techniques discussed in the introduction use either electron or optical beams to measure electrical signals on an IC, and all have some degree of trade-off between achieving best time resolution, spatial resolution, and perturbation of the circuit operation. Direct electrooptic sampling uses the substrate of the GaAs IC itself as the electrooptic modulator, eliminating external electrooptic elements and their invasive aspects, and permitting access to arbitrary points within the circuit without physical contact to a resolution limited by the diameter of the focused infrared probe beam. With the substrate serving as the electrooptic element, the optical properties of the circuit must be considered (polishing of the substrate backside and metallization reflectivity), and probe beam absorption through deep levels in the GaAs substrate can affect circuit operation. Reducing the probe beam intensity, using a longer wavelength beam, and avoiding active devices reduces this perturbation. The sections on system bandwidth and sensitivity describe limits on the instrument's time resolution and accuracy. Since the intensity modulations due to the electrooptic effect are small, full understanding of the noise sources in the system and methods for their suppression is crucial if the system is to provide useful circuit measurements. The dominant accuracy limitation in backside probing is the non-zero backside potential, which depends most strongly on ground-to-ground spacing of frontside conductors. The system described in this paper has a potential time resolution of less than 2 ps, a corresponding bandwidth greater than 100 GHz, a working sensitivity of $70 \mu\text{V}/\sqrt{\text{Hz}}$, and a spatial resolution of less than 3 microns.

The direct electrooptic sampling system has several aspects critical for IC testing in addition to internal node testing. Synchronization of the laser probe pulses to the signal generator driving the IC permits operation of the circuit in its normal fashion, driven by microwave or digital signals from electronic sources. Integration of the electrooptic sampling system with a microwave wafer probe station permits wafer-level optical probing of high-speed IC's. Measurement results on a variety of GaAs analog microwave and high-speed digital integrated circuits have been presented, such as gate propagation delay and logic timing measurements of an 8-bit multiplexer/demultiplexer clocked at 2.6 GHz, a 20 gate inverter chain using $1\mu\text{m}$ MESFET technology, 18 GHz static frequency dividers using $0.2\mu\text{m}$ MESFET technology on digital IC's, internal signal measurements on 2-18 GHz microstrip and coplanar waveguide traveling-wave amplifiers, and voltage standing wave and reflection coefficient measurements on transmission lines at frequencies to 40 GHz. The development of the active probe frequency-multiplier has extended the measurement capabilities of the electrooptic

sampler to the millimeter-wave frequencies. On-wafer millimeter-wave S-parameter measurement results up to 100 GHz of one-port and two-port networks, millimeter-wave time-waveform measurements and potential mapping of uniplanar guides on GaAs, using the active probe and the electrooptic sampler have been presented. Monolithic integration of the active probe circuits and reductions of the pulsewidth and timing jitter of the laser pulses will extend the measurement capability of the electrooptic sampler to 300 GHz.

6. Acknowledgments

The authors thank J.F. Jensen of Hughes Research Laboratories (Malibu), M. Riaziat of Varian Research Center, K.R. Gleason of Cascade Microtech and TriQuint Semiconductor, Inc., S. Swierkowski of Lawrence Livermore National Labs, E. Ehlers and G. Andersen of Hewlett-Packard Co. for their assistance with the GaAs devices and circuits. Thanks to T. Baer and J.D. Kafka of Spectra-Physics, inc., for their assistance with the optical pulse compressor. We acknowledge the generous equipment donations of Cascade Microtech, Inc., Tektronix, Inc, and the Hewlett-Packard Co.

References

1. H.Q. Tserng and B. Kim: "110 GHz GaAs FET Oscillator," *Elec. Lett.*, vol. 21, pp. 178-179, 1985
2. T. Henderson, M.I. Aksun, C.K. Peng, Hadis Morkoc, P.C. Chao, P.M. Smith, K.-H. G. Duh, and L.F. Lester: "Microwave performance of a Quarter-Micrometer Gate Low-Noise Pseudomorphic InGaAs/AlGaAs Modulation-Doped Field Effect Transistor," *IEEE Elect.Dev. Lett.*, vol. EDL-7, pp. 649-651, 1986
3. T.C.L.G. Sollner, E.R. Brown, W.D. Goodhue, and H.Q. Le: "Observation of millimeter-wave oscillations from resonant tunneling diodes and some theoretical considerations of ultimate frequency limits", *Appl. Phys. Lett.*, vol. 50, pp. 332-334, 1987
4. J.F. Jensen, L.G. Salmon, D.S. Deakin, and M.J. Delaney: "Ultra-high speed GaAs static frequency dividers," Technical Digest of the 1986 International Electron Device Meeting, p. 476-479
5. E.W. Strid, K.R. Gleason, and T.M. Reeder: "On-wafer measurement of gigahertz integrated circuits," *VLSI Electronics: Microstructure Science, Vol 11*, New York: Academic Press, 1985, pp. 265-287
6. Cascade Microtech, Inc., P.O. Box 2015, Beaverton, OR 97075
7. Hypres, Inc., 175 Clearbrook Rd., Elmsford, NY 10523
8. "Electron-beam testing of VLSI chips gets practical," *Electronics*, March 24, 1986, pp. 51-54.
9. R. Iscoff: "E-beam probing systems: filling the submicron gap," *Semiconductor International*, Sept. 1985, pp. 62-68
10. P. May, J.-M. Halbout, and G. Chiu: "Laser pulsed E-beam system for high speed IC testing," to be published in *Picosecond Electronics and Optoelectronics*, New York: Springer-Verlag, 1987
11. R.B. Marcus, A.M. Weiner, J.H. Abeles, and P.S.D. Lin: "High-speed electrical sampling by fs photoemission," *Appl. Phys. Lett.*, vol. 49, pp. 357-359, 1986
12. J. Bokor, A.M. Johnson, R.H. Storz, and W.M. Simpson: "High-speed circuit measurements using photoemission sampling," *Appl. Phys. Lett.*, vol. 49, pp. 226-228, 1986

13. A.M. Weiner, R.B. Marcus, P.S.D. Lin, and J.H. Abeles: "Photoemissive testing of high-speed electrical waveforms," to be published in *Picosecond Electronics and Optoelectronics*, New York: Springer-Verlag, 1987
14. H.K. Heinrich, D.M. Bloom, and B.R. Hemenway: "Noninvasive sheet charge density probe for integrated silicon devices," *Appl. Phys. Lett.*, vol. 48, pp. 1066-1068, 1986
15. H.K. Heinrich, B.R. Hemenway, K.A. McGroddy, and D.M. Bloom: "Measurement of real-time digital signals in a silicon bipolar junction transistor using a noninvasive optical probe," *Elec. Lett.*, vol. 22, pp. 650-652, 1986
16. J.A. Valdmanis, G.A. Mourou, and C.W. Gabel: "Picosecond electro-optic sampling system," *Appl. Phys. Lett.*, vol. 41, pp. 211-212, 1982
17. B.H. Kolner, D.M. Bloom, and P.S. Cross: "Electro-optic sampling with picosecond resolution," *Elec. Lett.*, vol. 19, 574-575, 1983
18. J.A. Valdmanis, G.A. Mourou, and C.W. Gabel: "Subpicosecond electrical sampling," *IEEE J. Quantum Elect.*, vol. QE-19, 664-667, 1983
19. J.A. Valdmanis and G. Mourou: "Subpicosecond electrooptic sampling: principles and applications," *IEEE J. Quantum Elect.*, vol. QE-22, pp. 69-78, 1986
20. D.R. Dykaar, R. Sobolewski, J.F. Whitaker, T.Y. Hsiang, G.A. Mourou, M.A. Hollis, B.J. Clifton, K.B. Nichols, C.O. Bozler, and R.A. Murphy: "Picosecond characterization of ultrafast phenomena: new devices and new techniques," *Ultrafast Phenomena V*, ed. by G.R. Fleming and A.E. Siegman, Springer Ser. Chem. Phys., Vol. 46, New York: Springer-Verlag, 1986 pp. 103-106
21. J.A. Valdmanis and S.S. Pei: "A non-contact picosecond prober for integrated circuit testing." To be published in *Picosecond Electronics and Optoelectronics*, New York: Springer-Verlag, 1987
22. J.A. Valdmanis and S.S. Pei: "Picosecond non-contact electrooptic probing for integrated circuits," *Technical Digest of the 1987 Conference on Lasers and Electrooptics*, pp. 352-353
23. J.A. Valdmanis: Presentation FN3 at the 1987 Conference on Laser and Electrooptics, and private communication
- 24 I.P. Kaminow, *An Introduction to Electro-Optic Devices.*, New York: Academic Press, 1974
25. I.P. Kaminow and E.H. Turner: "Electrooptic light modulators," *Proc. IEEE*, 54, 1374-1390 (1966)

26. B.H. Kolner and D.M. Bloom: "Direct electrooptic sampling of transmission-line signals propagating on a GaAs substrate," *Elect. Lett.*, vol. 20, 818-819, 1984
27. B.H. Kolner and D.M. Bloom: "Electrooptic sampling in GaAs integrated circuits," *IEEE J. Quant. Elect.*, vol. QE-22, 79-93, 1986
28. A. Yariv and P. Yeh: *Optical Waves in Crystals*, New York: New York: John Wiley & Sons, Inc, 1984, pp. 286-287
29. *Ibid*, p. 230
30. J.L. Freeman, S.K. Diamond, H. Fong, and D.M. Bloom: "Electrooptic sampling of planar digital integrated circuits," *Appl. Phys. Lett.*, vol. 47, 1083-1084, 1985
31. W.H. Knox, R.L. Fork, M.C. Downer, R.H. Stolen, and C.V. Shank: "Optical pulse compression to 8 fs at a 5-kHz repetition rate," *Appl. Phys. Lett.*, vol. 46, 1120-1121, 1985
32. C.H. Brito-Cruz, R.L. Fork, and C.V. Shank: "Compression of optical pulses to 6 fs using cubic phase distortion compensation," *Technical Digest of the 1987 Conference on Lasers and Electrooptics*, pp. 12-13
33. A.S. Gouveia-Neto, A.S.L. Gomes, and J.R. Taylor: "Generation of 33-fsec pulses at 1.32 μm through a high-order soliton effect in a single-mode optical fiber," *Optics Letters*, vol. 12, 395-397, 1987
34. B. Zysset, W. Hodel, P. Beaud, and H.P. Weber: "200-femtosecond pulses at 1.06 μm generated with a double-stage pulse compressor," *Optics Letters*, vol. 11, 156-158, 1986
35. R.N. Bracewell, *The Fourier Transforms and its Applications*, New York: McGraw-Hill, 1978
36. D. Cotter, "Technique for highly stable active mode-locking," *Ultrafast Phenomena IV*, D.A. ed. by Auston and K.B. Eisenthal, New York: Springer-Verlag, 1984, p. 78-80
37. M.J.W. Rodwell, K.J. Weingarten, D.M. Bloom, T. Baer, and B.H. Kolner: "Reduction of timing fluctuations in a mode-locked Nd:YAG laser by electronic feedback," *Optics Letters*, vol. 11, 638-640, 1986
38. E.B. Treacy: "Optical pulse compression with diffraction gratings," *IEEE J. Quant. Elect.*, vol. QE-5, 454-458, 1969

39. D. Grischkowsky and A.C. Balant: "Optical pulse compression based on enhanced frequency chirping," *Appl. Phys. Lett.*, vol. 41, 1-3, 1982
40. J.D. Kafka, B.H. Kolner, T. Baer, and D.M. Bloom: "Compression of pulses from a continuous-wave mode-locked Nd:YAG laser," *Opt. Lett.*, vol. 9, 505-506, 1984
41. A.J. Taylor, J.M. Wiesenfeld, G.Eisenstein, R.S. Tucker, J.R. Talman, and U. Koren: "Electrooptic sampling of fast electrical signals using an InGaAsP injection laser," *Elec. Lett.*, vol. 22, 61-62, 1986
42. A.J. Taylor, J.M. Wiesenfeld, R.S. Tucker, G.Eisenstein, J.R. Talman, and U. Koren: "Measurement of a very high-speed InGaAs photodiode using electrooptic sampling," *Elec. Lett.*, vol. 22, 325-327, 1986
43. J.M. Wiesenfeld, R.S. Tucker, A. Antreasyan, C.A. Burrus, and A.J. Taylor: "Electrooptic sampling measurements of high-speed InP integrated circuits," *Appl. Phys. Lett.*, vol. 50, 1310-1312, 1987
44. J.P. Heritage, R.N. Thurston, W.J. Tomlinson, and A.M. Weiner: "Spectral windowing of frequency-modulated optical pulses in a grating compressor," *Appl. Phys. Lett.*, vol. 47, 87-89, 1985
45. N.J. Halas and D. Grischkowsky: "Simultaneous optical pulse compression and wing reduction," *Appl. Phys. Lett.*, vol. 48, 823-825, 1986
46. M.J.W. Rodwell, K.J. Weingarten, J.L. Freeman, and D.M.Bloom: "Gate propagation delay and logic timing of GaAs integrated circuits measured by electro-optic sampling," *Elec. Lett.*, 22, 499-501, 1986
47. J.D. Kafka and T. Baer: "Intensity fluctuations in optical pulse compression," *Technical Digest of the 1987 Conference on Lasers and Electrooptics*, pp. 276-277
48. K.J. Weingarten, M.J.W. Rodwell, and D.M. Bloom: "Picosecond sampling of GaAs integrated circuits," To be published in *Picosecond Electronics and Optoelectronics*, New York: Springer-Verlag, 1987
49. M.N. Islam, L.F. Mollenauer, and R.H. Stolen: *Ultrafast Phenomena V*, ed. by G.R. Fleming and A.E. Siegman, Springer Ser. Chem. Phys., Vol. 46, New York:Springer-Verlag, 1986, pp. 46-50
50. J.D. Kafka and T. Baer: "Fiber Raman soliton laser pumped by a Nd:YAG laser," *Optics Letters*, vol. 12, 181-183, 1987

51. R.M. Shelby, M.D. Levenson, and P.W. Bayer: "Guided acoustic-wave Brillouin scattering," *Phys. Rev. B*, vol. 31, 5244-5252, 1985
52. J.L. Freeman, S.R. Jefferies, and B.A. Auld, "Full-field modeling of the longitudinal electro-optic probe," *Opt. Lett.*, vol. 12, 795-797, 1987
53. J.L. Freeman, D.M. Bloom, S.R. Jefferies, and B.A. Auld, "Accuracy of electrooptic Measurements of Coplanar Waveguide Transmission Lines," *Appl. Phys. Lett.*, vol. 53, 7-9, 1988.
54. G.M. Martin, "Optical assessment of the main electron trap in bulk-semi-insulating GaAs," *Appl. Phys. Lett.*, vol. 39, 747-748, 1981
55. P. Dobrilla and J.S. Blakemore, "Experimental requirements for quantitative mapping of midgap flaw concentration in semi-insulating GaAs wafers by measurement of near-infrared transmittance," *J. Appl. Phys.*, vol. 58, 208-218, 1985
56. S. Swierkowski, K. Mayeda, and C. McGonagh: "A sub-200 picosecond GaAs sample-and-hold circuit for a multi-gigasample/second integrated circuit," *Technical Digest of the 1985 International Electron Devices Meeting*, pp. 272-275
57. X.-C. Zhang and R. K. Jain: "Measurement of on-chip waveforms and pulse propagation in digital GaAs integrated circuits by picosecond electro-optic sampling," *Elec. Lett.*, vol. 22, 264-265, 1986
58. J.F. Jensen, K.J. Weingarten, and D.M. Bloom: To be published in *Picosecond Electronics and Optoelectronics*, New York: Springer-Verlag, 1987
59. G.D. McCormack, A.G. Rode, and E.W. Strid: "A GaAs MSI 8-bit Multiplexer and Demultiplexer," *Proceedings of the 1982 GaAs IC Symposium*, pp. 25-28
60. X.-C. Zhang, R.K. Jain, and R.M. Hickling: "Electrooptic sampling analysis of timing patterns at critical internal nodes in GigaBit GaAs multiplexers/demultiplexers," To be published in *Picosecond Electronics and Optoelectronics*, New York: Springer-Verlag, 1987
61. R.E. Collins, *Foundations of Microwave Engineering*, New York: McGraw-Hill, 1966
62. K.J. Weingarten, M.J.W. Rodwell, J.L. Freeman, S.K. Diamond, and D.M. Bloom: "Electrooptic sampling of gallium arsenide integrated circuits," *Ultrafast Phenomena V*, ed. by G.R. Fleming and A.E. Siegman, Springer Ser. Chem. Phys., Vol. 46, New York: Springer-Verlag, 1986, pp. 98

63. M.J.W. Rodwell, M. Riaziat, K.J. Weingarten, B.A. Auld, and D.M. Bloom: "Internal microwave propagation and distortion characteristics of travelling-wave amplifiers studied by electro-optic sampling," *IEEE Trans. Microwave Theory Tech.*, vol. MTT-34, 1356-1362, 1986
64. G. Zdasiuk, M. Riaziat, R. LaRue, C. Yuen, and S. Bandy: "Enhanced performance ultra-broadband distributed amplifiers," To be published in *Picosecond Electronics and Optoelectronics*, New York: Springer-Verlag, 1987
65. J. Archer, "Millimeter Wavelength Frequency Multipliers", IEEE MTT, Vol. 29, No. 6, June 1981.
66. R. Majidi-Ahy and D. M. Bloom, "A Millimeter-Wave Active Probe Frequency-Multiplier for On-Wafer Characterization of GaAs Devices and IC's", *submitted to IEE Electronics Letters*, August 1988.
67. E. Ehlers et al., "Extending Millimeter-Wave Diode Operation to 110 GHz", Hewlett-Packard Journal, Vol. 37, No. 11, November 1986.
68. M. Kohn et al., "Harmonic Mixing with an Anti-parallel Diode Pair", IEEE MTT, Vol. 23, No. 8, August 1975.
69. Matthei, Young and Jones, "Microwave Filters, Impedance Matching Networks and Coupling Structures", McGraw Hill, 1964.
70. C. P. Wen, "Coplanar Waveguide: A Surface Strip Transmission Line Suitable for Non-reciprocal Gyromagnetic Device Applications", MTT-17, No. 12, Dec. 1969, pp. 1087-1090.
71. S. B. Cohn, "Slot Line on a Dielectric Substrate", MTT-17, No. 10, Oct. 1969, pp. 768-778.
72. E. A. Mariani et al., "Slot Line Characteristics", MTT-17, No. 12, December 1969, pp. 1091-1096.
73. M. Riaziat et al., "Coplanar Waveguides used in 2-18 GHz Distributed Amplifier", MTT-Symposium Digest 1987, pp. 337-339.
74. R. Majidi-Ahy et al., "Electrooptic Sampling Measurement of Coplanar Waveguide (Coupled Slot Line) Modes", Elect. Lett., Vol. 23, No. 24, Nov. 1987, pp. 1262-1263.
75. R. Majidi-Ahy et al., "Electrooptic Sampling Measurement of Dispersion Characteristics of Slot line and Coplanar Waveguide Even and Odd Modes", MTT-Symposium Digest 1988, pp. 301-304.

76. B. K. Knorr et al., "Analysis of Coupled Slots and Coplanar Strips on Dielectric Substrate",
MTT-23, No. 7, July 1975, pp. 541-548.

Papers Presented at Meetings, Conferences, and Seminars

M. J. W. Rodwell, M. Riaziat *, K. J. Weingarten, and D. M. Bloom "Internal Microwave Propagation and Distortion Characteristics of Travelling-Wave Amplifiers Studied by Electrooptic Sampling" Presented - 1986 IEEE MTT Symposium. * Varian Associates, Palo Alto, CA 94303

K. J. Weingarten, M. J. W. Rodwell, J. L. Freeman, S. K. Diamond, and D. M. Bloom "Electrooptic Sampling of Gallium Arsenide Integrated Circuits" Presented - 1986 Topical Meeting on Ultrafast Phonomena

K. J. Weingarten, R. Majidi-Ahy, M. J. W. Rodwell, B. A. Auld, and D. M. Bloom "Microwave Measurements of GaAs Integrated Circuits Using Electrooptic Sampling" Presented - IEEE MTT Symposium 1987

R. Majidi-Ahy, K. J. Weingarten, M. Riaziat, D. M. Bloom, and B\ A. Auld "Electrooptic Sampling Measurement of Dispersion Characteristics of Slot line and Coplanar Waveguide (Coupled Slot Line) Even and Odd modes", IEEE MTT-S International Microwave Symposium Digest (May 25, 1988)

K. J. Weingarten, M. J. W. Rodwell, and D. M. Bloom "Picosecond sampling of GaAs integrated circuits" in Picosecond Electronics and Optoelectronics New York: Springer-Verlag. 1987

J. F. Jensen, K. J. Weingarten, and D. M. Bloom in Picosecond Electronics and Optoelectronics. New York: Springer-Verlag, 1987

K. J. Weingarten, M. J. W. Rodwell, J. L. Freeman, S. K. Diamond, and D. M. Bloom "Electrooptic sampling of gallium arsenide integrated circuits" in Ultrafast PhenomenaV, G. R. Fleming and A. E. Siegman, Eds. New York: Springer-Verlag, 1986, p. 98, Springer Ser. Chem. Phys., vol. 46

List of Written Publications in Technical Journals

K. J. Weingarten, M. J. W. Rodwell, H. K. Heinrich, B. H. Kolner, and D. M. Bloom, "Direct Electrooptic Sampling of GaAs Integrated Circuits," Elect. Lett. 21, 765-766 (August 1985).

M. J. W. Rodwell, K. J. Weingarten, J. L. Freeman, and D. M. Bloom, "Gate Propagation Delay and Logic Timing of GaAs Integrated Circuits Measured by Electrooptic Sampling," Elect. Lett. 22, 499-501 (April 24, 1986).

M. J. W. Rodwell, K. J. Weingarten, D. M. Bloom, T. M. Baer, and B. H. Kolner, "Reduction of Timing Fluctuations in a Mode-Locked Nd:YAG Laser by Electronic Feedback," Opt. Lett. Vol. 11, 638-640 (October 1986).

M. J. Rodwell, M. Riaziat, K. J. Weingarten, B. A. Auld, and D. M. Bloom, "Internal Microwave Propagation and Distortion Characteristics of Traveling-Wave Amplifiers Studied by Electrooptic Sampling," IEEE Trans. MTT, Vol. MTT-34, (12), 1356-1361 (December 1986).

K. J. Weingarten, M. J. W. Rodwell, and D. M. Bloom "Picosecond Sampling of GaAs Integrated Circuits" IEEE Journal of Quantum Electronics Vol. 24/No.2 February 1988

J. L. Freeman, D. M. Bloom, S. R. Jefferies, and B. A. Auld "Accuracy of Electrooptic Measurements of Coplanar Waveguide Transmission Lines" Applied Physics Newsletter 53 (1), 4 July 1988

B. H. Kolner and D. M. Bloom, "Direct electrooptic sampling of transmission-line signals propagating on a GaAs substrate" Electronics Letters vol.20, pp. 818-819, 1984

B. H. Kolner and D. M. Bloom, "Electrooptic sampling in GaAs intrgrated circuits" IEEE Journal of Quantum Electronics vol QE-22 pp. 79-93, 1986

J. L. Freeman, S. K. Diamond, H. Fong, and D. M. Bloom, "Electrooptic sampling of planar digital integrated circuits" Applied Physics Letters vol 47 pp. 1083-1084, 1985

M. J. W. Rodwell, M. Riaziat, K. J. Weingarten, B. A. Auld, and D. M. Bloom, "Internal microwave propagation and distortion characteristics of travelling-wave amplifiers studied by electro-optic sampling," IEEE Trans. Microwave Theory Tech., vol MTT-34, pp. 1356-1362, 1986

SUBMITTED

M. J. W. Rodwell, D. M. Bloom, and K. J. Weingarten * "Subpicosecond Laser Timing Stabilization" Submitted to IEEE Journal of Quantum Electronics

R. Majidi-Ahy and D. M. Bloom "A Millimeter-Wave Active Probe Frequency-Multiplier for On-Wafer Characterization of GaAs Devices and IC's" Submitted to IEEE Electronics Letters

Advanced Degrees Awarded

Brian Kolner, Ph.D. August 1985
Picosecond Electrooptic Sampling in Gallium Arsenide.

Kurt Weingarten, Ph.D. January 1988
Gallium Arsenide Integrated Circuit Testing Using Electrooptic Sampling.

Mark Rodwell, Ph.D. January 1988
**Picosecond Electrical Wavefront Generation and Picosecond Optoelectronic
Instrumentation.**

James Freeman, Ph.D. August 1988
Accuracy and Invasivness of Direct Electrooptic Sampling of GaAs Integrated Circuits

Professional Personnel Associated with the Research

David M. Bloom, Principal Investigator

Advanced Degrees Awarded

Brian Kolner, Ph.D. August 1985
Picosecond Electrooptic Sampling in Gallium Arsenide.

Kurt Weingarten, Ph.D. January 1988
Gallium Arsenide Integrated Circuit Testing Using Electrooptic Sampling.

Mark Rodwell, Ph.D. January 1988
**Picosecond Electrical Wavefront Generation and Picosecond Optoelectronic
Instrumentation.**

James Freeman, Ph.D. August 1988
Accuracy and Invasivness of Direct Electrooptic Sampling of GaAs Integrated Circuits